RESOLUTION ANALYSIS OF PASSIVE SYNTHETIC APERTURE IMAGING OF FAST MOVING OBJECTS

L. BORCEA*, J. GARNIER†, G. PAPANICOLAOU‡, K. SOLNA§, AND C. TSOGKA¶

Abstract. In this paper we introduce and analyze a passive synthetic aperture radar system motivated by space surveillance radar networks for detecting, tracking, imaging, and identifying small debris (aka target) in low-earth orbit. We propose a system with a powerful transmitter on the ground and one or several flying receiver platforms. Each platform can separate the direct signals from the source, coming from below, and the reflected signals, coming from above. In the case of a single receiver platform, the image is formed by cross correlating the Doppler-compensated direct and reflected signals. We show that its resolution is described by the ideal Rayleigh resolution formulas. That is, range resolution is proportional to the transmitter pulse width, and the cross range resolutions are determined by the synthetic angular cones determined by the target and receiver trajectories. However, the one-receiver imaging modality is not capable of determining both the target location and velocity. In the case of multiple receiver platforms, the image is computed by cross correlating the Doppler-compensated reflected signals. In this case, the image focusing relies on differences of travel times between the moving target and the receivers, and we show that two well separated pairs of receiver platforms are sufficient for determining the target location and velocity. The resolution formulas for this imaging modality are new and different from the Rayleigh resolution limits. They are derived analytically from first principles, and are validated with detailed numerical simulations.

1. Introduction. In synthetic aperture radar (SAR), moving antennas are used to emulate extended apertures while the transmitter and receiver antennas are themselves small. In monostatic systems a flying platform (airborne or spaceborne) carries both the transmitter and receiver antennas [5, 7]. It is possible to have more elaborate, bistatic systems, in which the transmit and receiver antennas are separated by a distance that is as large as the expected target range. Since the early implementation of bistatic SAR systems [2], interest on bistatic SAR has increased and bistatic systems with many different receive-transmit configurations have been implemented. Most bistatic SAR systems image ground reflectivity from spaceborne and/or airborne transmitters and receivers. A spaceborne/airborne bistatic SAR system can, for example, use a satellite as a transmitter and an aircraft as a receiver as in [25]. In [1] the feasibility of space-ground bistatic SAR using navigation satellites as transmitters of opportunity and a fixed ground-based receiver is demonstrated.

In this paper we consider SAR systems for the tracking and imaging of small, fast and high-flying objects (aka targets) using airborne receiver platforms and one ground-based transmitter. We assume that the transmitter is emitting pulses repeatedly with a pulse repetition interval that is large compared to the total travel time from the transmitter to the target and then back to the receivers. This will be the situation in practice and the more explicit scaling assumptions are discussed in Appendix A.1. There are at least four reasons for considering such passive systems. First, the transmitter is on the ground, so it can be powerful enough to illuminate a large sector in the sky. Second, the receiver platform is moving, so it can generate large synthetic apertures. Third, passive correlation-based imaging does not require knowing the emitted signals, and it is not very sensitive to the source location in the case of multiple receiver platforms. Four, imaging with multiple receiver platforms flying above the turbulent atmosphere is robust with respect to atmospheric lensing [20] and aberrations [22, 24], as follows from [11, 13].

A potential application of the proposed passive SAR systems is the identification and tracking of small-sized (1-10 cm) energetic debris in low-earth orbit (below 2000 km), which can be a threat to the integrity of satellites [9, 15, 28]. Older space surveillance systems operating in the VHF-band ($30 - 300$ MHz) have recently been updated to improve resolution, and are now in the S-band ($2 - 4$ GHz). The turbulent atmosphere is not an issue at these frequencies. However, turbulence will be a limiting factor for future generations of space surveillance systems, operating in X-band ($8 - 12$ GHz) [16, 17, 19]. Passive SAR systems with multiple receiver platforms flying above the turbulent atmosphere would allow bypassing this

*Department of Mathematics, University of Michigan, Ann Arbor MI 48109. borcea@umich.edu

†Laboratoire de Probabilités et Modèles Aléatoires & Laboratoire Jacques-Louis Lions, Université Paris Diderot, 75205 Paris Cedex 13, France. garnier@math.univ-paris-diderot.fr

‡Department of Mathematics, Stanford University, Stanford CA 94305. papanicolaou@stanford.edu

§Department of Mathematics, University of California at Irvine, Irvine CA 92697. ksolna@math.uci.edu

¶Department of Mathematics and Applied Mathematics, University of Crete and IACM/FORTH, GR-71409 Heraklion, Greece. Work partially carried out while visiting the Mathematics Department at Stanford University. tsogka@uoc.gr

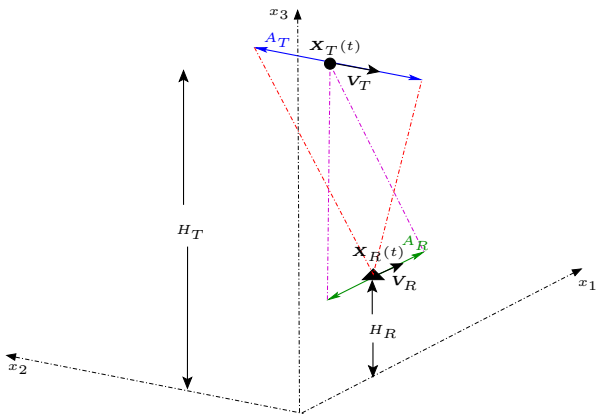

FIGURE 1.1. *Illustration of the imaging setup with a single receiver platform. The aperture A_R spanned by the receiver at altitude H_R is shown in green, and the aperture A_T spanned by the target at altitude H_T is shown in blue. The synthetic angular cones of opening angles of order A_R/H_R and A_T/H_T, which determine the cross-range resolutions of the images are shown with the dashed red lines.*

limitation.

We consider two imaging configurations with a single transmitter at location $\boldsymbol{X}_E$ on the ground. The first is for a single flying receiver platform, and the second is for one or two pairs of receiver platforms, flying in tandem. The receiver trajectories are at altitude H_R, at known locations $\boldsymbol{X}_R(t)$ and with velocity $\boldsymbol{V}_R$ assumed constant and horizontal for simplicity. They span a linear synthetic aperture $A_R = |\boldsymbol{V}_R|T_{\rm tot}$ over the duration $T_{\rm tot}$ of time t, and the goal of imaging is to determine the trajectory $\boldsymbol{X}_T(t)$ of a high-flying target from the measurements gathered over this aperture. We study in detail the case of a target in translational motion, at constant horizontal velocity $\boldsymbol{V}_T$ satisfying $|\boldsymbol{V}_T| \gg |\boldsymbol{V}_R|$. This defines a linear ISAR (inverse SAR) aperture $A_T = |\boldsymbol{V}_T|T_{\rm tot}$, at unknown altitude $H_T \gg H_R$. Extensions of the results to general target trajectories $(\boldsymbol{X}_T(t), \boldsymbol{V}_T(t))$, that can be determined by a flow from the initial position and velocity, are briefly addressed.

In both configurations the image is formed by the superposition of cross correlations of the recorded signals, synchronized using travel time delays. The imaging function has the general form used in other passive correlation-based imaging methods [12, 13], but there are Doppler effects that must be taken into account. Such effects are known to be important in satellite active SAR and ISAR (when there is a single, fixed transmitter/receiver antenna and a moving target) [6, 27], and in passive SAR [31, 32, 34, 35]. We use them in our imaging function by introducing Doppler compensation factors in the cross-correlations.

In the configuration with a single receiver platform, illustrated in Figure 1.1, the image is formed with cross correlations of the direct and reflected signals, Doppler compensated and synchronized with travel time delays. The direct arrival time from the transmitter at $\boldsymbol{X}_E$ to the receiver at $\boldsymbol{X}_R(t)$ plays an important role in the synchronization, so the method is highly sensitive to knowing $\boldsymbol{X}_E$. The images also lack robustness with respect to turbulent atmospheric distortions, so single receiver imaging systems are not expected to perform well in high frequency (X-band) regimes. If turbulent effects are negligible and $\boldsymbol{X}_E$ is known, the image resolution is described by the Rayleigh formulas that hold in general passive imaging systems with physical arrays [13], as well as for active ISAR [6, Section 7.3.6]. Indeed, we show that the range resolution, that is, the accuracy in the estimate of the altitude H_T of the target, is inversely proportional to the transmitter bandwidth B, or equivalently, proportional to the transmitter pulse width. The resolution along the direction of the target trajectory is given by $\lambda_o H_T/A_T$, where λ_o is the transmitter central wavelength, and the resolution along the direction of the receiver trajectory is $\lambda_o H_T/A_R$. These resolution formulas are derived from first principles, and are confirmed with detailed numerical simulations. They hold in a marginal sense because they represent focusing in a plane, when the coordinate out of plane and the target velocity are fixed at the correct values. The limited data acquired by the single receiver platform makes it impossible to determine the target trajectory from the image. Without prior information we can estimate at most two components of the target location: its range and cross-range in the direction of the trajectory. Alternatively,

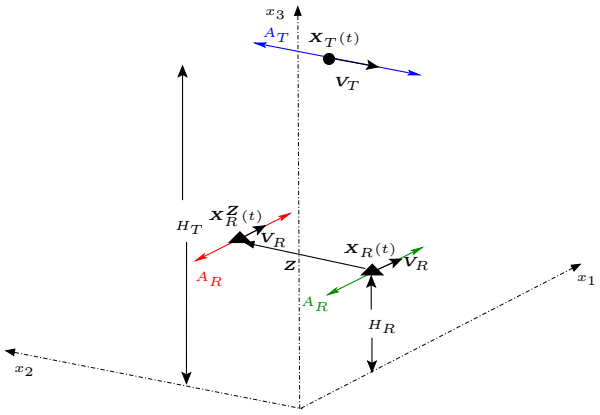

FIGURE 1.2. *Illustration of the imaging setup with a pair of receiver platforms flying at the same speed* $\boldsymbol{V}_R$. *The aperture* A_R *spanned by the receivers at altitude* H_R *is shown in green and red, and the aperture* A_T *spanned by the target at altitude* H_T *is shown in blue. The receivers are separated by* $\boldsymbol{Z}$.

if we knew the location of the target along its trajectory at unknown height H_T, we could determine H_T and the range component of $\boldsymbol{V}_T$.

In the case of multiple receiver platforms, the images are formed with Doppler compensated cross correlations of the reflected signals, synchronized with differences of the travel times of these signals. Were it not for the Doppler effects, the travel times of the direct arrivals from the transmitter would cancel out, and knowledge of $\boldsymbol{X}_E$ would not be needed to form the image. The transmitter location appears in the Doppler corrections, so it does play some role, but as we show in this paper the sensitivity of the image to $\boldsymbol{X}_E$ is low. This is one advantage of this imaging modality. The other advantage is that the cross correlations suppress efficiently atmospheric turbulence effects, as shown in [11, 12]. The images are as good as in homogeneous media, so the resolution theory presented in this paper applies to imaging through turbulence, when the receivers fly above it.

We study the resolution of passive imaging with a pair of receivers separated by vector $\boldsymbol{Z}$, flying at the same constant velocity $\boldsymbol{V}_R$, as illustrated in Figure 1.2. The target range is difficult to estimate in this setup, when the receivers are nearby i.e., for $|\boldsymbol{Z}| \ll H_T$. This is because the range information is almost canceled out in the difference of the travel times of the reflected signals measured at the two receivers. It is the target cross-range location that plays the prominent role, and its estimation is determined by the temporal duration of the pulse, which is of order $1/B$. Explicitly, with $\boldsymbol{Z}$ in the cross-range plane, we obtain that the cross-range resolution in the direction of $\boldsymbol{Z}$ is of order $c_o H_T/(B|\boldsymbol{Z}|)$. The limited data gathered by the single pair of receivers, makes it impossible to localize the target in the other two directions, and also estimate its velocity. We can only get a linear combination of the relative error of the velocity in the direction of $\boldsymbol{Z}$ and of the location in range, with precision of order $\lambda_o H_T/(A_T|\boldsymbol{Z}|)$.

To resolve this ambiguity we consider a second pair of nearby receivers. We quantify the gain brought by the extra measurements, and show that if the two receiver pairs are well separated, it is possible to determine the target trajectory. That is, determine both its velocity and location.

The paper is organized as follows: We begin in section 2 with the mathematical model of the measurements at the receiver platforms. The imaging functions with a single receiver or a pair of receivers are described in sections 3 and 4. We also state there the resolution results, and give their derivations in appendices A and B. In section 5 we present numerical simulations that verify the theoretical resolution estimates, and also illustrate the sensitivity of the images with respect to the location of the transmitter. We end in section 6 with a summary of the results.

2. Data model. We assume as in [23] the wave propagation model

$$\frac{1}{c^2(t,\boldsymbol{x})}\frac{\partial^2 u(t,\boldsymbol{x})}{\partial t^2} - \Delta u(t,\boldsymbol{x}) = f(t)\delta(\boldsymbol{x}-\boldsymbol{X}_E), \tag{2.1}$$

for one component $u(t,\boldsymbol{x})$ of the electromagnetic field, and a time dependent wave speed $c(t,\boldsymbol{x})$ satisfying

$$\frac{1}{c^2(t,\boldsymbol{x})} = \frac{1}{c_o^2}\Big[1+\varrho_T\big(\boldsymbol{x}-\boldsymbol{X}_T(t)\big)\Big]. \tag{2.2}$$

Here ϱ_T is a localized perturbation (with compact support) of the constant background speed c_o, modeling the target located at $\boldsymbol{X}_T(t)$ at time t. The waves are due to the transmitter at $\boldsymbol{X}_E$, which emits the probing pulse

$$f(t) = F(Bt)e^{-i\omega_o t} + F(Bt)e^{i\omega_o t} = 2F(Bt)\cos(\omega_o t). \tag{2.3}$$

The baseband signal F is a real valued function of dimensionless arguments and Fourier transform

$$\widehat{F}(\omega) = \int_{-\infty}^{\infty} ds\, F(s)e^{i\omega s},$$

supported in the interval $[-\pi,\pi]$. The frequency ω_o modulation in (2.3) and the scaling of the argument of F by the bandwidth B gives

$$\widehat{f}(\omega) = \int_{-\infty}^{\infty} dt\, f(t)e^{i\omega t} = \frac{1}{B}\left[\widehat{F}\left(\frac{\omega-\omega_o}{B}\right) + \widehat{F}\left(\frac{\omega+\omega_o}{B}\right)\right],$$

so the frequency support of the emitted pulse is $[\omega_o-\pi B,\omega_o+\pi B]\cup[-\omega_o-\pi B,-\omega_o+\pi B]$. We suppose, as is usual in SAR, that the bandwidth B is much smaller than the central frequency ω_o, moreover, denote the central wavelength by $\lambda_o = 2\pi c_o/\omega_0$.

The wave field $u(t,\boldsymbol{x})$ is measured at the receiver platform locations $\boldsymbol{X}_R(t)$. It consists of the direct wave $u_{\rm d}$, coming straight from $\boldsymbol{X}_E$, and the reflected wave $u_{\rm r}$ scattered at the target. The setup is as illustrated in Figures 1.1 or 1.2, with the receiver platforms having two antennas, one pointing down, towards the Earth, and the other pointing up, so that they can separate the direct and reflected waves. Such wave separation has already been used in other applications, like seismic exploration [11, 21] or passive fathometry [26].

The mathematical models of $u_{\rm d}$ and $u_{\rm r}$, *i.e.*, the component of the signal at the receiver directly transmitted from the source and reflected off the target respectively, are given in the next section, and the Doppler effects due to the motion of the target and receivers are described in section 2.2.

2.1. The direct and reflected waves. Rather than the full Maxwell's system of equations we will use here the simpler scalar wave equation which carries the main features of the scattering problems encountered in radar applications. The scalar model is frequently used in practice as in the recent book [6] and other references therein. Let $u_o(t,\boldsymbol{x})$ be the solution of the wave equation in the uniform medium,

$$\frac{1}{c_o^2}\frac{\partial^2 u_o(t,\boldsymbol{x})}{\partial t^2} - \Delta u_o(t,\boldsymbol{x}) = f(t)\delta(\boldsymbol{x}-\boldsymbol{X}_E), \tag{2.4}$$

which is given by the expression

$$u_o(\boldsymbol{x},t) = \frac{1}{4\pi\,|\boldsymbol{x}-\boldsymbol{X}_E|} f\left(t-\frac{|\boldsymbol{x}-\boldsymbol{X}_E|}{c_o}\right).$$

We define the direct and reflected waves at the receiver location $\boldsymbol{X}_R(t)$ by

$$u_{\rm d}(t) = u_o(t,\boldsymbol{X}_R(t)) \quad \text{and} \quad u_{\rm r}(t) = u(t,\boldsymbol{X}_R(t)) - u_o(t,\boldsymbol{X}_R(t)). \tag{2.5}$$

We use equations (2.1) and (2.2), and assume that the target is small (point-like) to derive the mathematical expressions of $u_{\rm d}(t)$ and $u_{\rm r}(t)$ stated in the next proposition.

PROPOSITION 2.1. *The direct wave is given by*

$$u_{\rm d}(t) = \frac{1}{4\pi\,|\boldsymbol{X}_R(t)-\boldsymbol{X}_E|} f\left(t-\frac{|\boldsymbol{X}_R(t)-\boldsymbol{X}_E|}{c_o}\right), \tag{2.6}$$

and the reflected wave is approximately

$$u_{\rm r}(t) \approx -\frac{\rho f''\Big(\tau(t) - \frac{|\boldsymbol{X}_T(\tau(t))-\boldsymbol{X}_E|}{c_o}\Big)}{(4\pi)^2 c_o^2 |\boldsymbol{X}_T(\tau(t)) - \boldsymbol{X}_E||\boldsymbol{X}_R(t) - \boldsymbol{X}_T(\tau(t))| \left|1 + \frac{\boldsymbol{V}_T}{c_o}\cdot\frac{(\boldsymbol{D}(t)-(t-\tau(t))\boldsymbol{V}_T)}{|(\boldsymbol{D}(t)-(t-\tau(t))\boldsymbol{V}_T|}\right|}, \tag{2.7}$$

where $\rho = \int d\boldsymbol{x}\, \varrho_T(\boldsymbol{x})$ *is the net target reflectivity,*

$$\boldsymbol{D}(t) = \boldsymbol{X}_T(0) - \boldsymbol{X}_R(0) + t(\boldsymbol{V}_T - \boldsymbol{V}_R). \tag{2.8}$$

and

$$\tau(t) = t - \frac{|\boldsymbol{D}(t)|}{c_o\left(1 - \left|\frac{\boldsymbol{V}_T}{c_o}\right|^2\right)}\left[\sqrt{1 - \left|\frac{\boldsymbol{V}_T}{c_o}\right|^2 + \left(\frac{\boldsymbol{V}_T}{c_o}\cdot\frac{\boldsymbol{D}(t)}{|\boldsymbol{D}(t)|}\right)^2} - \frac{\boldsymbol{V}_T}{c_o}\cdot\frac{\boldsymbol{D}(t)}{|\boldsymbol{D}(t)|}\right]. \tag{2.9}$$

Proof: Since the solution of (2.4) is just the time convolution of the pulse with the Green's function

$$G(t,\boldsymbol{x},\boldsymbol{y}) = \frac{\delta\left(t - \frac{|\boldsymbol{x}-\boldsymbol{y}|}{c_o}\right)}{4\pi\,|\boldsymbol{x}-\boldsymbol{y}|}, \tag{2.10}$$

equation (2.6) follows from definition (2.5). The scattered wave $u(t,\boldsymbol{x}) - u_o(t,\boldsymbol{x})$ may be modeled with the Born approximation, because the target is small. Equations (2.1) and (2.2) give in this approximation that

$$\begin{aligned} u(t,\boldsymbol{x}) - u_o(t,\boldsymbol{x}) &\approx -\frac{1}{c_o^2}\int_0^t d\tau \int_{\mathbb{R}^3} d\boldsymbol{y}\, G\left(t-\tau,\boldsymbol{x},\boldsymbol{y}\right)\varrho_T\left(\boldsymbol{y} - \boldsymbol{X}_T(\tau)\right)\frac{\partial^2}{\partial\tau^2}u_o(\tau,\boldsymbol{y}) \\ &\approx -\frac{\rho}{c_o^2}\int_0^t d\tau\, G(t-\tau,\boldsymbol{x},\boldsymbol{X}_T(\tau))\frac{\partial^2}{\partial\tau^2}u_o(\tau,\boldsymbol{y})\mid_{\boldsymbol{y}=\boldsymbol{X}_T(\tau)}. \end{aligned}$$

The first line is obtained in the Born (or single-scattering) approximation and the second line is obtained for the point-like target approximation. Substituting the expression of u_o in the right hand side and integrating by parts twice, we obtain

$$u(t,\boldsymbol{x}) - u_o(t,\boldsymbol{x}) \approx -\frac{\rho}{c_o^2}\int_0^t d\tau \int_0^\tau d\tau' f''(\tau') G\left(\tau-\tau',\boldsymbol{X}_T(\tau),\boldsymbol{X}_E\right) G\left(t-\tau,\boldsymbol{x},\boldsymbol{X}_T(\tau)\right).$$

The reflected wave field follows from definitions (2.5) and (2.10),

$$u_{\rm r}(t) = -\frac{\rho}{c_o^2}\int_0^t d\tau\, \frac{f''\Big(\tau - \frac{|\boldsymbol{X}_T(\tau)-\boldsymbol{X}_E|}{c_o}\Big)}{4\pi|\boldsymbol{X}_T(\tau)-\boldsymbol{X}_E|}\frac{\delta\Big(t-\tau-\frac{|\boldsymbol{X}_R(t)-\boldsymbol{X}_T(\tau)|}{c_o}\Big)}{4\pi|\boldsymbol{X}_R(t)-\boldsymbol{X}_T(\tau)|}.$$

Let us introduce

$$\Phi(\tau;t) = t - \tau - \frac{|\boldsymbol{X}_T(0) - \boldsymbol{X}_R(0) + t(\boldsymbol{V}_T - \boldsymbol{V}_R) - (t-\tau)\boldsymbol{V}_T|}{c_o},$$

and use that

$$\delta\left[\Phi(\tau;t)\right] = \frac{\delta[\tau - \tau(t)]}{|\partial_\tau\Phi(\tau(t);t)|},$$

with $\tau(t)$ the unique zero of the mapping $\tau \to \Phi(\tau;t)$ in $(0,t)$. This can be found from the quadratic equation

$$(t-\tau)^2 = \frac{|\boldsymbol{X}_T(0) - \boldsymbol{X}_R(0) + t(\boldsymbol{V}_T - \boldsymbol{V}_R) - (t-\tau)\boldsymbol{V}_T|^2}{c_o^2}.$$

Choosing the root that is smaller than t, we obtain (2.9). We also have

$$|\partial_\tau\Phi(\tau(t);t)| = \left|1 + \frac{\boldsymbol{V}_T}{c_o}\cdot\frac{[\boldsymbol{D}(t) - (t-\tau(t))\boldsymbol{V}_T]}{|\boldsymbol{D}(t) - (t-\tau(t))\boldsymbol{V}_T|}\right|.$$

Equation (2.7) follows by substituting these results in the expression of $u_{\rm r}(t)$ above.

2.2. Doppler factors. The transmitter emits pulses sequentially, at slow time instances s separated by Δs. We call s slow time because the pulse repetition interval Δs is much larger than the travel time of the waves from the emitter to the target and then to the receiver. The fast time t parametrizes the wave recordings between each emission, and satisfies $0 \leq t < \Delta s$. The result in the next proposition is obtained using this scale separation. It shows that the direct and reflected waves described in Proposition 2.1 can be approximated by some geometrical spreading amplitude factors multiplied with the time delayed and Doppler deformed pulse or its second derivative. This tells us how to synchronize the waves when we form images in sections 3 and 4.

PROPOSITION 2.2. *Let $u_{\rm d}(s+t)$ and $u_{\rm r}(s+t)$ be the direct and reflected waves defined in Proposition 2.1, for a pulse emitted at slow time s, and fast time t satisfying $0 \leq t < \Delta s$. Then, the expressions* (2.6) *and* (2.7) *can be approximated by*

$$u_{\rm d}(s+t) \approx \frac{f\big(\gamma_{\rm d}(s)t - t_{\rm d}(s)\big)}{4\pi|\boldsymbol{X}_R(s) - \boldsymbol{X}_E|}, \tag{2.11}$$

and

$$u_{\rm r}(s+t) \approx -\frac{\rho f''\Big(\gamma_{\rm r}(s, \boldsymbol{Y}_T, \boldsymbol{V}_T)t - t_{\rm r}(s, \boldsymbol{Y}_T, \boldsymbol{V}_T)\Big)}{(4\pi)^2 c_o^2 |\boldsymbol{X}_T(s)|^2}, \tag{2.12}$$

where $\boldsymbol{Y}_T = X_T(s) - s\boldsymbol{V}_T$ is the location of the target at the origin of the slow time. The travel time delay of the direct arrival is

$$t_{\rm d}(s) = |\boldsymbol{X}_R(s) - \boldsymbol{X}_E|/c_o, \tag{2.13}$$

and the delay of the reflected arrival is

$$t_{\rm r}(s, \boldsymbol{Y}_T, \boldsymbol{V}_T) = |\boldsymbol{X}_T(s) - \boldsymbol{X}_E|/c_o + \tilde{\gamma}_{\rm r}(s, \boldsymbol{Y}_T, \boldsymbol{V}_T)|\boldsymbol{X}_T(s) - \boldsymbol{X}_R(s)|/c_o. \tag{2.14}$$

The motion of the receiver causes the following Doppler factor in the direct signal

$$\gamma_{\rm d}(s) = 1 - \frac{\boldsymbol{V}_R}{c_o} \cdot \boldsymbol{m}_{RE}(s), \qquad \boldsymbol{m}_{RE}(s) = \frac{\boldsymbol{X}_R(s) - \boldsymbol{X}_E}{|\boldsymbol{X}_R(s) - \boldsymbol{X}_E|}, \tag{2.15}$$

with $\boldsymbol{m}_{RE}$ the unit vector pointing from the transmitter to the receiver. There are two Doppler factors in the reflected signal. The first is for the wave going from the transmitter to the moving target

$$\tilde{\gamma}_{\rm r}(s, \boldsymbol{Y}_T, \boldsymbol{V}_T) = 1 - \frac{\boldsymbol{V}_T}{c_o} \cdot \left[\boldsymbol{m}_{TE}(s) + \boldsymbol{m}_{TR}(s)\right], \tag{2.16}$$

and the second is for the wave going from the transmitter to the target, and then to the receiver

$$\gamma_{\rm r}(s, \boldsymbol{Y}_T, \boldsymbol{V}_T) \quad = 1 - \frac{\boldsymbol{V}_T}{c_o} \cdot \left[\boldsymbol{m}_{TE}(s) + \boldsymbol{m}_{TR}(s)\right] + \frac{\boldsymbol{V}_R}{c_o} \cdot \boldsymbol{m}_{TR}(s). \tag{2.17}$$

They are both determined by projections of the velocities $\boldsymbol{V}_T$ and $\boldsymbol{V}_R$ on the unit vectors

$$\boldsymbol{m}_{TE}(s) = \frac{\boldsymbol{X}_T(s) - \boldsymbol{X}_E}{|\boldsymbol{X}_T(s) - \boldsymbol{X}_E|}, \qquad \boldsymbol{m}_{TR}(s) = \frac{\boldsymbol{X}_T(s) - \boldsymbol{X}_R(s)}{|\boldsymbol{X}_T(s) - \boldsymbol{X}_R(s)|}. \tag{2.18}$$

Proof: Equations (2.11) and (2.12) follow from Proposition 2.1 and the following linear (in t) approximations

$$|\boldsymbol{X}_R(s+t) - \boldsymbol{X}_E| \approx |\boldsymbol{X}_R(s) - \boldsymbol{X}_E| + t\boldsymbol{V}_R \cdot \frac{\boldsymbol{X}_R(s) - \boldsymbol{X}_E}{|\boldsymbol{X}_R(s) - \boldsymbol{X}_E|},$$

$$|\boldsymbol{X}_T(s+t') - \boldsymbol{X}_E| \approx |\boldsymbol{X}_T(s) - \boldsymbol{X}_E| + t'\boldsymbol{V}_T \cdot \frac{\boldsymbol{X}_T(s) - \boldsymbol{X}_E}{|\boldsymbol{X}_T(s) - \boldsymbol{X}_E|},$$

$$|\boldsymbol{X}_T(s+t') - \boldsymbol{X}_R(s+t)| \approx |\boldsymbol{X}_T(s) - \boldsymbol{X}_R(s)| + \big(t'\boldsymbol{V}_T - t\boldsymbol{V}_R\big) \cdot \frac{\boldsymbol{X}_T(s) - \boldsymbol{X}_R(s)}{|\boldsymbol{X}_T(s) - |\boldsymbol{X}_R(s)|}.$$

These are justified in the appendix, were we carry out a detailed multiscale analysis, which takes into account that $|\boldsymbol{X}_T(t)| \gg |\boldsymbol{X}_R(t)|,\ |\boldsymbol{X}_E|$.

3. Imaging with one receiver. In this section we present a correlation-based imaging function for the configuration with one receiver platform. It is similar to the imaging function introduced recently in [12], except that it takes into consideration the fast motion of the target and receiver using the Doppler factors in Proposition 2.2. These factors must be estimated locally, because they depend on the locations of the target and receiver. This motivates us to consider first imaging over a small sub-aperture, and then form the final image by summing over the sub-apertures. Small apertures are also useful when the target and receiver have more complicated trajectories than the linear ones assumed here. Such trajectories have piece-wise linear approximations, for properly calibrated aperture segmentations, as shown in [3].

We take for convenience the observation time window $(-T_{\rm tot}/2, T_{\rm tot}/2)$, centered at the origin of the slow time, when the target is located at $\boldsymbol{Y}_T$. The observation time $T_{\rm tot}$ defines the target and receiver apertures A_T and A_R. We divide them into sub-apertures

$$a_T = |\boldsymbol{V}_T|\Delta S, \quad a_R = |\boldsymbol{V}_R|\Delta S,$$

corresponding to slow time intervals of duration ΔS. Let $N = \lfloor T_{\rm tot}/\Delta S \rfloor - 1$ then we have $N+1$ such intervals centered at $S_j = j\Delta S$, for $j = -N/2, \ldots, N/2$. Within each $j-$th sub-aperture we denote the slow time by

$$s_{jl} = S_j + l\Delta s, \quad l = -n/2, \ldots, n/2,$$

for $n = \lfloor \Delta S/\Delta s \rfloor - 1$. Both N and n are assumed even.

The sub-aperture imaging function is discussed in section 3.1. The final image is obtained by summing over the sub-apertures. We describe its resolution limits in section 3.2. The results are for uniform translational motion of the target and receiver, and therefore linear trajectories. We address briefly extensions to general trajectories in section 3.3.

3.1. Small aperture imaging function. The results in Proposition 2.2 show that both the direct and reflected signals recorded at the receiver platform have the form of the pulse profile (or its second derivative), time-delayed by travel times and scaled and deformed by Doppler factors. Any matched filter or correlation-based imaging function must compensate for these Doppler factors, as seen for example in [27] or [10, 31, 32, 34, 35]. Motivated by this line of research we define our imaging function $\mathcal{I}_j(\boldsymbol{X}, \boldsymbol{V})$ for the $j-$th aperture as follows:

$$\mathcal{I}_j(\boldsymbol{X}, \boldsymbol{V}) = \frac{1}{n} \sum_{l=-n/2}^{n/2} \int_{-\Delta s/2}^{\Delta s/2} dt\, u_{\rm d}\left(s_{jl} + \frac{t + t_{\rm d}(s_{jl})}{\gamma_{\rm d}(s_{jl})} \right) u_{\rm r}\left(s_{jl} + \frac{t + t_{\rm r}(s_{jl} - S_j, \boldsymbol{X}, \boldsymbol{V})}{\gamma_{\rm r}(s_{jl} - S_j, \boldsymbol{X}, \boldsymbol{V})} \right), \tag{3.1}$$

where $\boldsymbol{X}$ and $\boldsymbol{V}$ are the search vectors for $\boldsymbol{X}_T(S_j) = \boldsymbol{Y}_T + S_j\Delta S$ and $\boldsymbol{V}_T$. The time integral in (3.1) is over a duration of at most Δs, the pulse repetition interval. In fact, in practice, it would be sufficient for this duration to be slightly longer than that of $f(t)$, so that we can capture the whole pulse profile even if the emission times are only approximately known. The sum over l in (3.1) is as usual in synthetic aperture imaging from repeated probing pulses. However, each term is the cross correlation of the signal received directly from the transmitter and the reflected signal. Both signals are scaled by their respective Doppler factors defined in section 2.2.

PROPOSITION 3.1. *In the scaling regime*

$$|\boldsymbol{X}_E|, |\boldsymbol{X}_R| = O(H_R), \quad |\boldsymbol{X}_T| = O(H_T), \quad H_R \ll H_T, \tag{3.2}$$

where the target is at high altitude and moves at large speed $|\boldsymbol{V}_T| \gg |\boldsymbol{V}_R|$, the imaging function (3.1) *is large when the relative errors in the target location and velocity satisfy*

$$\left| \frac{(\boldsymbol{X}_T(S_j) - \boldsymbol{X})}{|\boldsymbol{X}_T(S_j)|} \cdot \boldsymbol{m}(S_j) + \mathcal{E}_1 \right| = O\left(\frac{c_o}{BH_T} \right), \tag{3.3}$$

and

$$\left| \frac{(\boldsymbol{V}_T - \boldsymbol{V})}{|\boldsymbol{V}_T|} \cdot \boldsymbol{m}(S_j) + \frac{(\boldsymbol{X}_T(S_j) - \boldsymbol{X})}{|\boldsymbol{X}_T(S_j)|} \cdot \frac{\mathbf{P}(S_j)\boldsymbol{V}_T}{|\boldsymbol{V}_T|} + \mathcal{E}_2 \right| = O\left(\frac{\lambda_o}{a_T} \right). \tag{3.4}$$

Here the unit vector

$$\boldsymbol{m}(S_j) = \frac{\boldsymbol{X}_T(S_j)}{|\boldsymbol{X}_T(S_j)|} \tag{3.5}$$

defines the range direction for the sub-aperture, pointing toward the location of the target, and

$$\mathbf{P}(S_j) = \mathbf{I} - \boldsymbol{m}(S_j)\boldsymbol{m}(S_j)^T \tag{3.6}$$

is the orthogonal projection on the cross-range plane orthogonal to $\boldsymbol{m}(S_j)$ *(*$\mathbf{I}$ *is the* 3×3 *identity matrix). The residuals in the estimates* (3.3) *and* (3.4) *are*

$$\mathcal{E}_1 = \left(\frac{\boldsymbol{X}_E}{2|\boldsymbol{X}_T(S_j)|} + \frac{\boldsymbol{X}_R(S_j)}{2|\boldsymbol{X}_T(S_j)|} \right) \cdot \frac{\mathbf{P}(S_j)(\boldsymbol{X}_T(S_j) - \boldsymbol{X})}{|\boldsymbol{X}_T(S_j)|}, \tag{3.7}$$

and

$$\mathcal{E}_2 = \left(\frac{\boldsymbol{X}_E}{2|\boldsymbol{X}_T(S_j)|} + \frac{\boldsymbol{X}_R(S_j)}{2|\boldsymbol{X}_T(S_j)|} \right) \cdot \frac{\mathbf{P}(S_j)(\boldsymbol{V}_T - \boldsymbol{V})}{|\boldsymbol{V}_T|} + \frac{\boldsymbol{V}_R}{|\boldsymbol{V}_T|} \cdot \frac{\mathbf{P}(S_j)(\boldsymbol{X}_T(S_j) - \boldsymbol{X})}{|\boldsymbol{X}_T(S_j)|}. \tag{3.8}$$

They play a minor role because they are determined by the relative errors in the target location and velocity, multiplied by small factors of order $O(H_R/H_T)$ *and* $O(|\boldsymbol{V}_R|/|\boldsymbol{V}_T|)$*, respectively.*

The resolution limits (3.3) and (3.4) are derived in appendix A, where we carry out a detailed multiscale analysis of the imaging function (3.1).

Equation (3.3) is due to the inaccuracy of the travel time estimation, which is of the order of $1/B$, the temporal duration of the probing pulse. Because the source and receiver locations are known, the travel time that plays a role in (3.1) is from the transmitter at $\boldsymbol{X}_E$ to the target at $\boldsymbol{X}_T$ and then back to the receiver at $\boldsymbol{X}_R$. By assumption (3.2) this time is approximately $2H_T/c_o$, and

$$H_T \approx \boldsymbol{X}_T(S_j) \cdot \boldsymbol{m}(S_j).$$

Thus, we can estimate the range with a precision of order c_o/B, as stated in (3.3). This is the classic Rayleigh range resolution limit.

Equation (3.4) is obtained by the coherent summation of the time synchronized cross-correlations over the sub-aperture a_T. It involves the linear combination of the relative errors of the range velocity and the cross-range target location. It is a marginal resolution result because it allows us to estimate either the velocity or the location, but not both:

- If we fix the search location $\boldsymbol{X}$ at the target cross-range, we get

$$\left| \frac{(\boldsymbol{V}_T - \boldsymbol{V})}{|\boldsymbol{V}_T|} \cdot \boldsymbol{m}(S_j) \right| \leq O\left(\frac{\lambda_o}{a_T} \right). \tag{3.9}$$

This is an excellent estimate of the velocity of the target in the range direction, that amounts to a sub-wavelength error of the target trajectory over the sub-aperture a_T.

- If we fix the range velocity at the correct value, we get

$$\left| (\boldsymbol{X}_T(S_j) - \boldsymbol{X}) \cdot \frac{\mathbf{P}(S_j)\boldsymbol{V}_T}{|\boldsymbol{V}_T|} \right| \leq O\left(\frac{\lambda_o H_T}{a_T} \right). \tag{3.10}$$

Because $\boldsymbol{V}_T$ is horizontal,

$$\mathbf{P}(S_j)\boldsymbol{V}_T \approx \boldsymbol{V}_T,$$

so (3.10) is the expected Rayleigh cross-range resolution formula for ISAR, with synthetic aperture a_T determined by the motion of the target. It says that the target location along the direction of the flight path is determined by the wavelength multiplied by the ratio of the target range and the aperture.

The target location in the direction orthogonal to $\boldsymbol{V}_T$ is practically impossible to determine from $\mathcal{I}_j$. It appears only in the residuals $\mathcal{E}_1$ and $\mathcal{E}_2$, and to see it we need to cancel the leading terms in equations (3.3) and (3.4). For example, if we knew the range location of the target, we could get from (3.3) and (3.7) some cross-range estimate of the order $c_o H_T/(BH_R)$. Otherwise, if we knew the target velocity and its cross-range location along the trajectory, and if $\boldsymbol{V}_R$ were orthogonal to $\boldsymbol{V}_T$, we could get from (3.4) and (3.8) that

$$\left|(\boldsymbol{X}_T(S_j)-\boldsymbol{X})\cdot\frac{\mathbf{P}(S_j)\boldsymbol{V}_R}{|\boldsymbol{V}_R|}\right| \approx \left|(\boldsymbol{X}_T(S_j)-\boldsymbol{X})\cdot\frac{\boldsymbol{V}_R}{|\boldsymbol{V}_R|}\right| \leq O\left(\frac{\lambda_o H_T}{a_R}\right). \tag{3.11}$$

This is the Rayleigh resolution formula for SAR, with synthetic aperture a_R determined by the motion of the receiver. The estimate is worse for other orientations of $\boldsymbol{V}_R$.

3.2. Imaging with a large aperture. We sum coherently the small aperture imaging functions (3.1) over j to form the full aperture imaging function:

$$\mathcal{I}(\boldsymbol{Y},\boldsymbol{V}) = \sum_{j=-N/2}^{N/2} \mathcal{I}_j(\boldsymbol{Y}+S_j\boldsymbol{V},\boldsymbol{V}), \tag{3.12}$$

Because the target has a linear trajectory, we have $\boldsymbol{X}_T(S_j) = \boldsymbol{Y}_T + S_j\boldsymbol{V}_T$, and the search points $\boldsymbol{X}$ satisfy similarly $\boldsymbol{X} = \boldsymbol{Y} + S_j\boldsymbol{V}$. The unknowns are $\boldsymbol{Y}_T$ and $\boldsymbol{V}_T$, which is why we parametrize the images (3.12) by the search location $\boldsymbol{Y}$ and velocity $\boldsymbol{V}$.

It is difficult to derive analytically the resolution limits of $\mathcal{I}$ for arbitrarily large synthetic aperture A_T defined by the motion of the target. However, when $A_T \ll H_T$, all the range directions are approximately aligned with $\boldsymbol{Y}_T$,

$$\boldsymbol{m}(S_j) = \frac{\boldsymbol{Y}_T + S_j\boldsymbol{V}_T}{|\boldsymbol{Y}_T + S_j\boldsymbol{V}_T|} \approx \boldsymbol{m}(0) = \frac{\boldsymbol{Y}_T}{|\boldsymbol{Y}_T|},$$

and $|\boldsymbol{Y}_T| \approx H_T$. Then, we show in appendix A.4 that $\mathcal{I}(\boldsymbol{Y},\boldsymbol{V})$ is large when

$$|(\boldsymbol{Y}_T-\boldsymbol{Y})\cdot\boldsymbol{m}(0)| \leq O\left(\frac{c_o}{B}\right), \tag{3.13}$$

and

$$\left|\frac{\boldsymbol{V}_T-\boldsymbol{V}}{|\boldsymbol{V}_T|}\cdot\boldsymbol{m}(0) + \frac{\boldsymbol{V}_T}{|\boldsymbol{V}_T|}\cdot\frac{\mathbf{P}(0)(\boldsymbol{Y}_T-\boldsymbol{Y})}{|\boldsymbol{Y}_T|}\right| \leq O\left(\frac{\lambda_o}{A_T}\right). \tag{3.14}$$

The sum over the sub-apertures does not affect the range estimate (3.13), which stays of order c_o/B, but it improves the estimate (3.14) because $A_T \gg a_T$.

Additionally, if $\boldsymbol{Y} = \boldsymbol{Y}_T$ and $(\boldsymbol{V}-\boldsymbol{V}_T)\cdot\boldsymbol{m}(0) = 0$, then it is shown in appendix A.4 that $\mathcal{I}(\boldsymbol{Y}_T,\boldsymbol{V})$ is large when

$$\left|\frac{\boldsymbol{V}_T-\boldsymbol{V}}{|\boldsymbol{V}_T|}\cdot\frac{\boldsymbol{V}_T}{|\boldsymbol{V}_T|}\right| \leq O\left(\frac{\lambda_o H_T}{A_T^2}\right). \tag{3.15}$$

Note that even with the large aperture the imaging function with a single transmitter and receiver platform cannot determine both the target location and velocity. Moreover, all the information is restricted to the plane spanned by $\boldsymbol{Y}_T$ and $\boldsymbol{V}_T$. These ambiguities are expected and are as in active monostatic SAR systems, because the data are two-dimensional, parametrized by the slow time (location of the receiver) and the fast time. More measurements are needed to resolve these ambiguities, either from multiple transmitters or receivers, separated by large distances of the order of H_T, as explained in section 4.

3.3. Extensions to general trajectories. Our simplifying assumption of constant velocity of the target and receiver can be relaxed to account for more general motion. Suppose that the target has a

deterministic trajectory, determined by the gravitational force and its initial location $\boldsymbol{X}_T^{\rm in}$ and velocity $\boldsymbol{V}_T^{\rm in}$. Then, $(\boldsymbol{X}_T(s), \boldsymbol{V}_T(s))$ is the unique solution of the differential equation

$$\frac{d}{ds}\begin{pmatrix}\boldsymbol{X}_T(s)\\ \boldsymbol{V}_T(s)\end{pmatrix} = \begin{pmatrix}\boldsymbol{V}_T(s)\\ -\frac{g}{m}\frac{\boldsymbol{X}_T(s)}{|\boldsymbol{X}_T(s)|}\end{pmatrix}, \quad s \in (-T_{\rm tot}/2, T_{\rm tot}/2),$$

with initial condition

$$\boldsymbol{X}_T(-T_{\rm tot}/2) = \boldsymbol{X}_T^{\rm in}, \qquad \boldsymbol{V}_T(-T_{\rm tot}/2) = \boldsymbol{V}_T^{\rm in},$$

where g is the gravitational acceleration and m is the mass of the target.

When imaging, we can approximate such a trajectory as piecewise linear, using appropriate aperture segmentation, as in [3]. This amounts to taking constant velocities $\boldsymbol{V}_T(S_j)$ and $\boldsymbol{V}_R(S_j)$ in each sub-aperture. The results in Proposition 3.1 extend verbatim to this case. Moreover, the sub-aperture results can be combined in the large aperture function

$$\mathcal{I}(\boldsymbol{X}^{\rm in}, \boldsymbol{V}^{\rm in}) = \sum_{j=-N/2+1}^{N/2-1} \mathcal{I}_j(\boldsymbol{X}(S_j; \boldsymbol{X}^{\rm in}, \boldsymbol{V}^{\rm in}), \boldsymbol{V}(S_j; \boldsymbol{X}^{\rm in}, \boldsymbol{V}^{\rm in})).$$

It searches at $\boldsymbol{X}^{\rm in}$ and $\boldsymbol{V}_T^{\rm in}$ the initial location and velocity of the target, and the arguments in the sum are defined by the piecewise linear flow

$$\boldsymbol{X}(s + S_j; \boldsymbol{X}^{\rm in}, \boldsymbol{V}^{\rm in}) = \boldsymbol{X}(S_j; \boldsymbol{X}^{\rm in}, \boldsymbol{V}^{\rm in}) + (s - S_j)\boldsymbol{V}(S_j; \boldsymbol{X}^{\rm in}, \boldsymbol{V}^{\rm in}), \qquad s \in (S_j, S_j + \Delta S),$$

with

$$\boldsymbol{V}(S_j; \boldsymbol{X}^{\rm in}, \boldsymbol{V}^{\rm in}) = \boldsymbol{V}(S_{j-1}; \boldsymbol{X}^{\rm in}, \boldsymbol{V}^{\rm in}) - \frac{g\Delta S}{m}\frac{\boldsymbol{X}(S_{j-1}; \boldsymbol{X}^{\rm in}, \boldsymbol{V}^{\rm in})}{|\boldsymbol{X}(S_{j-1}; \boldsymbol{X}^{\rm in}, \boldsymbol{V}^{\rm in})|},$$

for $j = -N/2 + 1, \ldots, N/2$, and

$$\boldsymbol{X}(S_{-N/2}; \boldsymbol{X}^{\rm in}, \boldsymbol{V}^{\rm in}) = \boldsymbol{X}^{\rm in}, \quad \boldsymbol{V}(S_{-N/2}; \boldsymbol{X}^{\rm in}, \boldsymbol{V}^{\rm in}) = \boldsymbol{V}^{\rm in}.$$

Recall that the receiver location and velocity are assumed known.

4. Imaging with multiple receiver platforms. In this section we describe the imaging function with multiple receiver platforms. We begin in section 4.1 with one pair of receivers, flying in tandem, and then describe in section 4.2 the result for two pairs of receivers. We assume throughout the section that the target and receivers travel at constant speeds.

4.1. One pair of receivers. Let us consider a pair of receivers flying side by side, at the same constant velocity $\boldsymbol{V}_R$. They are located at $\boldsymbol{X}_R(s)$ and $\boldsymbol{X}_R^Z(s) = \boldsymbol{X}_R(s) + \boldsymbol{Z}$, with constant offset vector $\boldsymbol{Z}$ for all $s \in (-T_{\rm tot}/2, T_{\rm tot}/2)$. We study imaging in the scaling regime

$$|\boldsymbol{X}_E|, |\boldsymbol{X}_R|, |\boldsymbol{Z}| = O(H_R), \quad |\boldsymbol{X}_T| = O(H_T), \quad H_R \ll H_T, \tag{4.1}$$

which is similar to that in the one receiver case, with the additional scale $|\boldsymbol{Z}|$ that is at most of the order of the receiver height. The model of the data recorded at the first receiver is as in Proposition 2.2. For the second receiver we have a similar model, and we denote by $u_{\rm r}^Z$ the reflected signal recorded by it. It depends on the Doppler factors $\gamma_{\rm r}^Z$ and $\tilde{\gamma}_{\rm r}^Z$ and the delay time $t_{\rm r}^Z$, resulting from the replacement of $\boldsymbol{X}_R$ by $\boldsymbol{X}_R + \boldsymbol{Z}$ in the formulas in Proposition 2.2.

The imaging function for the $j-$th sub-aperture is

$$\mathcal{I}_j(\boldsymbol{X}, \boldsymbol{V}) = \frac{1}{n}\sum_{l=-n/2}^{n/2}\int_{-\Delta s/2}^{\Delta s/2} dt\, u_{\rm r}\left(s_{jl} + \frac{t + t_{\rm r}(s_{jl} - S_j, \boldsymbol{X}, \boldsymbol{V})}{\gamma_{\rm r}(s_{jl} - S_j, \boldsymbol{X}, \boldsymbol{V})}\right) u_{\rm r}^Z\left(s_{jl} + \frac{t + t_{\rm r}^Z(s_{jl} - S_j, \boldsymbol{X}, \boldsymbol{V})}{\gamma_{\rm r}^Z(s_{jl} - S_j, \boldsymbol{X}, \boldsymbol{V})}\right). \tag{4.2}$$

It differs from the imaging function (3.1) in the previous section by the fact that it uses cross correlations of the reflected signals measured by the two receivers. This is important for at least two reasons: First, it leads to new resolution results that are no longer like the classic Rayleigh resolution limits, as stated in the next proposition. Second, the cross correlations in (4.2) essentially remove the wave propagation effects from the transmitter to the receivers. This is why the image (4.2) is not affected by wave distortions caused by scattering in the turbulent atmosphere below the receivers, and it is only weakly sensitive to knowledge of the transmitter location. We do not consider atmospheric turbulence in this paper, but refer to [11] and [13, Chapter 10] for studies of robustness of this type of passive imaging in scattering media. The robustness with respect to the knowledge of $\boldsymbol{X}_E$ is illustrated with numerical simulations in section 5. A passive imaging functional which is similar to (4.2) has been introduced and studied in [29] and [30] for imaging and estimating the velocity of ground moving targets. In this case the scattered waves are due to transmitters of opportunity, such as cell phone towers. The analysis in the imaging configuration considered here is different and reveals the significant effect of the inverse SAR aperture due the high speed of the moving object (satellite).

PROPOSITION 4.1. *Under the scaling assumptions* (4.1) *and for* $|\boldsymbol{V}_T| \gg |\boldsymbol{V}_R|$*, the imaging function* (4.2) *is large when the following two conditions are fulfilled:*

$$\left| \frac{\mathbf{P}(S_j)\boldsymbol{Z}}{|\boldsymbol{Z}|} \cdot \frac{(\boldsymbol{X}_T(S_j) - \boldsymbol{X})}{|\boldsymbol{X}_T(S_j)|} + \mathcal{E}_3 \right| \leq O\left(\frac{c_o}{B|\boldsymbol{Z}|} \right), \tag{4.3}$$

and

$$\left| \frac{\mathbf{P}(S_j)\boldsymbol{Z}}{|\boldsymbol{Z}|} \cdot \frac{(\boldsymbol{V}_T - \boldsymbol{V})}{|\boldsymbol{V}_T|} - \frac{Z_{\parallel}}{|\boldsymbol{Z}|} \boldsymbol{m}(S_j) \cdot \frac{(\boldsymbol{X}_T(S_j) - \boldsymbol{X})}{|\boldsymbol{X}_T(S_j)|} + \mathcal{E}_4 \right| \leq O\left(\frac{\lambda_o H_T}{a_T |\boldsymbol{Z}|} \right). \tag{4.4}$$

Here $Z_{\parallel} = \boldsymbol{Z} \cdot \boldsymbol{V}_T / |\boldsymbol{V}_T|$*, is the projection of the receiver offset on the direction of the target trajectory,* $\boldsymbol{m}(S_j)$ *is the unit vector* (3.5) *that defines the range direction, and* $\mathbf{P}(S_j)$ *is the orthogonal projection on the cross-range plane* (3.6)*. The residuals* $\mathcal{E}_3$ *and* $\mathcal{E}_4$ *play a minor role, and are determined by the relative errors of the target location and velocity, multiplied by small factors of order* H_R/H_T *and* $|\boldsymbol{V}_R|/|\boldsymbol{V}_T|$*.*

The derivation of the resolution limits (4.3) and (4.4) is in appendix B.

Equation (4.3) is due to the inaccuracy of the travel time estimation, of the order of the duration $1/B$ of the probing pulse. Because the image (4.2) is formed with cross correlations of the reflected signals at the two receivers, the difference of the travel times of these signals comes into play. The receiver separation is much smaller than the range of the target by scaling assumption (4.1), so the range information almost cancels out in this difference. This is why we can only determine the cross-range location of the target, as stated in (4.3).

The estimate (4.4) is due to the summation over the sub-apertures. It differs from the estimate (3.4) obtained in the one receiver case in two ways: First, (3.4) involves the range velocity and cross-range target location, whereas in (4.4) we have the cross-range velocity and the range target location, each multiplied by projections of the unit vector $\boldsymbol{Z}/|\boldsymbol{Z}|$. Second, the error bound in (4.4) is worse than in (3.4), by a large factor of order $H_T/|\boldsymbol{Z}|$.

It is clear from (4.3) and (4.4) that the best estimates are obtained with offset vectors $\boldsymbol{Z}$ that are in the cross-range plane, which is basically horizontal in our case. Then, we can write

$$\mathbf{P}(S_j)\boldsymbol{Z} \approx \boldsymbol{Z},$$

and obtain from (4.3) that the target location can be estimated along the direction of $\boldsymbol{Z}$, with a resolution of order $c_o H_T/(B|\boldsymbol{Z}|)$. This is the counterpart of result (3.3) in the one receiver case, but the estimate is worse due to the large factor $H_T/|\boldsymbol{Z}|$.

Equation (4.4) involves the linear combination of the relative error of the target velocity along $\boldsymbol{Z}$, and the relative error of the target location along range. If we knew $\boldsymbol{V}_T$, the best orientation of $\boldsymbol{Z}$ would be along the target trajectory, and we would get the range resolution

$$|(\boldsymbol{X}_T(S_j) - \boldsymbol{X}) \cdot \boldsymbol{m}(S_j)| \leq O\left(\frac{\lambda_o H_T^2}{a_T |\boldsymbol{Z}|} \right). \tag{4.5}$$

This is the counterpart of result (3.10) in the one receiver case, but the estimate is worse by the large factor $H_T/|\boldsymbol{Z}|$. Of course, in general $|\boldsymbol{V}_T|$ is not known, and we cannot separate the two errors in (4.4), unless $\boldsymbol{Z}$ is orthogonal to $\boldsymbol{V}_T$. In that case (4.4) gives a relative error of the cross-range velocity in the direction orthogonal to the receiver flight paths.

The large aperture images are obtained as in the one-receiver case by summing coherently the sub-aperture images (4.2). The expression of the imaging function is as in (3.12) and the parametrization is by $\boldsymbol{Y}$ and $\boldsymbol{V}$, the search vectors for the target location $\boldsymbol{Y}_T$ at the reference slow time $s = 0$ and the target velocity $\boldsymbol{V}_T$. Again, the coherent summation gives better results, and in the scaling $A_T \ll H_T$ we can derive analytically the resolution limits. We obtain that $\mathcal{I}(\boldsymbol{Y}, \boldsymbol{V})$ is large when

$$\left| \frac{\mathbf{P}(0)\boldsymbol{Z}}{|\boldsymbol{Z}|} \cdot \frac{(\boldsymbol{Y}_T - \boldsymbol{Y})}{|\boldsymbol{Y}_T|} \right| \leq O\left(\frac{c_o}{B|\boldsymbol{Z}|} \right), \tag{4.6}$$

and

$$\left| \frac{\mathbf{P}(0)\boldsymbol{Z}}{|\boldsymbol{Z}|} \cdot \frac{(\boldsymbol{V}_T - \boldsymbol{V})}{|\boldsymbol{V}_T|} - \frac{Z_{\parallel}}{|\boldsymbol{Z}|} \boldsymbol{m}(0) \cdot \frac{(\boldsymbol{Y}_T - \boldsymbol{Y})}{|\boldsymbol{Y}_T|} \right| \leq O\left(\frac{\lambda_o H_T}{A_T |\boldsymbol{Z}|} \right). \tag{4.7}$$

Here we neglected the residuals, and note the large aperture improvement in (4.7).

4.2. Two pairs of receivers. The results in the previous section show that it is impossible to determine with a single transmitter and a single receiver pair both the location of the target and its velocity. Thus, we consider here an additional pair of receivers and discuss how the added measurements improve the imaging.

We maintain the assumption 4.1 for the first pair of receivers, and suppose that $A_R \ll A_T \ll H_T$, so that we can derive analytically the focusing conditions of the large aperture imaging functions. The second pair of receivers also flies in tandem, at constant velocity $\tilde{\boldsymbol{V}}_R$ and altitude $\tilde{H}_R$ that may be different than $\boldsymbol{V}_R$ and H_R, but satisfy

$$|\tilde{\boldsymbol{V}}_R| = O(|\boldsymbol{V}_R|) \ll |\boldsymbol{V}_T|, \qquad \tilde{H}_R = O(H_R) \ll H_T. \tag{4.8}$$

We denote their locations at slow time s by $\tilde{\boldsymbol{X}}_R(s)$ and $\tilde{\boldsymbol{X}}_R^Z(s)$, and their offset vector by $\tilde{\boldsymbol{Z}}$.

Since there are four receiver platforms, we can form images with cross-correlations of the reflected signals measured by any two of them. For our purpose it suffices to consider three complementary images obtained with the first pair of receivers, the second pair, and across pairs, with the receivers at $\boldsymbol{X}_R$ and $\tilde{\boldsymbol{X}}_R$. We begin as in the previous section with the small aperture images, and then sum them coherently over the large apertures.

The sub-aperture image $\mathcal{I}_j(\boldsymbol{X}, \boldsymbol{V})$ obtained with the first pair of receivers is described in Proposition 4.1. We restate its resolution limits here in simpler form, by neglecting the residuals and using the approximation

$$\boldsymbol{m}(S_j) = \frac{\boldsymbol{X}_T(S_j)}{|\boldsymbol{X}_T(S_j)|} \approx \frac{\boldsymbol{Y}_T}{|\boldsymbol{Y}_T|} = \boldsymbol{m}(0), \qquad \mathbf{P}(S_j) = \mathbf{I} - \boldsymbol{m}(S_j)\boldsymbol{m}(S_j)^T \approx \mathbf{I} - \boldsymbol{m}(0)\boldsymbol{m}(0)^T = \mathbf{P}(0), \tag{4.9}$$

justified by assumption $A_T \ll H_T$. We obtain that $\mathcal{I}_j(\boldsymbol{X}, \boldsymbol{V})$ is large when

$$\left| \frac{\mathbf{P}(0)\boldsymbol{Z}}{|\boldsymbol{Z}|} \cdot \frac{(\boldsymbol{X}_T(S_j) - \boldsymbol{X})}{|\boldsymbol{X}_T(S_j)|} \right| \leq O\left(\frac{c_o}{B|\boldsymbol{Z}|} \right), \tag{4.10}$$

and

$$\left| \frac{\mathbf{P}(0)\boldsymbol{Z}}{|\boldsymbol{Z}|} \cdot \frac{(\boldsymbol{V}_T - \boldsymbol{V})}{|\boldsymbol{V}_T|} - \frac{Z_{\parallel}}{|\boldsymbol{Z}|} \boldsymbol{m}(0) \cdot \frac{(\boldsymbol{X}_T(S_j) - \boldsymbol{X})}{|\boldsymbol{X}_T(S_j)|} \right| \leq O\left(\frac{\lambda_o H_T}{a_T |\boldsymbol{Z}|} \right). \tag{4.11}$$

The resolution of the large aperture image $\mathcal{I}$ is as stated in (4.6) and (4.7).

To explain the improvement brought by the extra measurements we consider two cases: The first is for nearby pairs of receivers, so that

$$|\tilde{\boldsymbol{X}}_R - \boldsymbol{X}_R|, |\tilde{\boldsymbol{X}}_R|, |\tilde{\boldsymbol{Z}}| = O(H_R) \ll H_T, \tag{4.12}$$

and the second is for well separated pairs, so that

$$|\tilde{\boldsymbol{X}}_R - \boldsymbol{X}_R| = O(H_T), \qquad |\tilde{\boldsymbol{Z}}| = O(H_R) \ll H_T. \tag{4.13}$$

4.2.1. Nearby pairs of receivers. When all the receivers are nearby, as described by (4.1) and (4.12), the resolution analysis of the image $\tilde{\mathcal{I}}_j(\boldsymbol{X}, \boldsymbol{V})$ formed with the second pair of receivers is the same as in appendix B. Moreover, the range direction from $\tilde{\boldsymbol{X}}_R(S_j)$ and $\tilde{\boldsymbol{X}}_R^Z(S_j)$ to $\boldsymbol{X}_T(S_j)$ is almost aligned with $\boldsymbol{m}(0)$, so we can state the resolution limits by obvious modifications of equations (4.10) and (4.11). We obtain that $\tilde{\mathcal{I}}_j(\boldsymbol{X}, \boldsymbol{V})$ is large when

$$\left| \frac{\mathbf{P}(0)\tilde{\boldsymbol{Z}}}{|\tilde{\boldsymbol{Z}}|} \cdot \frac{(\boldsymbol{X}_T(S_j) - \boldsymbol{X})}{|\boldsymbol{X}_T(S_j)|} \right| \leq O\left(\frac{c_o}{B|\tilde{\boldsymbol{Z}}|} \right), \tag{4.14}$$

$$\left| \frac{\mathbf{P}(0)\tilde{\boldsymbol{Z}}}{|\tilde{\boldsymbol{Z}}|} \cdot \frac{(\boldsymbol{V}_T - \boldsymbol{V})}{|\boldsymbol{V}_T|} - \frac{\tilde{Z}_{\parallel}}{|\tilde{\boldsymbol{Z}}|} \boldsymbol{m}(0) \cdot \frac{(\boldsymbol{X}_T(S_j) - \boldsymbol{X})}{|\boldsymbol{X}_T(S_j)|} \right| \leq O\left(\frac{\lambda_o H_T}{a_T|\tilde{\boldsymbol{Z}}|} \right), \tag{4.15}$$

where $\tilde{Z}_{\parallel} = \tilde{\boldsymbol{Z}} \cdot \boldsymbol{V}_T/|\boldsymbol{V}_T|$. These results show, as in the previous section, that the best scenario is when $\tilde{\boldsymbol{Z}}$ is almost horizontal. Then, the estimates (4.10) and (4.14) are complementary, as they determine the location of the target along the offset vectors $\boldsymbol{Z}$ and $\tilde{\boldsymbol{Z}}$. If these point in different directions in the horizontal plane, they localize the target in cross-range with resolution of the order $c_o H_T/(BH_R)$, where we used that both $|\boldsymbol{Z}|$ and $|\tilde{\boldsymbol{Z}}|$ are $O(H_R)$.

The estimates (4.11) and (4.15) are also complementary, but they are not sufficient to determine both the target velocity and its range location. Moreover, the sub-aperture image $\breve{\mathcal{I}}_j(\boldsymbol{X}, \boldsymbol{V})$ obtained with the receivers at $\boldsymbol{X}_R$ and $\tilde{\boldsymbol{X}}_R$ does not bring much improvement. The resolution analysis of $\breve{\mathcal{I}}_j(\boldsymbol{X}, \boldsymbol{V})$ is similar but not the same as in appendix B, unless $\boldsymbol{V}_R = \tilde{\boldsymbol{V}}_R$. However, since these velocities are much smaller than $\boldsymbol{V}_T$, the results coincide to leading order. We have that $\breve{\mathcal{I}}_j(\boldsymbol{X}, \boldsymbol{V})$ is large when

$$\left| \frac{\mathbf{P}(0)\breve{\boldsymbol{Z}}(S_j)}{|\breve{\boldsymbol{Z}}(S_j)|} \cdot \frac{(\boldsymbol{X}_T(S_j) - \boldsymbol{X})}{|\boldsymbol{X}_T(S_j)|} \right| \leq O\left(\frac{c_o}{B|\breve{\boldsymbol{Z}}(S_j)|} \right), \tag{4.16}$$

$$\left| \frac{\mathbf{P}(0)\breve{\boldsymbol{Z}}(S_j)}{|\breve{\boldsymbol{Z}}(S_j)|} \cdot \frac{(\boldsymbol{V}_T - \boldsymbol{V})}{|\boldsymbol{V}_T|} - \frac{\breve{Z}_{\parallel}(S_j)}{|\breve{\boldsymbol{Z}}|} \boldsymbol{m}(0) \cdot \frac{(\boldsymbol{X}_T(S_j) - \boldsymbol{X})}{|\boldsymbol{X}_T(S_j)|} \right| \leq O\left(\frac{\lambda_o H_T}{a_T|\breve{\boldsymbol{Z}}(S_j)|} \right), \tag{4.17}$$

where

$$\breve{\boldsymbol{Z}}(S_j) = \tilde{\boldsymbol{X}}_R(S_j) - \boldsymbol{X}_R(S_j), \tag{4.18}$$

and $\breve{Z}_{\parallel} = \breve{\boldsymbol{Z}} \cdot \boldsymbol{V}_T/|\boldsymbol{V}_T|$. The first estimate does not bring any additional information on the target location, as it still involves the projection on the cross-range plane. The second equation does not help either, because it still involves the linear combination of the cross-range velocity error and range target location error.

The analysis of the large aperture image $\tilde{\mathcal{I}}$ obtained by the coherent summation of $\tilde{\mathcal{I}}_j$ is like that of $\mathcal{I}$, and its resolution limits are given by (4.6) and (4.7), with $\boldsymbol{Z}$ replaced by $\tilde{\boldsymbol{Z}}$. The large aperture does not improve the localization of the target in cross-range, which remains of the order $c_o H_T/(BH_R)$, but it sharpens the estimate (4.15), by replacing a_T with A_T.

The analysis of the large aperture $\breve{\mathcal{I}}$ image obtained by the coherent summation of $\breve{\mathcal{I}}_j$ is different when $\boldsymbol{V}_R \neq \tilde{\boldsymbol{V}}_R$, but again in the scaling of this section, and for $A_T \ll H_T$, the results remain similar to leading order.

4.2.2. Well separated pairs of receivers. The setup described by the scaling assumptions (4.1) and (4.13) is better for imaging, due to the large separation between the receivers. We use the same notation as above, with pair separation $\breve{\boldsymbol{Z}}$ defined in (4.18), and state directly the results, without giving the details of the resolution analysis that is very similar to that in appendix B.

The change for the image $\tilde{\mathcal{I}}_j$ comes from the fact that the second pair of receivers views the target from a different direction, which is approximately

$$\tilde{\boldsymbol{m}}(S_j) = \frac{\boldsymbol{X}_T(S_j) - \breve{\boldsymbol{Z}}(S_j)}{|\boldsymbol{X}_T(S_j) - \breve{\boldsymbol{Z}}(S_j)|} \approx \tilde{\boldsymbol{m}}(0) = \frac{\boldsymbol{Y}_T - \breve{\boldsymbol{Z}}(0)}{|\boldsymbol{Y}_T - \breve{\boldsymbol{Z}}(0)|}, \tag{4.19}$$

with $\breve{\boldsymbol{Z}}$ defined in (4.18). The resolution limits are like in (4.14) and (4.15), but with $\boldsymbol{m}$ replaced by $\tilde{\boldsymbol{m}}$ and the projection $\mathbf{P}$ replaced by $\tilde{\mathbf{P}} = \mathbf{I} - \tilde{\boldsymbol{m}}\tilde{\boldsymbol{m}}^T$.

Similarly, the resolution limits of the image $\breve{\mathcal{I}}_j$ are like in (4.16) and (4.17), but with $\boldsymbol{m}$ replaced by $\breve{\boldsymbol{m}} = (\boldsymbol{m} + \tilde{\boldsymbol{m}})/2$, and the projection $\mathbf{P}$ replaced by $\breve{\mathbf{P}} = (\mathbf{P} + \tilde{\mathbf{P}})/2$.

We conclude that the three images give different views of the target, from three linearly independent range directions $\boldsymbol{m}(0)$, $\tilde{\boldsymbol{m}}(0)$ and $\breve{\boldsymbol{m}}(0)$, and therefore in three different cross-range planes. More explicitly, the six resolution equations of the three images give independent error estimates of the six unknowns: the components of the target location and velocity. Thus, we can image the target and estimate its velocity with the two pairs of receivers.

5. Parameter regime and numerical results. In this section we present numerical simulations that verify the resolution results stated in sections 3 and 4. The setup is as illustrated in Figures 1.1 and 1.2, with a point target located at the reference slow time $s = 0$ at $\boldsymbol{Y}_T = (0, 0, H_T)$, with $H_T = 500\,\text{km}$. The target moves with constant speed $\boldsymbol{V}_T = (0, V_T, 0)$, and we consider two values of V_T: either 7610 m/s or 3805 m/s. The target motion defines a synthetic aperture $A_T = V_T T_{\text{tot}}$ over the duration T_{tot} of the data gather. We consider different values of T_{tot}, to illustrate the effect of the aperture on the resolution of the images.

The data for the direct field are generated using a discretization in time of (2.6) while the data for the reflected field are computed by a discretization of (2.7). The probing pulse used in the numerical simulations is

$$f(t) = \cos(2\pi f_o t) \exp\Big(- \frac{B^2 t^2}{2}\Big),$$

with the central frequency $f_o = 9.6\,\text{GHz}$ and the bandwidth $B = 622\,\text{MHz}$. This gives the central wavelength $\lambda_o = 3\,\text{cm}$. The pulse repetition rate is $\Delta s = 0.015\,\text{s}$. The probing pulses are emitted from a transmitter on the ground, at position $\boldsymbol{X}_E = (5, 5, 0)\,\text{m}$.

In the setup with a single receiver platform, this is located at $\boldsymbol{Y}_R = (0, 0, H_R)$ at $s = 0$, with $H_R = 20\,\text{km}$. It moves with the constant velocity $\boldsymbol{V}_R = (V_R, 0, 0)$, which is orthogonal to $\boldsymbol{V}_T$, with $V_R = 222\,\text{m/s}$. Over the duration T_{tot}, the receiver defines the synthetic aperture $A_R = V_R T_{\text{tot}}$.

In the setup with a pair of receivers, they move at the same speed $\boldsymbol{V}_R$ that may be orthogonal or parallel to $\boldsymbol{V}_T$, with $|\boldsymbol{V}_R| = 222\,\text{m/s}$. One receiver is located at $\boldsymbol{Y}_R - \boldsymbol{Z}/2$, with $\boldsymbol{Y}_R$ given above, and the other one at $\boldsymbol{Y}_R + \boldsymbol{Z}/2$. When $\boldsymbol{V}_R = (V_R, 0, 0)$ is orthogonal to $\boldsymbol{V}_T$, the receivers are offset by $\boldsymbol{Z} = (0, Z, 0)$. When $\boldsymbol{V}_R = (0, V_R, 0)$ is along $\boldsymbol{V}_T$, the offset is $\boldsymbol{Z} = (Z, 0, 0)$. In either case we let $Z = 50\,\text{km}$ or $100\,\text{km}$.

The cross-correlations are computed in the time domain by discretizing the expressions of the imaging functionals (3.1) and (4.2) using the Simpson rule. To generate the images we fix four out of the six variables to their correct values and we compute the image as a function of the remaining two variables.

REMARK 1. *The numerical simulations are in the X-band regime. The currently planned Space Surveillance System [15] is in the S-band regime, with central frequency of* 2 GHz*, which gives a* 15 cm *wavelength. The resolution limits in this section can be converted to the S-band system by changing the* 3 cm *wavelength to* 15 cm *and the bandwidth from* 622 MHz *to around* 125 MHz*.*

5.1. Imaging results with one receiver. We illustrate here the resolution results of imaging with the single receiver platform. As explained in section 3, it is impossible to determine all six unknowns (the coordinates of $\boldsymbol{Y}_T$ and components of $\boldsymbol{V}_T$) from the data gathered by the receiver. Thus, we display two-dimensional cross-sections of the images, corresponding to four unknowns fixed at the correct values. To illustrate the effect of the target speed and therefore synthetic aperture A_T on the resolution, we present results for two values of V_T: 7610 m/s and 3805 m/s. We also consider two durations T_{tot} of the experiment: 22.5 s and 10.5 s. These give two different values of the synthetic aperture A_R defined by the receiver motion at speed $V_R = 222\,\text{m/s}$.

Note that at the largest target speed $V_T = 7610\,\text{m/s}$, and the longest duration $T_{\text{tot}} = 22.5\,\text{s}$, the opening angle of the cone defined by the moving target is

$$\arctan\left(\frac{A_T}{2H_T}\right) = 9.2^o.$$

Thus, the range direction perceived from any point along the trajectory remains almost vertical in the simulations. We use the usual coordinate system with the first two coordinates in the horizontal (cross-range) plane, and the third in the vertical direction.

In Figure 5.1 we plot the cross-section of the image $\mathcal{I}(\boldsymbol{Y}, \boldsymbol{V})$ in the plane (V_1, V_2). As expected from the theory, the cross-range velocity V_1 cannot be estimated, while the cross-range velocity V_2 can be estimated with an accuracy of the order of $\lambda_o V_T H_T / A_T^2$, that is, $0.018\,\mathrm{m/s}$ for $T_{\mathrm{tot}} = 10.5\,\mathrm{s}$, $V_T = 7610\,\mathrm{m/s}$ and $0.036\,\mathrm{m/s}$ for $T_{\mathrm{tot}} = 10.5\,\mathrm{s}$, $V_T = 3805\,\mathrm{m/s}$, which is indeed what is observed in the figure.

The estimation of the velocity in the range direction (V_3) can be extracted from Figure 5.2 where we plot the the cross-section of the image $\mathcal{I}(\boldsymbol{Y}, \boldsymbol{V})$ in the plane (V_1, V_3). The numerical results are in agreement with equation (4.7) which shows that the range velocity $V_{T,3}$ can be estimated with an accuracy of the order of $\lambda_o / T_{\mathrm{tot}}$, which equals $2.9\,10^{-3}\,\mathrm{m/s}$ for the shorter duration $T_{\mathrm{tot}} = 10.5\,\mathrm{s}$, and $1.3\,10^{-3}\,\mathrm{m/s}$ for the longer one.

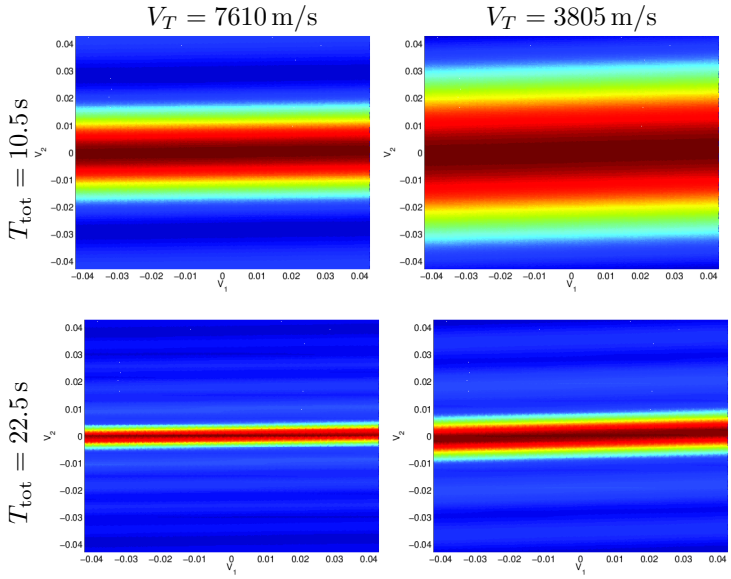

FIGURE 5.1. *One-receiver result: Cross-section of the image $\mathcal{I}(\boldsymbol{Y}, \boldsymbol{V})$ in the plane (V_1, V_2). The origin corresponds to the true values, which are $V_1 = 0$ and $V_2 = V_T$. The abscissa is for V_1 and the ordinate for V_2. The units are in* m/s. *The target velocity is $V_T = 7610\,\mathrm{m/s}$ in the left column, and $3805\,\mathrm{m/s}$ in the right column. The first row is for the duration $T_{\mathrm{tot}} = 10.5\,\mathrm{s}$ and the second for $22.5\,\mathrm{s}$. According to the theory V_1 cannot be accurately estimated, while the cross-range velocity V_2 can be estimated with an accuracy of the order of $\lambda_o V_T H_T / A_T^2$, that is in particular $0.018\,\mathrm{m/s}$ for $T_{\mathrm{tot}} = 10.5\,\mathrm{s}$, $V_T = 7610\,\mathrm{m/s}$, which is supported by the results in the figure.*

Figure 5.3 shows the cross-section of the image $\mathcal{I}(\boldsymbol{Y}, \boldsymbol{V})$ in the plane (Y_1, Y_2). Equations (3.4), (3.8) and (4.7) predict that it is difficult to estimate the location $Y_{T,1}$ of the target. This is confirmed by the figure, where we see no focusing of the image in Y_1, except an oblique line indicating some sensitivity to $Y_{T,1}$. However, we can locate the target along the direction of its trajectory (i.e., $Y_{T,2}$) with a resolution of the order of $\lambda_o H_T / A_T$. This equals $0.09\,\mathrm{m}$ in the case of $V_T = 7610\,\mathrm{m/s}$ and $T_{\mathrm{tot}} = 22.5\,\mathrm{s}$, and corresponds to what we see in the figure, up to some factor of order one.

Figure 5.4 shows the cross-section of the image $\mathcal{I}(\boldsymbol{Y}, \boldsymbol{V})$ in the plane (Y_1, Y_3). Because we fix here $\boldsymbol{V} = \boldsymbol{V}_T$ and $Y_2 = Y_{T,2}$, we can observe the focusing along Y_1. This is the cross-range direction orthogonal to $\boldsymbol{V}_T$, which is along $\boldsymbol{V}_R$ in the simulation. Equation (3.11) predicts that the resolution along Y_1 should be of the order of $\lambda_o H_T / A_R$, which equals $3.2\,\mathrm{m}$ when $T_{\mathrm{tot}} = 22.5\,\mathrm{s}$. This is what the figure gives, up to a factor of order one. The estimate of the target range is expected to be of the order of c_o / B, which equals $0.48\,\mathrm{m}$. It corresponds to the resolution in the figure, up to a factor of order one. Note how the resolution along Y_1 improves when we increase the duration T_{tot}, whereas the resolution along Y_3 stays the same. This is exactly what the theory predicts.

In Figure 5.5 we show the the cross-section of the image $\mathcal{I}(\boldsymbol{Y}, \boldsymbol{V})$ in the plane (Y_2, Y_3). The focusing along Y_3 is the same as in Figure 5.4 and the cross-range focusing as in Figure 5.3. This is the optimal target

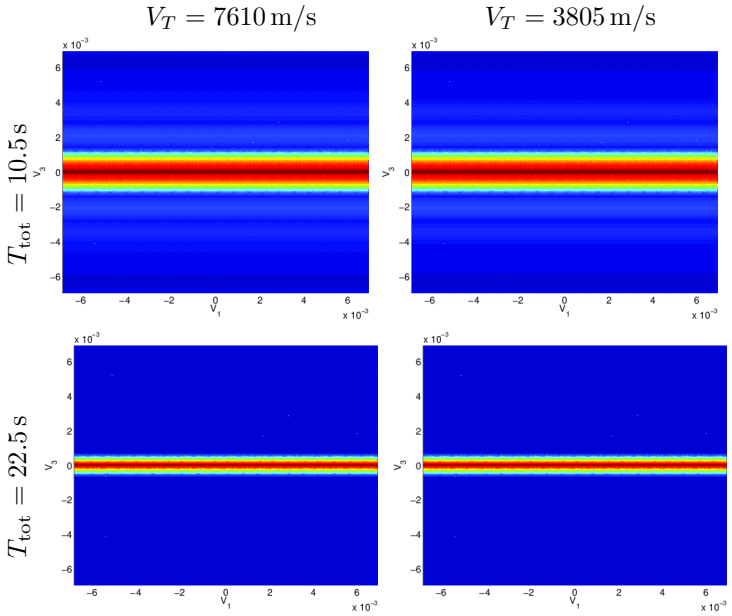

FIGURE 5.2. *One-receiver result: Cross-section of the image $\mathcal{I}(\boldsymbol{Y}, \boldsymbol{V})$ in the plane (V_1, V_3). The origin corresponds to the true values, which are zero. The abscissa is for V_1 and the ordinate for V_3. The units are in* m/s. *The target velocity is $V_T = 7610\,\mathrm{m/s}$ in the left column, and $3805\,\mathrm{m/s}$ in the right column.The first row is for the duration $T_{\mathrm{tot}} = 10.5\,\mathrm{s}$ and the second for $22.5\,\mathrm{s}$. According to the theory V_1 cannot be accurately estimated, while V_3 can be estimated with an accuracy of the order of $\lambda_o/T_{\mathrm{tot}}$, which equals $2.9\,10^{-3}\,\mathrm{m/s}$ for the shorter duration $T_{\mathrm{tot}} = 10.5\,\mathrm{s}$, which conforms well with the results in the figure.*

unknown	estimation	theory
$V_{T,1}$	poorly determined	poorly determined
$V_{T,2}$	$0.013\,\mathrm{m/s}$	$\dfrac{\lambda_o V_T H_T}{A_T^2}$ $(0.01\,\mathrm{m/s})$
$V_{T,3}$	$0.002\,\mathrm{m/s}$	$\dfrac{\lambda_o}{T_{\mathrm{tot}}}$ $(0.002\,\mathrm{m/s})$
$Y_{T,1}$	poorly determined	poorly determined
$Y_{T,2}$	$0.1\,\mathrm{m}$	$\dfrac{\lambda_o H_T}{A_T}$ $(0.13\,\mathrm{m})$
$Y_{T,3}$	$0.4\,\mathrm{m}$	$\dfrac{c_o}{B}$ $(0.48\,\mathrm{m})$

TABLE 5.1

Resolution summary for one-receiver platform when $T_{\mathrm{tot}} = 15\,\mathrm{s}$ and $\boldsymbol{V}_T = (0, V_T, 0)$ with $V_T = 7610\,\mathrm{m/s}$. Recall that $A_T = V_T T_{\mathrm{tot}}$.

localization possible in the one-receiver imaging modality, but it requires knowing the target velocity.

To better assess the resolution we plot in Figure 5.6 the corresponding one-dimensional slices of the two-dimensional plots obtained by fixing one of the two variables to the correct value. The plots are for the target velocity is $\boldsymbol{V}_T = (0, V_T, 0)$ with $V_T = 7610\,\mathrm{m/s}$, and the duration T_{tot} of the experiment is $15\,\mathrm{s}$ and illustrate better the relative magnitude of the side lobes.

We summarize these resolution results in Table 5.1, for the case $V_T = 7610\,\mathrm{m/s}$ and $T_{\mathrm{tot}} = 15\,\mathrm{s}$. In the next section we consider the two-receiver case and we summarize the associated resolution results in the corresponding Table 5.2 below.

REMARK 2. *Given the high number of unknowns in our problem we have chosen to illustrate the imaging results on two-dimensional cross-sections by fixing four out of the six unknowns to their correct values. These images do not allow to fully characterize the imaging function. The theoretical analysis carried out*

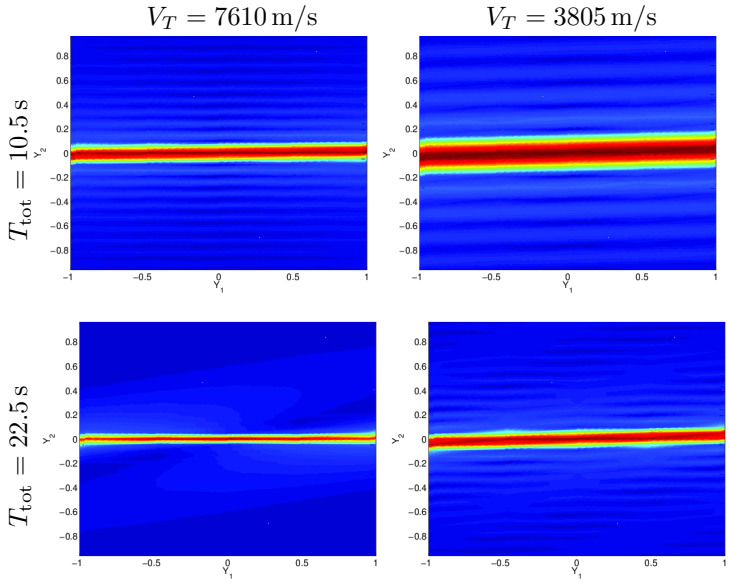

FIGURE 5.3. *One-receiver result: Cross-section of the image $\mathcal{I}(\boldsymbol{Y}, \boldsymbol{V})$ in the plane (Y_1, Y_2). The origin corresponds to the true values, which are zero. The abscissa is for Y_1 and the ordinate for Y_2. The units are in* m. *The target velocity is $V_T = 7610\,\mathrm{m/s}$ in the left column, and $3805\,\mathrm{m/s}$ in the right column. The first row is for the duration $T_{\mathrm{tot}} = 10.5\,\mathrm{s}$ and the second for $22.5\,\mathrm{s}$. According to the theory Y_1 cannot be estimated well, however, we can estimate Y_2 with a resolution of the order of $\lambda_o H_T / A_T$. This equals $0.09\,\mathrm{m}$ in the case of $V_T = 7610\,\mathrm{m/s}$ and $T_{\mathrm{tot}} = 22.5\,\mathrm{s}$, which is roughly what is seen in the figure.*

in Sections 3 and 4 concerns the resolution of the imaging system and assumes that the targets are point like. The analysis is not restricted to the planar two-dimensional cross-sections and fully characterizes the imaging function's resolution. However, the imaging function being rather complicated, it is difficult to obtain a full analytic expression for the point spread function that will shed light on its complete behavior and the existence of possible sidelobes. The numerical simulations are complementary to the theory and give us a better understanding of the point spread function. We see for example in Figure 5.5 that in the plane $Y_2 - Y_3$ there are sidelobes in the Y_3 direction that are stronger than the ones in the Y_2 direction. The joint theoretical and numerical analysis shows the potential, and allows to assess the advantages and the limitations of such passive imaging systems.

5.2. Imaging results with two receivers. We illustrate first the resolution theory of section 4.1 for imaging with a pair of receivers, and then consider two pairs of receivers, to illustrate the image improvement described in section 4.2. The analysis is for nearby receivers in the pair, with offset satisfying $|\boldsymbol{Z}| \ll H_T$. The simulations are in this setting, specially when $|\boldsymbol{Z}| = 50\,\mathrm{km}$, so that $|\boldsymbol{Z}|/H_T = 0.1$. The larger offset $|\boldsymbol{Z}| = 100\,\mathrm{km}$, where $|\boldsymbol{Z}|/H_T = 0.2$, is a borderline case. It allows us to illustrate the effect of increasing the receiver offset.

All the results displayed in this section are for the target velocity $\boldsymbol{V}_T = (0, V_T, 0)$ with $V_T = 7610\,\mathrm{m/s}$. We vary the aperture $A_T = V_T T_{\mathrm{tot}}$ by taking two durations T_{tot}: $10.5\,\mathrm{s}$ and $22.5\,\mathrm{s}$. The receivers fly at speed $\boldsymbol{V}_R$ with magnitude $|\boldsymbol{V}_R| = 222\,\mathrm{m/s}$, which is in the horizontal plane, either parallel to $\boldsymbol{V}_T$ or orthogonal to it. The receiver offset vector $\boldsymbol{Z}$ is also in the horizontal plane and orthogonal to $\boldsymbol{V}_R$.

We begin with Figures 5.7 and 5.8, obtained for $\boldsymbol{V}_R \perp \boldsymbol{V}_T$, and therefore $\boldsymbol{Z}$ parallel to $\boldsymbol{V}_T$. Figure 5.7 displays the cross-section of the image $\mathcal{I}(\boldsymbol{Y}, \boldsymbol{V})$ in the plane (Y_1, Y_3), and Figure 5.8 in the plane (Y_1, Y_2). We expect from equation (4.7) a range resolution of the order of $\lambda_o H_T^2/(A_T Z)$, which equals $1.8\,\mathrm{m}$ in the case $T_{\mathrm{tot}} = 10.5\,\mathrm{s}$ and $Z = 50\,\mathrm{km}$, and $0.9\,\mathrm{m}$ when $T_{\mathrm{tot}} = 10.5\,\mathrm{s}$ and $Z = 100\,\mathrm{km}$. This is consistent with the results in Figure 5.7, where we see improved focusing in range when we increase either T_{tot} and therefore A_T, or Z. The range resolution is about the same for the double offset (middle plot) or the double aperture (right plot), as expected.

Equation (4.6) predicts no resolution along Y_1 and a resolution along Y_2 of the order of $c_o H_T/(BZ)$,

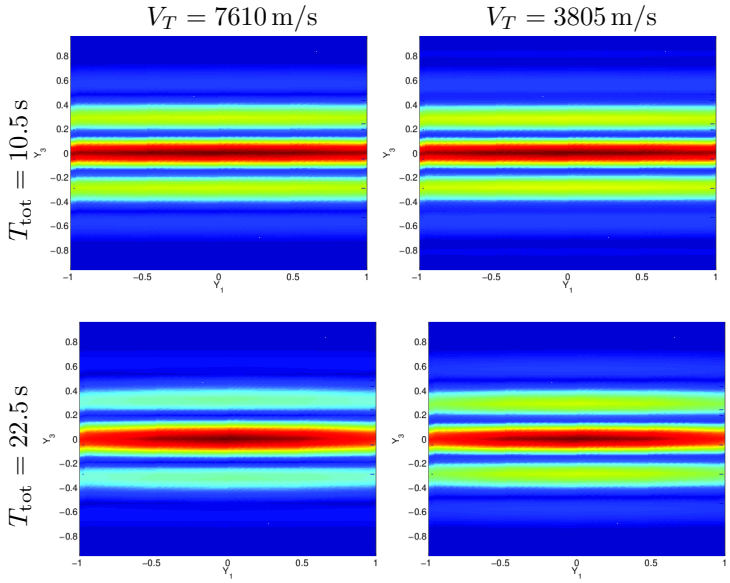

FIGURE 5.4. *One-receiver result: Cross-section of the image $\mathcal{I}(\boldsymbol{Y},\boldsymbol{V})$ in the plane (Y_1, Y_3). The origin corresponds to the true values, which are $Y_1 = 0$ and $Y_3 = 500\,\mathrm{km}$. The abscissa is for Y_1 and the ordinate for Y_3. The units are in* m. *The target velocity is $V_T = 7610\,\mathrm{m/s}$ in the left column, and $3805\,\mathrm{m/s}$ in the right column. The first row is for the duration $T_{\mathrm{tot}} = 10.5\,\mathrm{s}$ and the second for $22.5\,\mathrm{s}$. According to the theory the Y_1 estimate accuracy should be of the order of $\lambda_o H_T/A_R$, which equals $3.2\,\mathrm{m}$ when $T_{\mathrm{tot}} = 22.5\,\mathrm{s}$, while the estimate of the target range Y_3 is expected to be of the order of c_o/B, which equals $0.48\,\mathrm{m}$, which conforms well with the results in the figure.*

while the last term in the left-hand side in (4.4) also gives a resolution in Y_2 which may be better than (4.6). Indeed it gives $|\Delta Y_2| < \lambda_o H_T^3/(A_T^2 Z)$. So that the Y_2 resolution becomes

$$|\Delta Y_2| < \min\left(\lambda_o H_T^3/(A_T^2 Z), c_o H_T/(BZ)\right).$$

For the results shown in Figure 5.8 the minimum is $\lambda_o H_T^3/(A_T^2 Z)$ which equals $2.6\,\mathrm{m}$ for $Z = 50\,\mathrm{km}$ and $1.3\,\mathrm{m}$ for $Z = 100\,\mathrm{km}$. This is consistent with the results in Figure 5.8, where we note the improvement in the focusing along Y_2 for the larger offset Z. Increasing the aperture A_T by considering larger $T_{\mathrm{tot}} = 37.5\,\mathrm{s}$ in Figure 5.9 also improves the resolution along Y_2 as expected from the theory.

We also plot in Figure 5.10 the cross-section of the image $\mathcal{I}(\boldsymbol{Y},\boldsymbol{V})$ in the plane (V_1, V_2). Equation (4.3) suggests that we should not expect any resolution along V_1 while for the velocity component V_2 which is along $\boldsymbol{Z}$ we expect a resolution of the order of $\lambda_o H_T/(T_{\mathrm{tot}} Z)$ and this is indeed what we observe numerically.

unknown	estimation	theory
$V_{T,1}$	not determined	not determined
$V_{T,2}$	$0.01\,\mathrm{m/s}$	$\dfrac{\lambda_o H_T}{T_{\mathrm{tot}} Z}$ $(0.008\,\mathrm{m/s})$
$V_{T,3}$	not determined	not determined
$Y_{T,1}$	not determined	not determined
$Y_{T,2}$	$1.5\,\mathrm{m}$	$\min\left(\dfrac{\lambda_o H_T^3}{A_T^2 Z}, \dfrac{c_o H_T}{BZ}\right)$ $(1.6\,\mathrm{m})$
$Y_{T,3}$	$0.3\,\mathrm{m}$	$\dfrac{\lambda_o H_T^2}{V_T T_{\mathrm{tot}} Z}$ $(0.5\,\mathrm{m})$

TABLE 5.2

Resolution summary for a two-receiver configuration when $T_{\mathrm{tot}} = 20\,\mathrm{s}$, $V_T = 7610\,\mathrm{m/s}$ and $Z = 100\,\mathrm{km}$. The receiver offset $\boldsymbol{Z} = (0, Z, 0)$ is along $\boldsymbol{V}_T = (0, V_T, 0)$ and we consider one receiver at $(0, -Z/2, H_R)$ and the other one at $(0, Z/2, H_R)$. In the Y_2 direction for the parameters used here the minimum is given by $\lambda_o H_T^3/(A_T^2 Z)$.

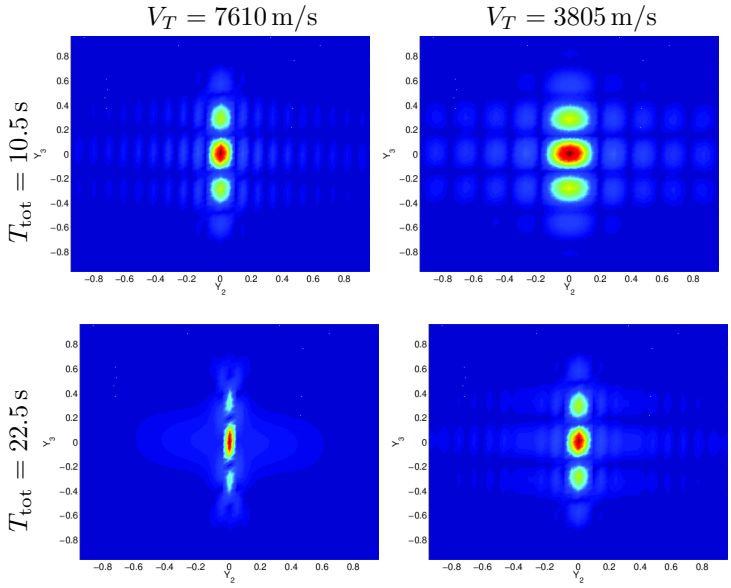

FIGURE 5.5. *One-receiver result: Cross-section of the image $\mathcal{I}(\boldsymbol{Y}, \boldsymbol{V})$ in the plane (Y_2, Y_3). The origin corresponds to the true values, which are $Y_2 = 0$ and $Y_3 = 500\,\mathrm{km}$. The abscissa is for Y_2 and the ordinate for Y_3. The units are in* m. *The target velocity is $V_T = 7610\,\mathrm{m/s}$ in the left column, and $3805\,\mathrm{m/s}$ in the right column. The first row is for the duration $T_{\mathrm{tot}} = 10.5\,\mathrm{s}$ and the second for $22.5\,\mathrm{s}$. The marginal resolutions correspond to those in respectively Figures 5.3 and 5.4.*

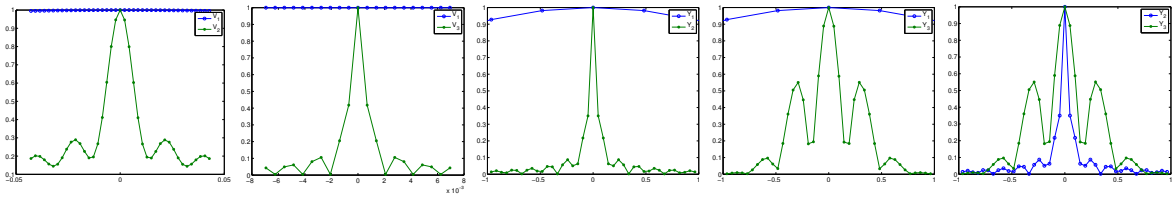

FIGURE 5.6. *The corresponding one-dimensional slices obtained by fixing one of the two variables to the correct value. The plots are normalized by their maximal value. From left to right: (V_1, V_2), (V_1, V_3), (Y_1, Y_2), (Y_1, Y_3), and (Y_2, Y_3). The origin corresponds to the true values. The units in the first two plots are in* m/s *and for the next three plots are in* m. *The target velocity is $\boldsymbol{V}_T = (0, V_T, 0)$ with $V_T = 7610\,\mathrm{m/s}$, and the duration T_{tot} of the experiment is $15\,\mathrm{s}$.*

To obtain focusing along Y_1, the receiver offset should be along this direction, that is orthogonal to $\boldsymbol{V}_T$. This is what equation (4.6) predicts, and is illustrated in Figure 5.11. However, this comes at the expense of the lack of focusing along Y_2. As the theory predicts, it is impossible to locate the target along all three directions, even if we knew its velocity, as assumed in Figure 5.11.

5.3. Two pairs of receivers. In Figures 5.13-5.14 we illustrate the improvement brought by a second pair of receivers. The target velocity is $\boldsymbol{V}_T = (0, V_T, 0)$. The first pair of receivers has an offset $\boldsymbol{Z} = (0, Z, 0)$ and a common velocity $\boldsymbol{V}_R = (V_R, 0, 0)$. The second pair of receivers has an offset $\boldsymbol{Z} = (Z, 0, 0)$ and a common velocity $\boldsymbol{V}_R = (0, V_R, 0)$.

We note the improvement in focusing along the cross-range directions Y_1 and Y_2. Because of the different range directions perceived by the two different receiver pairs, it is now possible to determine all the coordinates of the target. We also illustrate the focusing in the plane (V_1, V_2).

5.4. Image sensitivity with respect to the transmitter location. The results in Section 5.2 were obtained with the exact location $\boldsymbol{X}_E$ of the transmitter. In this section we illustrate the sensitivity of the image to errors in $\boldsymbol{X}_E$. We present in Figure 5.15 cross-sections of the image $\mathcal{I}(\boldsymbol{Y}, \boldsymbol{V})$ obtained with a pair of receivers with offset $\boldsymbol{Z} = (0, Z, 0)$ along $\boldsymbol{V}_T = (0, V_T, 0)$ and $Z = 100\,\mathrm{km}$. We take $V_R = 222\,\mathrm{m/s}$, $V_T = 7610\,\mathrm{m/s}$ and $T_{\mathrm{tot}} = 22.5\,\mathrm{s}$. We consider erroneous transmitter locations shifted by the vector $\Delta X_E(1, 1, 0)$, with ΔX_E as large as $1\,\mathrm{km}$. We note that there is imaging sensitivity to ΔX_E, but this is not as high as in

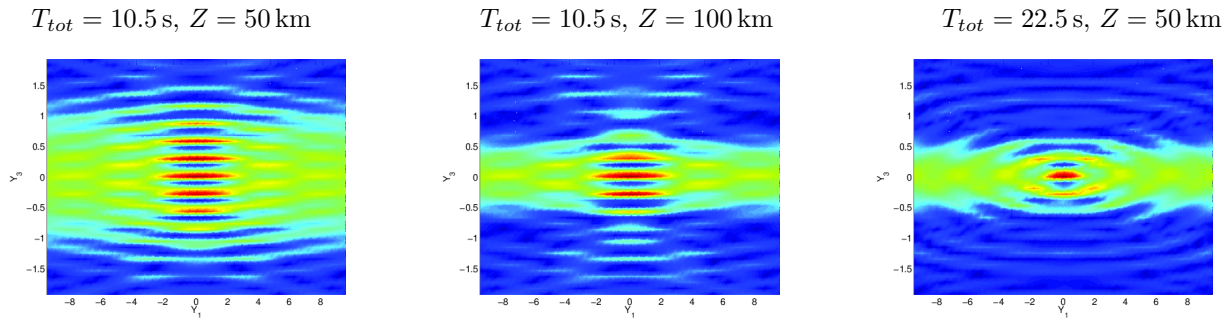

FIGURE 5.7. *One pair of receivers result: Cross-section of the image* $\mathcal{I}(\boldsymbol{Y}, \boldsymbol{V})$ *in the plane* (Y_1, Y_3). *The origin corresponds to the true values, which are* $Y_1 = 0$ *and* $Y_3 = 500\,\mathrm{km}$. *The abscissa is for* Y_1 *and the ordinate for* Y_3. *The units are in* m. *The target velocity is* $\boldsymbol{V}_T = (0, V_T, 0)$ *with* $V_T = 7610\,\mathrm{m/s}$. *The receiver offset* $\boldsymbol{Z} = (0, Z, 0)$ *is along* $\boldsymbol{V}_T$ *and we consider one receiver at* $(0, -Z/2, H_R)$ *and the other one at* $(0, Z/2, H_R)$. *Its magnitude* Z *takes two values:* 50 km *and* 100 km, *as indicated in the plots. The duration* T_{tot} *of the experiment is either* 10.5 s *or* 22.5 s. *The theoretical range* (Y_3) *resolution is* $\lambda_o H_T^2/(A_T Z)$, *which equals* 1.8 m *for the left plot and* 0.9 m *for the middle and right plots.*

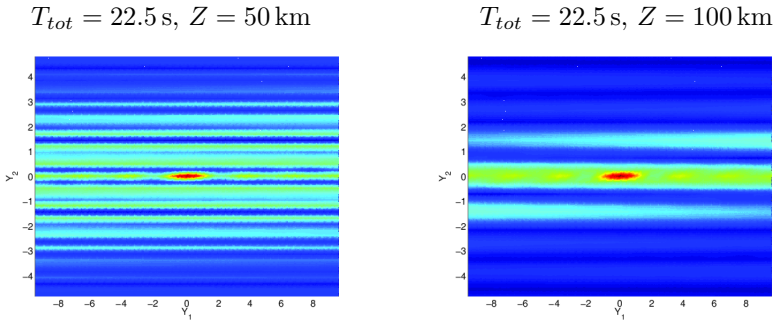

FIGURE 5.8. *One pair of receivers result: Cross-section of the image* $\mathcal{I}(\boldsymbol{Y}, \boldsymbol{V})$ *in the plane* (Y_1, Y_2). *The origin corresponds to the true values, which are zero. The abscissa is for* Y_1 *and the ordinate for* Y_2. *The units are in* m. *The target velocity is* $\boldsymbol{V}_T = (0, V_T, 0)$ *with* $V_T = 7610\,\mathrm{m/s}$. *The receiver offset* $\boldsymbol{Z} = (0, Z, 0)$ *is along* $\boldsymbol{V}_T = (0, V_T, 0)$ *and we consider one receiver at* $(0, -Z/2, H_R)$ *and the other one at* $(0, Z/2, H_R)$. *Its magnitude* Z *takes two values:* 50 km *and* 100 km, *as indicated in the plots. The duration* T_{tot} *of the experiment is* 22.5 s. *The theoretical cross-range resolution along* Y_2 *which is in this case* $\lambda_o H_T^3/(A_T^2 Z)$ *gives* 2.6 m *for* $Z = 50\,\mathrm{km}$ *and* 1.3 m *for* $Z = 100\,\mathrm{km}$.

the one-receiver case (not shown here). The images deteriorate when we increase ΔX_E, but they still look reasonable when $\Delta X_E = 500\,\mathrm{m}$, which is more than 10^4 wavelengths.

6. Summary and conclusions. We have considered the imaging of fast moving objects with passive correlation based techniques using surface/airborne bistatic radar systems. A single transmitter on the ground illuminates a sector of the sky and one or more flying receiver platforms record the signals reflected by a fast moving target. In the one-receiver case we cross-correlate the signal arriving directly from the transmitter with the reflected signal by adequately selecting the evaluation times in our imaging function and compensating for Doppler effects. In this case we need to know the arrival time from the transmitter to the antenna and from the transmitter to the search point in the image, so accurate knowledge of the transmitter location is needed. In the multiple-receiver case we cross-correlate the reflected signals recorded at two of the receivers. A surprising result is that here too we need to know the transmitter location, but with relatively low accuracy. This is unusual for correlation-based imaging and is due to the Doppler corrections that we need to take into account because of the high velocity of the moving object.

A simplified version of the main results of the paper can be given when we assume that the trajectories of the target and the antenna are linear and parallel to the ground. We then have the following resolution formulas for this one-receiver configuration:

(i) Resolution in range is proportional to c_o/B and is determined by the bandwidth.

(ii) In the direction that the target is moving, resolution is proportional to $\lambda_o H_T/A_T$, A_T being the

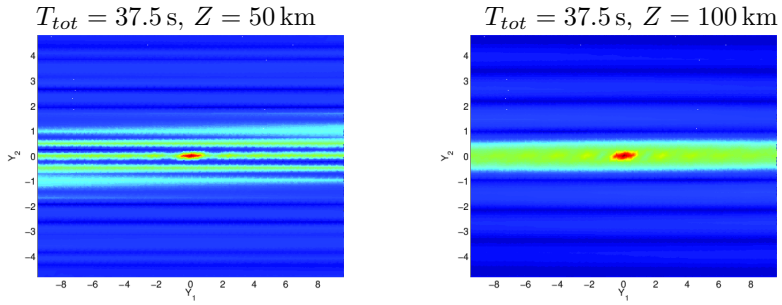

FIGURE 5.9. *One pair of receivers result: Cross-section of the image* $\mathcal{I}(\boldsymbol{Y}, \boldsymbol{V})$ *in the plane* (Y_1, Y_2). *The origin corresponds to the true values, which are zero. The abscissa is for* Y_1 *and the ordinate for* Y_2. *The units are in* m. *The target velocity is* $\boldsymbol{V}_T = (0, V_T, 0)$ *with* $V_T = 7610\,\mathrm{m/s}$. *The receiver offset* $\boldsymbol{Z} = (0, Z, 0)$ *is along* $\boldsymbol{V}_T = (0, V_T, 0)$ *and we consider one receiver at* $(0, -Z/2, H_R)$ *and the other one at* $(0, Z/2, H_R)$. *Its magnitude* Z *takes two values:* 50 km *and* 100 km, *as indicated in the plots. The duration* T_{tot} *of the experiment is* 37.5 s. *The theoretical cross-range resolution along* Y_2 *which is* $\lambda_o H_T^3/(A_T^2 Z)$ *gives* 0.92 m *for* $Z = 50\,\mathrm{km}$ *and* 0.46 m *for* $Z = 100\,\mathrm{km}$.

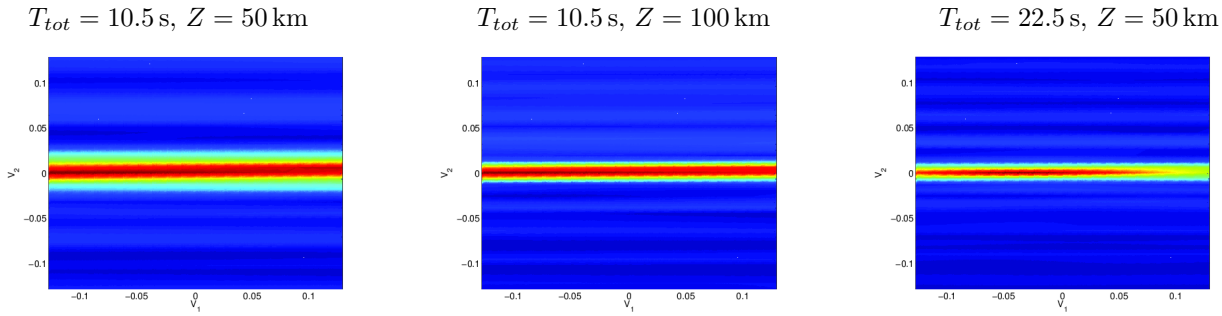

FIGURE 5.10. *One pair of receivers result: Cross-section of the image* $\mathcal{I}(\boldsymbol{Y}, \boldsymbol{V})$ *in the plane* (V_1, V_2). *The origin corresponds to the true values. The abscissa is for* V_1 *and the ordinate for* V_2. *The units are in* m/s. *The target velocity is* $\boldsymbol{V}_T = (0, V_T, 0)$ *with* $V_T = 7610\,\mathrm{m/s}$. *The receiver offset* $\boldsymbol{Z} = (0, Z, 0)$ *is along* $\boldsymbol{V}_T$ *and we consider one receiver at* $(0, -Z/2, H_R)$ *and the other one at* $(0, Z/2, H_R)$. *Its magnitude* Z *takes two values:* 50 km *and* 100 km, *as indicated in the plots. The duration* T_{tot} *of the experiment is either* 10.5 s *or* 22.5 s. *The theoretical resolution along* V_2 *is* $\lambda_o H_T/(T_{\mathrm{tot}} Z)$ *which gives* 0.03 m/s *for* $Z = 50\,\mathrm{km}$ *and* $T_{\mathrm{tot}} = 10.5\,\mathrm{s}$, 0.014 m/s *for* $Z = 100\,\mathrm{km}$ *and* $T_{\mathrm{tot}} = 10.5\,\mathrm{s}$, *and* 0.013 m/s *for* $Z = 50\,\mathrm{km}$ *and* $T_{\mathrm{tot}} = 22.5\,\mathrm{s}$.

aperture covered by the fast moving target.

For the multiple receiver case, two pairs of receivers are needed for recovering all the unknowns. Assuming in particular as before that the trajectories are linear parallel to the ground and that one receiver pair is moving orthogonal to the target and the other parallel to it, we obtain the following:

(i) Resolution in range is proportional to $\lambda_0 H_T^2/(ZA_T)$, Z being the distance between the receiver antennas that is assumed constant.

(ii) In the cross-range direction that the target is moving, resolution is proportional to $\min\left(c_o H_T/(BZ), \lambda_0 H_T^3/(ZA_T^2)\right)$.

(iii) In the second cross-range direction resolution is proportional to $c_o H_T/(BZ)$.

An issue in the one-receiver case is that the position and velocity of the target cannot be uniquely determined. Unique recovery can be achieved, however, by using two-pairs of receivers. Increasing the distance between the two receiver platforms is beneficial for the image quality and we observe an improvement in resolution. But as the distance between the receivers increases we find that sensitivity to knowing the transmitter location increases.

In this paper we have focused our attention on resolution. We comment here briefly on the role of noise. We anticipate that the correlation-based imaging methods that we propose are very robust with respect to additive measurement noise, because we cross correlate signals recorded at different time windows in the one-receiver case and we cross correlate signals recorded by different receivers in the two-receiver case. We also anticipate that the proposed methods are robust with respect to medium noise induced by the turbulent

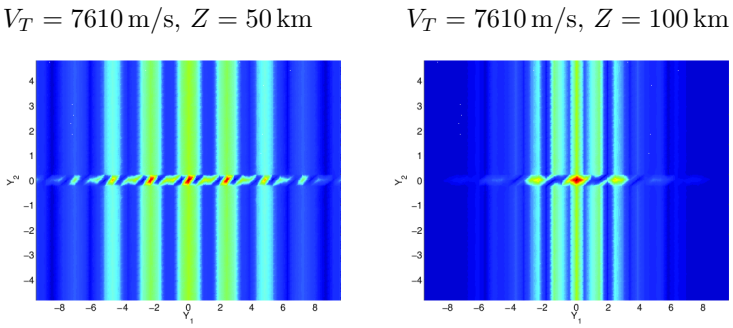

FIGURE 5.11. *One pair of receivers result: Cross-section of the image $\mathcal{I}(\boldsymbol{Y},\boldsymbol{V})$ in the plane (Y_1, Y_2). The origin corresponds to the true values, which are zero. The abscissa is for Y_1 and the ordinate for Y_2. The units are in m. The target velocity is $\boldsymbol{V}_T = (0, V_T, 0)$ with $V_T = 7610\,\mathrm{m/s}$ or $V_T = 3805\,\mathrm{m/s}$, as indicated on the plots. The receiver offset $\boldsymbol{Z} = (Z, 0, 0)$ is orthogonal to $\boldsymbol{V}_T$ and we consider one receiver at $(-Z/2, 0, H_R)$ and the other one at $(Z/2, 0, H_R)$. The magnitude of the offset Z takes two values: 50 km and 100 km, as indicated in the plots. The duration T_{tot} of the experiment is 22.5 s. The theoretical resolution along Y_1 is $c_o H_T/(BZ)$ which gives 4.8 m for $Z = 50\,\mathrm{km}$ and 2.4 m for $Z = 100\,\mathrm{km}$.*

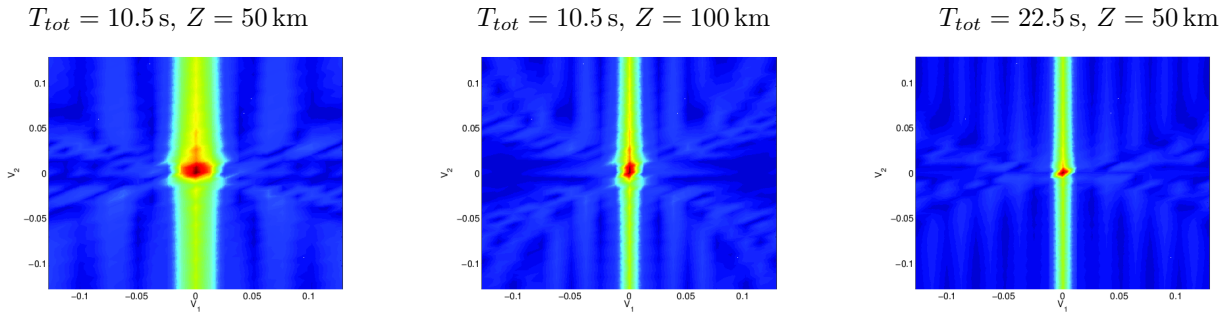

FIGURE 5.12. *One pair of receivers result: Cross-section of the image $\mathcal{I}(\boldsymbol{Y},\boldsymbol{V})$ in the plane (V_1, V_2). The origin corresponds to the true values. The abscissa is for V_1 and the ordinate for V_2. The units are in m/s. The target velocity is $\boldsymbol{V}_T = (0, V_T, 0)$ with $V_T = 7610\,\mathrm{m/s}$. The receiver offset $\boldsymbol{Z} = (Z, 0, 0)$ is orthogonal to $\boldsymbol{V}_T$. The magnitude of the offset Z takes two values: 50 km and 100 km, as indicated in the plots. The duration T_{tot} of the experiment is either 10.5 s or 22.5 s. The theoretical resolution along V_1 is $\lambda_o H_T/(T_{\mathrm{tot}} Z)$ which gives 0.029 m/s for the left plot and 0.014 m/s for the middle and right plots.*

atmosphere. This was shown in passive imaging with stationary arrays in [11, 13, 14].

Acknowledgements. The work of L. Borcea was partially supported by the NSF grant DMS1510429. Support from AFOSR is also gratefully acknowledged. The work of G. Papanicolaou and C. Tsogka was partially supported by AFOSR grant FA9550-11-1-0266. The work of K. Sølna was partially supported by AFOSR grant FA9550-14-1-0197.

Appendix A. Resolution analysis with one receiver. In this appendix we derive the resolution results stated in section 3, in our regime of separation of scales with large target height $H_T \gg H_R$, large target velocity $|\boldsymbol{V}_T| \gg |\boldsymbol{V}_R|$, and large central frequency $\omega_o \gg B$. We define this regime using a dimensionless asymptotic parameter $\varepsilon \ll 1$ in section A.1. The data model in this scaling is given in section A.2, and the resolution limits are derived in sections A.3 and A.4.

A.1. Scaling. To model the separation of scales, we introduce the asymptotic scaling parameter $\varepsilon \ll 1$, defined as the ratio of the altitude of the receiver and the altitude of the target. We denote henceforth by superscript ε the real quantities, and use the scaling by ε to define their scaled, order one counterparts. Thus, the initial locations of the receiver and target (at slow time 0) are $\boldsymbol{Y}_T^\varepsilon$ and $\boldsymbol{Y}_R^\varepsilon$, and the velocities of the receiver and target are $\boldsymbol{V}_T^\varepsilon$ and $\boldsymbol{V}_R^\varepsilon$. In the numerical setting discussed in Section 5, $\omega_o^\varepsilon = 2\pi\, 9.6\,\mathrm{GHz}$, $B^\varepsilon = 622\,\mathrm{MHz}$, $|\boldsymbol{V}_R^\varepsilon| = 222\,\mathrm{m/s}$, $|\boldsymbol{V}_T^\varepsilon| = 7610\,\mathrm{m/s}$, $H_R^\varepsilon = Y_{R,3}^\varepsilon = 2\,10^4\,\mathrm{m}$, $H_T^\varepsilon = Y_{T,3}^\varepsilon = 5\,10^5\,\mathrm{m}$, $T_{\mathrm{tot}}^\varepsilon = 22\,\mathrm{s}$,

unknown	estimation	theory
$V_{T,1}$	$0.01\,\mathrm{m/s}$	$\dfrac{\lambda_o H_T}{T_{\mathrm{tot}} Z}$ $(0.008\,\mathrm{m/s})$
$V_{T,2}$	not determined	not determined
$V_{T,3}$	not determined	not determined
$Y_{T,1}$	$2.4\,\mathrm{m}$	$\dfrac{c_o H_T}{BZ}$ $(2.4\,\mathrm{m})$
$Y_{T,2}$	not determined	not determined
$Y_{T,3}$	not determined	not determined

TABLE 5.3

Resolution summary for a two-receiver configuration when $T_{\mathrm{tot}} = 20\,\mathrm{s}$, $V_T = 7610\,\mathrm{m/s}$, $Z = 100\,\mathrm{km}$, *and* $\boldsymbol{Z} = (Z, 0, 0)$ *is orthogonal to* $\boldsymbol{V}_T = (0, V_T, 0)$.

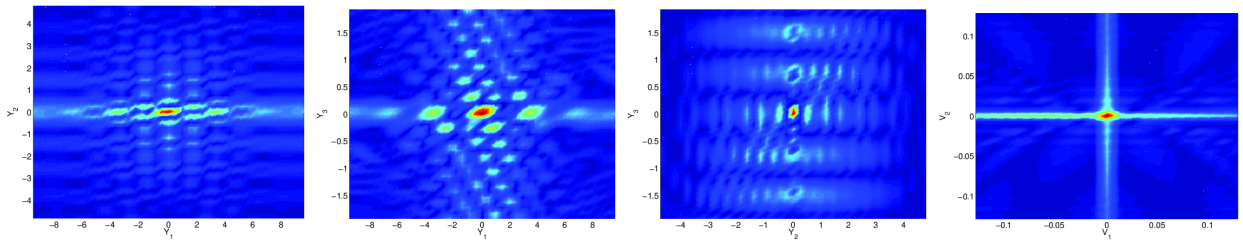

FIGURE 5.13. *Two pairs of receivers result given by summing the images obtained with each pair. We show results for* $Z = 100\,\mathrm{km}$. *From left to right: Cross-section of the image* $\mathcal{I}(\boldsymbol{Y}, \boldsymbol{V})$ *in the planes* (Y_1, Y_2), (Y_1, Y_3), (Y_2, Y_3) *and* (V_1, V_2). *The origin corresponds to the true values. The units in the first three plots are in m and in the last plot in m/s. The target velocity is* $\boldsymbol{V}_T = (0, V_T, 0)$ *with* $V_T = 7610\,\mathrm{m/s}$, *and the duration* T_{tot} *of the experiment is* $22.5\,\mathrm{s}$. *The common speed for the receivers is* $V_R = 222\,\mathrm{m/s}$.

$\Delta s^\varepsilon = 1.5\,10^{-2}$ seconds, so

$$\varepsilon = \frac{Y^\varepsilon_{R,3}}{Y^\varepsilon_{T,3}} = \frac{H^\varepsilon_R}{H^\varepsilon_T} = 0.04.$$

The system of coordinates is defined by the unit basis vectors $(\hat{\boldsymbol{e}}_1, \hat{\boldsymbol{e}}_2, \hat{\boldsymbol{e}}_3)$, where $\hat{\boldsymbol{e}}_3$ is in the upward vertical direction.

The reference (order one) length scale is given by the altitude H^ε_T of the target (i.e., $5\,10^5\,\mathrm{m}$). The reference time is the travel time for a round trip from the ground to the target (i.e., $3.3\,10^{-3}\,\mathrm{s}$) and the

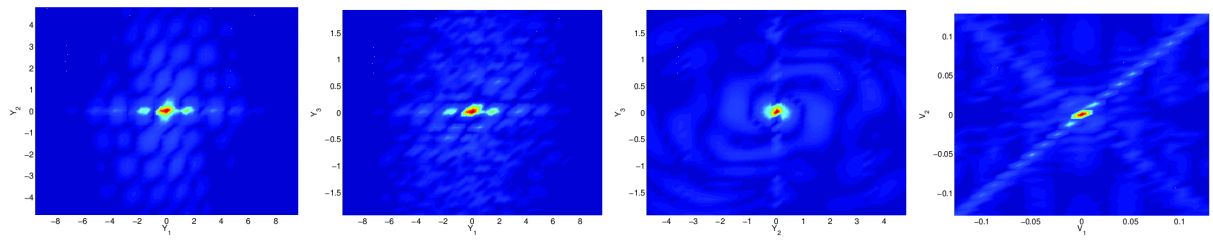

FIGURE 5.14. *Two pairs of receivers result given by multiplying the images obtained with each pair. We show results for* $Z = 100\,\mathrm{km}$. *From left to right: Cross-section of the image* $\mathcal{I}(\boldsymbol{Y}, \boldsymbol{V})$ *in the planes* (Y_1, Y_2), (Y_1, Y_3), (Y_2, Y_3) *and* (V_1, V_2). *The origin corresponds to the true values. The units in the first three plots are in m and in the last plot in m/s. The target velocity is* $\boldsymbol{V}_T = (0, V_T, 0)$ *with* $V_T = 7610\,\mathrm{m/s}$, *and the duration* T_{tot} *of the experiment is* $22.5\,\mathrm{s}$. *The common speed for the receivers is* $V_R = 222\,\mathrm{m/s}$.

unknown	estimation	theory
$V_{T,1}$	$0.01\,\mathrm{m/s}$	$\dfrac{\lambda_o H_T}{T_{\mathrm{tot}} Z}$ $(0.008\,\mathrm{m/s})$
$V_{T,2}$	$0.01\,\mathrm{m/s}$	$\dfrac{\lambda_o H_T}{T_{\mathrm{tot}} Z}$ $(0.008\,\mathrm{m/s})$
$V_{T,3}$	not determined	not determined
$Y_{T,1}$	$2.4\,\mathrm{m}$	$\dfrac{c_o H_T}{BZ}(2.4\,\mathrm{m})$
$Y_{T,2}$	$1.5\,\mathrm{m}$	$\min\left(\dfrac{\lambda_o H_T^3}{A_T^2 Z}, \dfrac{c_o H_T}{BZ}\right)$ $(1.6\,\mathrm{m})$
$Y_{T,3}$	$0.3\,\mathrm{m}$	$\dfrac{\lambda_o H_T^2}{A_T Z}$ $(0.5\,\mathrm{m})$

TABLE 5.4

Resolution summary for two pairs of receiver platforms, with $T_{\mathrm{tot}} = 20\,\mathrm{s}$, $Z = 100\,\mathrm{km}$. *In the* Y_2 *direction for the parameters used here the minimum is given by* $\lambda_o H_T^3/(A_T^2 Z)$.

reference speed is c_o (i.e., $3\,10^8\,\mathrm{m/s}$). According to the listed numerical values, we scale the variables by

$$
\begin{aligned}
\omega_o^\varepsilon &= \frac{\omega_o}{\varepsilon^5},\\
B^\varepsilon &= \frac{B}{\varepsilon^4},\\
T_{\mathrm{tot}}^\varepsilon &= \frac{T_{\mathrm{tot}}}{\varepsilon^3},\\
\Delta S^\varepsilon &= \frac{\Delta S}{\varepsilon},\\
\Delta s^\varepsilon &= \Delta s,\\
\boldsymbol{V}_T^\varepsilon &= \varepsilon^3 \boldsymbol{V}_T = \varepsilon^3 (V_{T,1}, V_{T,2}, V_{T,3}),\\
\boldsymbol{V}_R^\varepsilon &= \varepsilon^4 \boldsymbol{V}_R = \varepsilon^4 (V_{R,1}, V_{R,2}, V_{R,3}),\\
\boldsymbol{Y}_T^\varepsilon &= \boldsymbol{Y}_T = (Y_{T,1}, Y_{T,2}, Y_{T,3}),\\
\boldsymbol{Y}_R^\varepsilon &= \varepsilon \boldsymbol{Y}_R = \varepsilon (Y_{R,1}, Y_{R,2}, Y_{R,3}),\\
\boldsymbol{Z}^\varepsilon &= \varepsilon \boldsymbol{Z} = \varepsilon (Z_1, Z_2, Z_3),\\
\boldsymbol{X}_E^\varepsilon &= \varepsilon \boldsymbol{X}_E = \varepsilon (X_{E,1}, X_{E,2}, 0),
\end{aligned}
$$

where all quantities without superscript ε are order one. We also consider the scaling of the slow time (over

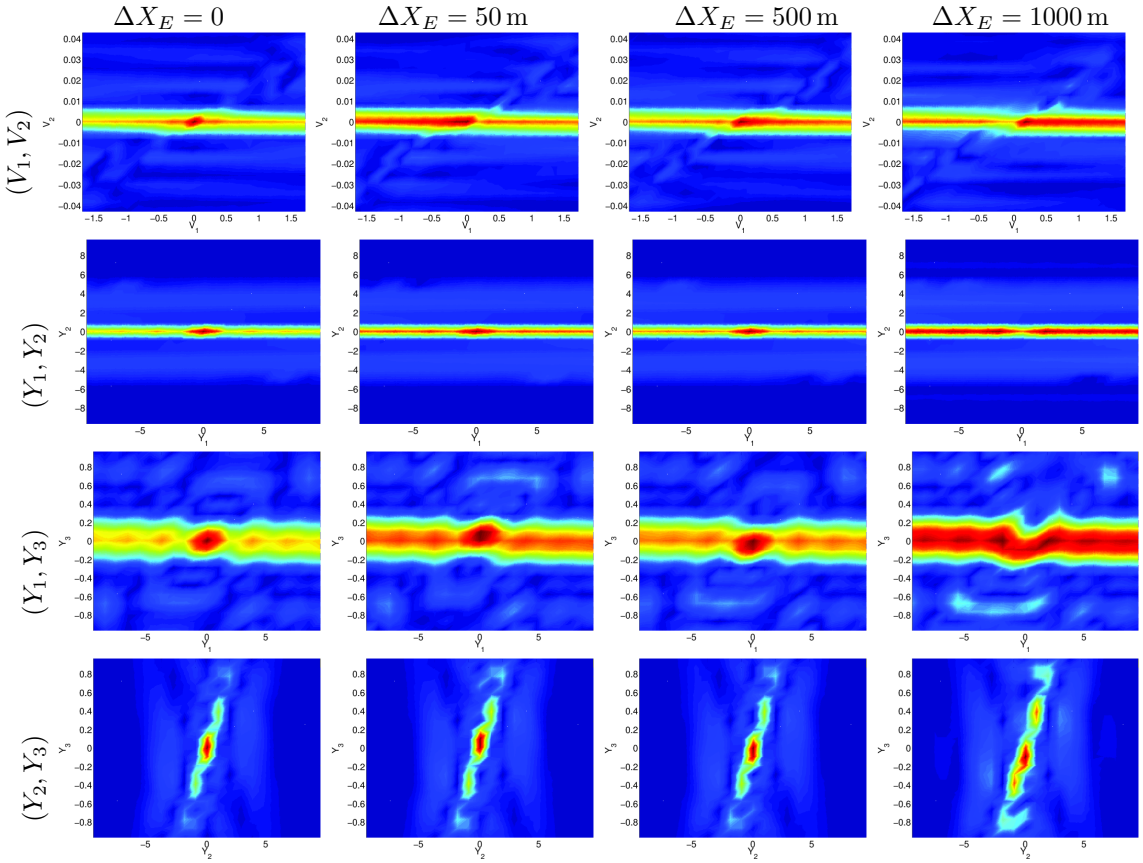

FIGURE 5.15. *One pair of receivers result: Sensitivity of the image to errors in the transmitter location. The transmitter is erroneously placed at* $\boldsymbol{X}_E + \Delta X_E(1,1,0)$*, with* ΔX_E *shown in the plots. The images in the first row are shown in the plane* (V_1, V_2)*, with* V_1 *in the abscissa and* V_2 *in the ordinate. The units are in m/s. The other rows show images in the planes* (Y_1, Y_2)*,* (Y_1, Y_3)*, and* (Y_2, Y_3)*, and the axes are in units of m.*

the recording time window $(-T^\varepsilon_{\rm tot}/2, T^\varepsilon_{\rm tot}/2)$ as

$$s^\varepsilon = \frac{s}{\varepsilon^3},$$

which is consistent with that of length. For example, the receiver position at slow time $s^\varepsilon = s/\varepsilon^3$ is $\boldsymbol{X}^\varepsilon_R(s^\varepsilon) = \boldsymbol{Y}^\varepsilon_R + s^\varepsilon \boldsymbol{V}^\varepsilon_R$, which is equal to $\varepsilon \boldsymbol{X}_R(s)$ with $\boldsymbol{X}_R(s) = \boldsymbol{Y}_R + s\boldsymbol{V}_R$. Similarly the target position is $\boldsymbol{X}^\varepsilon_T(s^\varepsilon) = \boldsymbol{Y}^\varepsilon_T + s^\varepsilon \boldsymbol{V}^\varepsilon_T$, which is equal to $\boldsymbol{X}_T(s)$ with $\boldsymbol{X}_T(s) = \boldsymbol{Y}_T + s\boldsymbol{V}_T$.

The sub-apertures are defined by the slow time intervals $\Delta S^\varepsilon = \Delta S/\varepsilon$, and there are many of them, $N^\varepsilon = \lfloor T^\varepsilon_{\rm tot}/\Delta S^\varepsilon \rfloor - 1 = O(\varepsilon^{-2})$. Moreover, in each sub-aperture the transmitter emits a large number of pulses $n^\varepsilon = \lfloor \Delta S^\varepsilon/\Delta s^\varepsilon \rfloor = O(\varepsilon^{-1})$ at slow time instances

$$s^\varepsilon_{jl} = S^\varepsilon_j + l\Delta s^\varepsilon = \frac{S_j}{\varepsilon^3} + l\Delta s, \quad |l| \le n^\varepsilon/2.$$

Given the velocity scalings this gives the sub-apertures

$$a^\varepsilon_T = |\boldsymbol{V}^\varepsilon_T|\Delta S^\varepsilon = \varepsilon^2 |\boldsymbol{V}_T|\Delta S = \varepsilon^2 a_T \quad \text{and} \quad a^\varepsilon_R = |\boldsymbol{V}^\varepsilon_R|\Delta S^\varepsilon = \varepsilon^3 a_R,$$

whereas the large apertures are

$$A^\varepsilon_T = |\boldsymbol{V}^\varepsilon_T|T^\varepsilon_{\rm tot} = |\boldsymbol{V}_T|T_{\rm tot} = A_T \quad \text{and} \quad A^\varepsilon_R = |\boldsymbol{V}^\varepsilon_R|T^\varepsilon_{\rm tot} = \varepsilon|\boldsymbol{V}_R|T_{\rm tot} = \varepsilon A_R.$$

The transmitter is on the ground $X_{E,3} = 0$, and in the same region as the receiver antenna.

A.2. Data model. The transmitter emits around time s^ε the signal

$$f^\varepsilon(t-s^\varepsilon) = 2F\big(\varepsilon^{-4}Bt\big)\cos\big(\varepsilon^{-5}\omega_o t\big). \tag{A.1}$$

The recorded data consists of two contributions: the direct wave $u_{\rm d}^\varepsilon$ and the reflected (scattered) wave $u_{\rm r}^\varepsilon$:

$$u_{\rm d}^\varepsilon(s^\varepsilon+t) = \frac{1}{4\pi|\boldsymbol{X}_R^\varepsilon(s^\varepsilon+t)-\boldsymbol{X}_E^\varepsilon|} f^\varepsilon\Big(t-\frac{|\boldsymbol{X}_R^\varepsilon(s^\varepsilon+t)-\boldsymbol{X}_E^\varepsilon|}{c_o}\Big)$$

and

$$\begin{aligned} u_{\rm r}^\varepsilon(s^\varepsilon+t) = -\int_0^t dt' \frac{\rho^\varepsilon}{(4\pi)^2 c_o^2|\boldsymbol{X}_R^\varepsilon(s^\varepsilon+t)-\boldsymbol{X}_T^\varepsilon(s^\varepsilon+t')|} \\ \times\frac{1}{|\boldsymbol{X}_T^\varepsilon(s^\varepsilon+t')-\boldsymbol{X}_E^\varepsilon|} f^{\varepsilon\prime\prime}\Big(t'-\frac{|\boldsymbol{X}_T^\varepsilon(s^\varepsilon+t')-\boldsymbol{X}_E^\varepsilon|}{c_o}\Big) \\ \times\delta\Big(t-t'-\frac{|\boldsymbol{X}_T^\varepsilon(s^\varepsilon+t')-\boldsymbol{X}_R^\varepsilon(s^\varepsilon+t)|}{c_o}\Big). \end{aligned}$$

Here ρ^ε is the scattering coefficient of the target. We expand the distances in powers of ε and since the carrier frequency is ε^{-5}, we keep the terms up to $o(\varepsilon^5)$,

$$\begin{aligned} |\boldsymbol{X}_R^\varepsilon(s^\varepsilon+t)-\boldsymbol{X}_E^\varepsilon| &= \varepsilon|\boldsymbol{X}_R(s)-\boldsymbol{X}_E| + \varepsilon^4 t\boldsymbol{V}_R\cdot\frac{\boldsymbol{X}_R(s)-\boldsymbol{X}_E}{|\boldsymbol{X}_R(s)-\boldsymbol{X}_E|}+o(\varepsilon^5), \\ |\boldsymbol{X}_T^\varepsilon(s^\varepsilon+t')-\boldsymbol{X}_E^\varepsilon| &= |\boldsymbol{X}_T(s)-\varepsilon\boldsymbol{X}_E| + \varepsilon^3 t'\boldsymbol{V}_T\cdot\frac{\boldsymbol{X}_T(s)-\varepsilon\boldsymbol{X}_E}{|\boldsymbol{X}_T(s)-\varepsilon\boldsymbol{X}_E|}+o(\varepsilon^5), \\ |\boldsymbol{X}_T^\varepsilon(s^\varepsilon+t')-\boldsymbol{X}_R^\varepsilon(s^\varepsilon+t)| &= |\boldsymbol{X}_T(s)-\varepsilon\boldsymbol{X}_R(s)| + \big(\varepsilon^3 t'\boldsymbol{V}_T-\varepsilon^4 t\boldsymbol{V}_R\big)\cdot\frac{\boldsymbol{X}_T(s)-\varepsilon\boldsymbol{X}_R(s)}{|\boldsymbol{X}_T(s)-\varepsilon\boldsymbol{X}_R(s)|}+o(\varepsilon^5). \end{aligned}$$

The model of the direct signal is

$$u_{\rm d}^\varepsilon(s^\varepsilon+t) \approx \frac{f^\varepsilon\big(\gamma_{\rm d}^\varepsilon(s^\varepsilon)t-t_{\rm d}^\varepsilon(s^\varepsilon)\big)}{4\pi|\boldsymbol{X}_R^\varepsilon(s^\varepsilon)-\boldsymbol{X}_E^\varepsilon|} = \frac{f^\varepsilon\big(\gamma_{\rm d}(s)t-t_{\rm d}(s)\big)}{4\pi\varepsilon|\boldsymbol{X}_R(s)-\boldsymbol{X}_E|}, \tag{A.2}$$

where

$$\gamma_{\rm d}^\varepsilon(s^\varepsilon) := 1-\frac{\boldsymbol{V}_R^\varepsilon}{c_o}\cdot\frac{(\boldsymbol{X}_R^\varepsilon(s^\varepsilon)-\boldsymbol{X}_E^\varepsilon)}{|\boldsymbol{X}_R^\varepsilon(s^\varepsilon)-\boldsymbol{X}_E^\varepsilon|} = \gamma_{\rm d}(s) := 1-\varepsilon^4\frac{\boldsymbol{V}_R}{c_o}\cdot\frac{(\boldsymbol{X}_R(s)-\boldsymbol{X}_E)}{|\boldsymbol{X}_R(s)-\boldsymbol{X}_E|}, \tag{A.3}$$

and

$$t_{\rm d}^\varepsilon(s) := \frac{|\boldsymbol{X}_R^\varepsilon(s^\varepsilon)-\boldsymbol{X}_E^\varepsilon|}{c_o} = t_{\rm d}(s) := \varepsilon\frac{|\boldsymbol{X}_R(s)-\boldsymbol{X}_E|}{c_o}. \tag{A.4}$$

As stated before, the quantities with the superscript ε are in physical units and those without the epsilon superscript are in the scaled units.

The reflected signal is

$$\begin{aligned} u_{\rm r}^\varepsilon(s^\varepsilon+t) &\approx \frac{\rho^\varepsilon(k_o^\varepsilon)^2}{(4\pi)^2|\boldsymbol{X}_T^\varepsilon(s^\varepsilon)|^2} f^\varepsilon\Big(\gamma_{\rm r}^\varepsilon(s^\varepsilon,\boldsymbol{Y}_T^\varepsilon,\boldsymbol{V}_T^\varepsilon)t-t_{\rm r}^\varepsilon(s^\varepsilon,\boldsymbol{Y}_T^\varepsilon,\boldsymbol{V}_T^\varepsilon)\Big) \\ &= \frac{\rho^\varepsilon k_o^2}{(4\pi)^2\varepsilon^{10}|\boldsymbol{X}_T(s)|^2} f^\varepsilon\Big(\gamma_{\rm r}(s,\boldsymbol{Y}_T,\boldsymbol{V}_T)t-t_{\rm r}(s,\boldsymbol{Y}_T,\boldsymbol{V}_T)\Big), \end{aligned} \tag{A.5}$$

where $k_o^\varepsilon = \omega_o^\varepsilon/c_o = \varepsilon^{-5}k_o$ is the wave number. The Doppler coefficients are defined by

$$\begin{aligned} \gamma_{\rm r}^\varepsilon(s^\varepsilon,\boldsymbol{Y}^\varepsilon,\boldsymbol{V}^\varepsilon) := 1-\frac{\boldsymbol{V}^\varepsilon}{c_o}\cdot\Big(\frac{\boldsymbol{Y}^\varepsilon+s^\varepsilon\boldsymbol{V}^\varepsilon-\boldsymbol{X}_R^\varepsilon(s^\varepsilon)}{|\boldsymbol{Y}^\varepsilon+s^\varepsilon\boldsymbol{V}^\varepsilon-\boldsymbol{X}_R^\varepsilon(s^\varepsilon)|}+\frac{\boldsymbol{Y}^\varepsilon+s^\varepsilon\boldsymbol{V}^\varepsilon-\boldsymbol{X}_E^\varepsilon)}{|\boldsymbol{Y}^\varepsilon+s^\varepsilon\boldsymbol{V}^\varepsilon-\boldsymbol{X}_E^\varepsilon|}\Big) \\ +\frac{\boldsymbol{V}_R^\varepsilon}{c_o}\cdot\frac{\boldsymbol{Y}^\varepsilon+s^\varepsilon\boldsymbol{V}^\varepsilon-\boldsymbol{X}_R^\varepsilon(s^\varepsilon)}{|\boldsymbol{Y}^\varepsilon+s^\varepsilon\boldsymbol{V}^\varepsilon-\boldsymbol{X}_R^\varepsilon(s^\varepsilon)|}, \end{aligned}$$

and

$$\widetilde{\gamma}_{\rm r}^{\varepsilon}(s^{\varepsilon},\boldsymbol{Y}^{\varepsilon},\boldsymbol{V}^{\varepsilon}):=1-\frac{\boldsymbol{V}^{\varepsilon}}{c_o}\cdot\Big(\frac{\boldsymbol{Y}^{\varepsilon}+s^{\varepsilon}\boldsymbol{V}^{\varepsilon}-\boldsymbol{X}_R^{\varepsilon}(s^{\varepsilon})}{|\boldsymbol{Y}^{\varepsilon}+s^{\varepsilon}\boldsymbol{V}^{\varepsilon}-\boldsymbol{X}_R^{\varepsilon}(s^{\varepsilon})|}+\frac{\boldsymbol{Y}^{\varepsilon}+s^{\varepsilon}\boldsymbol{V}^{\varepsilon}-\boldsymbol{X}_E^{\varepsilon})}{|\boldsymbol{Y}^{\varepsilon}+s^{\varepsilon}\boldsymbol{V}^{\varepsilon}-\boldsymbol{X}_E^{\varepsilon}|}\Big).$$

They are equal to $\gamma_{\rm r}(s,\boldsymbol{Y},\boldsymbol{V})$ and $\widetilde{\gamma}_{\rm r}(s,\boldsymbol{Y},\boldsymbol{V})$ respectively, which are written in the scaled variables as

$$\begin{aligned}\gamma_{\rm r}(s,\boldsymbol{Y},\boldsymbol{V}):=1-\varepsilon^3\frac{\boldsymbol{V}}{c_o}\cdot\Big(\frac{\boldsymbol{Y}+s\boldsymbol{V}-\varepsilon\boldsymbol{X}_R(s)}{|\boldsymbol{Y}+s\boldsymbol{V}-\varepsilon\boldsymbol{X}_R(s)|}+\frac{\boldsymbol{Y}+s\boldsymbol{V}-\varepsilon\boldsymbol{X}_E)}{|\boldsymbol{Y}+s\boldsymbol{V}-\varepsilon\boldsymbol{X}_E|}\Big)\\ +\varepsilon^4\frac{\boldsymbol{V}_R}{c_o}\cdot\frac{\boldsymbol{Y}+s\boldsymbol{V}-\varepsilon\boldsymbol{X}_R(s)}{|\boldsymbol{Y}+s\boldsymbol{V}-\varepsilon\boldsymbol{X}_R(s)|},\end{aligned}$$

and

$$\widetilde{\gamma}_{\rm r}(s,\boldsymbol{Y},\boldsymbol{V}):=1-\varepsilon^3\frac{\boldsymbol{V}}{c_o}\cdot\Big(\frac{\boldsymbol{Y}+s\boldsymbol{V}-\varepsilon\boldsymbol{X}_R(s)}{|\boldsymbol{Y}+s\boldsymbol{V}-\varepsilon\boldsymbol{X}_R(s)|}+\frac{\boldsymbol{Y}+s\boldsymbol{V}-\varepsilon\boldsymbol{X}_E)}{|\boldsymbol{Y}+s\boldsymbol{V}-\varepsilon\boldsymbol{X}_E|}\Big).$$

The time delay is defined by

$$t_{\rm r}^{\varepsilon}(s,\boldsymbol{Y}^{\varepsilon},\boldsymbol{V}^{\varepsilon})=\frac{|\boldsymbol{Y}^{\varepsilon}+s^{\varepsilon}\boldsymbol{V}^{\varepsilon}-\boldsymbol{X}_E^{\varepsilon}|}{c_o}+\frac{|\boldsymbol{Y}^{\varepsilon}+s^{\varepsilon}\boldsymbol{V}^{\varepsilon}-\boldsymbol{X}_R^{\varepsilon}(s^{\varepsilon})|}{c_o}\widetilde{\gamma}_{\rm r}^{\varepsilon}(s^{\varepsilon},\boldsymbol{Y}^{\varepsilon},\boldsymbol{V}^{\varepsilon}),$$

and it is equal to $t_{\rm r}(s,\boldsymbol{Y},\boldsymbol{V})$ which can be written in the scaled variables as

$$t_{\rm r}(s,\boldsymbol{Y},\boldsymbol{V})=\frac{|\boldsymbol{Y}+s\boldsymbol{V}-\varepsilon\boldsymbol{X}_E|}{c_o}+\frac{|\boldsymbol{Y}+s\boldsymbol{V}-\varepsilon\boldsymbol{X}_R(s)|}{c_o}\widetilde{\gamma}_{\rm r}(s,\boldsymbol{Y},\boldsymbol{V}).$$

A.3. Small-aperture imaging function. The imaging function $\mathcal{I}_j^{\varepsilon}(\boldsymbol{X}^{\varepsilon},\boldsymbol{V}^{\varepsilon})$ for the $j-$th sub-aperture is given by

$$\mathcal{I}_j^{\varepsilon}(\boldsymbol{X}^{\varepsilon},\boldsymbol{V}^{\varepsilon})=\frac{1}{n^{\varepsilon}}\sum_{l=-n^{\varepsilon}/2}^{n^{\varepsilon}/2}\int_{-\Delta T^{\varepsilon}}^{\Delta T^{\varepsilon}}dt\,u_{\rm d}^{\varepsilon}\left(s_{jl}^{\varepsilon}+\frac{t+t_{\rm d}^{\varepsilon}(s_{jl}^{\varepsilon})}{\gamma_{\rm d}^{\varepsilon}(s_{jl}^{\varepsilon})}\right)u_{\rm r}^{\varepsilon}\left(s_{jl}^{\varepsilon}+\frac{t+t_{\rm r}^{\varepsilon}(s_{jl}^{\varepsilon}-S_j^{\varepsilon},\boldsymbol{X}^{\varepsilon},\boldsymbol{V}^{\varepsilon})}{\gamma_{\rm r}^{\varepsilon}(s_{jl}^{\varepsilon}-S_j^{\varepsilon},\boldsymbol{X}^{\varepsilon},\boldsymbol{V}^{\varepsilon})}\right),\qquad(A.6)$$

where we let $\Delta T^{\varepsilon}=\varepsilon^{4-\eta}\Delta T$, for some $\eta\in(0,1)$, be slightly longer than the duration of the pulse $F(Bt/\varepsilon^4)$. In scaled variables $\boldsymbol{X}^{\varepsilon}=\boldsymbol{X}$, $\boldsymbol{V}^{\varepsilon}=\varepsilon^3\boldsymbol{V}$ we can write

$$\mathcal{I}_j^{\varepsilon}(\boldsymbol{X}^{\varepsilon},\boldsymbol{V}^{\varepsilon})\simeq\mathcal{I}_j(\boldsymbol{X},\boldsymbol{V}),$$

where

$$\begin{aligned}\mathcal{I}_j(\boldsymbol{X},\boldsymbol{V})=\frac{\varepsilon^{-11}\rho^{\varepsilon}k_o^2}{(4\pi)^3|\boldsymbol{X}_T(S_j)|^2|\boldsymbol{X}_R(S_j)-\boldsymbol{X}_E|}\frac{1}{n^{\varepsilon}}\sum_{l=-n^{\varepsilon}/2}^{n^{\varepsilon}/2-1}\Big\{\int_{-\Delta T^{\varepsilon}}^{\Delta T^{\varepsilon}}dt\,f^{\varepsilon}(t)\\ \times f^{\varepsilon}\Big(\frac{\big[t+t_{\rm r}(\varepsilon^2\sigma,\boldsymbol{X},\boldsymbol{V})\big]}{\gamma_{\rm r}(\varepsilon^2\sigma,\boldsymbol{X},\boldsymbol{V})}\gamma_{\rm r}(\varepsilon^2\sigma,\boldsymbol{X}_T(S_j),\boldsymbol{V}_T)-t_{\rm r}(\varepsilon^2\sigma,\boldsymbol{X}_T(S_j),\boldsymbol{V}_T)\Big)\Big\}_{\sigma=\varepsilon\Delta sl}.\end{aligned}\qquad(A.7)$$

To study the focusing of $\mathcal{I}_j$ we restrict ourselves to search velocities and locations satisfying

$$\frac{|\boldsymbol{V}^{\varepsilon}-\boldsymbol{V}_T^{\varepsilon}|}{|\boldsymbol{V}_T^{\varepsilon}|}\le\varepsilon^2\ \text{and}\ \frac{|\boldsymbol{X}^{\varepsilon}-\boldsymbol{X}_T^{\varepsilon}(S_j^{\varepsilon})|}{|\boldsymbol{X}_T^{\varepsilon}(S_j^{\varepsilon})|}\le\varepsilon^2,\qquad(A.8)$$

which means that the position and the velocity of the target at slow time $S_j^{\varepsilon}=S_j/\varepsilon^3$ are known a priori with a relative accuracy of the order of ε^2. In physical units this means about 10 m/s for the velocity and 800 m for the position.

The ratio $\gamma_{\rm r}(\varepsilon^2\sigma,\boldsymbol{X}_T(S_j),\boldsymbol{V}_T)/\gamma_{\rm r}(\varepsilon^2\sigma,\boldsymbol{X},\boldsymbol{V})$ can be expanded as $1+O(\varepsilon^5)$, and since $t=O(\varepsilon^3)$,

$$\gamma_{\rm r}(\varepsilon^2\sigma,\boldsymbol{X}_T(S_j),\boldsymbol{V}_T)/\gamma_{\rm r}(\varepsilon^2\sigma,\boldsymbol{X},\boldsymbol{V})t=t+o(\varepsilon^5).$$

Let us denote the argument of the second pulse f^ε in (A.7) by $t-\tau(\sigma,\boldsymbol{X},\boldsymbol{V},\boldsymbol{X}_T(S_j),\boldsymbol{V}_T,S_j)+o(\varepsilon^5)$. The expansion of τ in powers of ε is

$$\begin{aligned}\tau(\sigma,\boldsymbol{X},\boldsymbol{V},\widetilde{\boldsymbol{X}},\widetilde{\boldsymbol{V}},S_j)=&\frac{1}{c_o}\Big[|\widetilde{\boldsymbol{X}}-\varepsilon\boldsymbol{X}_E|-|\boldsymbol{X}-\varepsilon\boldsymbol{X}_E|\\&+|\widetilde{\boldsymbol{X}}-\varepsilon\boldsymbol{X}_R(S_j)|-|\boldsymbol{X}-\varepsilon\boldsymbol{X}_R(S_j)|\Big]\\&-2\varepsilon^3\frac{|\widetilde{\boldsymbol{X}}-\varepsilon\boldsymbol{X}_E|}{c_o}\Big[\frac{\boldsymbol{V}}{c_o}\cdot\frac{\boldsymbol{X}}{|\boldsymbol{X}|}-\frac{\widetilde{\boldsymbol{V}}}{c_o}\cdot\frac{\widetilde{\boldsymbol{X}}}{|\widetilde{\boldsymbol{X}}|}\Big]\\&-2\varepsilon^3\Big[\frac{|\widetilde{\boldsymbol{X}}-\varepsilon\boldsymbol{X}_R(S_j)|-|\boldsymbol{X}-\varepsilon\boldsymbol{X}_R(S_j)|}{c_o}\Big]\frac{\boldsymbol{V}}{c_o}\cdot\frac{\boldsymbol{X}}{|\boldsymbol{X}|}\\&-\varepsilon^2\sigma\Big[\frac{\boldsymbol{V}}{c_o}\cdot\boldsymbol{e}(\boldsymbol{X},S_j)-\frac{\widetilde{\boldsymbol{V}}}{c_o}\cdot\boldsymbol{e}(\widetilde{\boldsymbol{X}},S_j)\Big]\\&-\varepsilon^3\sigma\frac{\boldsymbol{V}_R}{c_o}\cdot\Big[\frac{\widetilde{\boldsymbol{X}}-\varepsilon\boldsymbol{X}_R(S_j)}{|\widetilde{\boldsymbol{X}}-\varepsilon\boldsymbol{X}_R(S_j)|}-\frac{\boldsymbol{X}-\varepsilon\boldsymbol{X}_R(S_j)}{|\boldsymbol{X}-\varepsilon\boldsymbol{X}_R(S_j)|}\Big]+o(\varepsilon^5),\end{aligned}\tag{A.9}$$

where we introduced the notation

$$\boldsymbol{e}(\boldsymbol{X},S_j)=\frac{\boldsymbol{X}-\varepsilon\boldsymbol{X}_E}{|\boldsymbol{X}-\varepsilon\boldsymbol{X}_E|}+\frac{\boldsymbol{X}-\varepsilon\boldsymbol{X}_R(S_j)}{|\boldsymbol{X}-\varepsilon\boldsymbol{X}_R(S_j)|}.\tag{A.10}$$

Note that assumption (A.8) implies that the first square bracket in (A.9) is $O(\varepsilon^2)$, and that the second, third and last square brackets are $O(\varepsilon^5)$. The last but one square bracket is $O(\varepsilon^4)$ if the vector $\boldsymbol{e}(\boldsymbol{X}_T(S_j),S_j)$ has an $O(1)$ component along $\boldsymbol{V}_T$. Otherwise the velocity is nearly orthogonal to $\boldsymbol{e}(\boldsymbol{X}_T(S_j),S_j)$ and this term is $O(\varepsilon^5)$, as well.

We rewrite (A.9) as

$$\begin{aligned}\tau(\sigma,\boldsymbol{X},\boldsymbol{V},\widetilde{\boldsymbol{X}},\widetilde{\boldsymbol{V}},S_j)=\tau(0,\boldsymbol{X},\boldsymbol{V},\widetilde{\boldsymbol{X}},\widetilde{\boldsymbol{V}},S_j)-\varepsilon^4\sigma\psi(\boldsymbol{X},\boldsymbol{V},\widetilde{\boldsymbol{X}},\widetilde{\boldsymbol{V}},S_j)\\-\varepsilon^5\sigma\varphi(\boldsymbol{X},\boldsymbol{V},\widetilde{\boldsymbol{X}},\widetilde{\boldsymbol{V}},S_j)+o(\varepsilon^5),\end{aligned}\tag{A.11}$$

where we introduced the notation

$$\begin{aligned}\psi(\boldsymbol{X},\boldsymbol{V},\widetilde{\boldsymbol{X}},\widetilde{\boldsymbol{V}},S_j)&=\varepsilon^{-2}\Big[\frac{\boldsymbol{V}}{c_o}\cdot\boldsymbol{e}(\boldsymbol{X},S_j)-\frac{\widetilde{\boldsymbol{V}}}{c_o}\cdot\boldsymbol{e}(\widetilde{\boldsymbol{X}},S_j)\Big],\\\varphi(\boldsymbol{X},\boldsymbol{V},\widetilde{\boldsymbol{X}},\widetilde{\boldsymbol{V}},S_j)&=\varepsilon^{-2}\frac{\boldsymbol{V}_R}{c_o}\cdot\Big[\frac{\widetilde{\boldsymbol{X}}-\varepsilon\boldsymbol{X}_R(S_j)}{|\widetilde{\boldsymbol{X}}-\varepsilon\boldsymbol{X}_R(S_j)|}-\frac{\boldsymbol{X}-\varepsilon\boldsymbol{X}_R(S_j)}{|\boldsymbol{X}-\varepsilon\boldsymbol{X}_R(S_j)|}\Big].\end{aligned}\tag{A.12}$$

By assumption (A.8), both ψ and φ are at most $O(1)$. We also have

$$\tau(0,\boldsymbol{X},\boldsymbol{V},\widetilde{\boldsymbol{X}},\widetilde{\boldsymbol{V}},S_j)=\mathcal{T}(\boldsymbol{X},\boldsymbol{V},\widetilde{\boldsymbol{X}},\widetilde{\boldsymbol{V}},S_j)+O(\varepsilon^5),$$

with

$$\begin{aligned}\mathcal{T}(\boldsymbol{X},\boldsymbol{V},\widetilde{\boldsymbol{X}},\widetilde{\boldsymbol{V}},S_j)=\frac{1}{c_o}\Big[|\widetilde{\boldsymbol{X}}-\varepsilon\boldsymbol{X}_E|-|\boldsymbol{X}-\varepsilon\boldsymbol{X}_E|\\+|\widetilde{\boldsymbol{X}}-\varepsilon\boldsymbol{X}_R(S_j)|-|\boldsymbol{X}-\varepsilon\boldsymbol{X}_R(S_j)|\Big].\end{aligned}\tag{A.13}$$

Substituting in (A.7) and using the expression (A.1) of the pulse we obtain that the sum in l can be replaced

by a continuous integral in σ and

$$\mathcal{I}_j(\boldsymbol{X},\boldsymbol{V}) = \frac{4\varepsilon^{-11}\rho^\varepsilon k_o^2}{(4\pi)^3|\boldsymbol{X}_T(S_j)|^2|\boldsymbol{X}_R(S_j)-\boldsymbol{X}_E|}\frac{1}{\Delta S}\int_{-\Delta S/2}^{\Delta S/2} d\sigma \int_{-\Delta T^\varepsilon}^{\Delta T^\varepsilon} dt\, F(\varepsilon^{-4}Bt)$$
$$\times F\Big[\varepsilon^{-4}B\big(t-\mathcal{T}(\boldsymbol{X},\boldsymbol{V},\boldsymbol{X}_T(S_j),\boldsymbol{V}_T,S_j)\big)+\sigma B\psi(\boldsymbol{X},\boldsymbol{V},\boldsymbol{X}_T(S_j),\boldsymbol{V}_T,S_j)\Big]\cos(\varepsilon^{-5}\omega_o t)$$
$$\times\cos\Big\{\varepsilon^{-5}\omega_o\Big[t-\tau(0,\boldsymbol{X},\boldsymbol{V},\boldsymbol{X}_T(S_j),\boldsymbol{V}_T,S_j)+\varepsilon^4\sigma\psi(\boldsymbol{X},\boldsymbol{V},\boldsymbol{X}_T(S_j),\boldsymbol{V}_T,S_j)$$
$$+\varepsilon^5\sigma\varphi(\boldsymbol{X},\boldsymbol{V},\boldsymbol{X}_T(S_j),\boldsymbol{V}_T,S_j)\Big]\Big\}. \tag{A.14}$$

To analyze the focusing of $\mathcal{I}_j(\boldsymbol{X},\boldsymbol{V})$ we evaluate next the two integrals in (A.14). Since σ appears in the argument of the second F, we write it in terms of its Fourier transform $\widehat{F}$, whose support is the interval $[-\pi,\pi]$. Now we can integrate over σ and obtain

$$\mathcal{I}_j(\boldsymbol{X},\boldsymbol{V}) \approx \frac{\varepsilon^{-7}\rho^\varepsilon k_o^2}{(4\pi)^3 B|\boldsymbol{X}_T(S_j)|^2|\boldsymbol{X}_R(S_j)-\boldsymbol{X}_E|}\int\frac{d\omega}{2\pi}|\widehat{F}(\omega)|^2\exp\Big[i\frac{\omega B\mathcal{T}(\boldsymbol{X},\boldsymbol{V},\boldsymbol{X}_T(S_j),\boldsymbol{V}_T,S_j)}{\varepsilon^4}\Big]$$
$$\times\sum_{q=1}^{2}\exp\Big[i(-1)^q\frac{\omega_o\tau(0,\boldsymbol{X},\boldsymbol{V},\boldsymbol{X}_T(S_j),\boldsymbol{V}_T,S_j)}{\varepsilon^5}\Big]$$
$$\times\operatorname{sinc}\Big\{\frac{\omega_o\Delta S}{2\varepsilon}\Big[\psi(\boldsymbol{X},\boldsymbol{V},\boldsymbol{X}_T(S_j),\boldsymbol{V}_T,S_j)\Big(1+\varepsilon(-1)^q\frac{\omega B}{\omega_o}\Big)+\varepsilon\varphi(\boldsymbol{X},\boldsymbol{V},\boldsymbol{X}_T(S_j),\boldsymbol{V}_T,S_j)\Big]\Big\}, \tag{A.15}$$

where the approximation sign is because we neglected the term with the rapidly oscillating exponential $\exp\big\{i(-1)^q\varepsilon^{-5}\omega_o[2t-\tau(0)]\big\}$ which gives a negligible contribution when we integrate over t. We also used

$$\int_{-\Delta T^\varepsilon}^{\Delta T^\varepsilon} dt\, e^{-i\frac{Bt}{\varepsilon^4}(\omega+\omega')} \approx \frac{2\pi\varepsilon^4}{B}\delta(\omega+\omega'),$$

and $\widehat{F}(-\omega)=\overline{\widehat{F}(\omega)}$, because the baseband pulse is real valued.

A.3.1. Target vector location orthogonal to target velocity. We first analyze the resolution properties of the sub-aperture imaging function (A.15) in the case where $\psi = O(\varepsilon)$, which occurs when the target location $\boldsymbol{X}_T(S_j)$ is almost orthogonal to the velocity. Then the ω dependent term is negligible in the argument of the sinc function and the result simplifies to

$$\mathcal{I}_j(\boldsymbol{X},\boldsymbol{V}) \approx \frac{2\varepsilon^{-7}\rho^\varepsilon k_o^2}{(4\pi)^3 B|\boldsymbol{X}_T(S_j)|^2|\boldsymbol{X}_R(S_j)-\boldsymbol{X}_E|}\cos\Big[\frac{\omega_o\tau(0,\boldsymbol{X},\boldsymbol{V},\boldsymbol{X}_T(S_j),\boldsymbol{V}_T,S_j)}{\varepsilon^5}\Big]$$
$$\times\mathcal{F}\Big(\frac{B\mathcal{T}(\boldsymbol{X},\boldsymbol{V},\boldsymbol{X}_T(S_j),\boldsymbol{V}_T,S_j)}{\varepsilon^4}\Big)$$
$$\times\operatorname{sinc}\Big\{\frac{\omega_o\Delta S}{2}\Big[\frac{\psi(\boldsymbol{X},\boldsymbol{V},\boldsymbol{X}_T(S_j),\boldsymbol{V}_T,S_j)}{\varepsilon}+\varphi(\boldsymbol{X},\boldsymbol{V},\boldsymbol{X}_T(S_j),\boldsymbol{V}_T,S_j)\Big]\Big\}, \tag{A.16}$$

where we introduced the new pulse $\mathcal{F}$, given by the autocorrelation of the two pulses F,

$$\mathcal{F}(t) = \int\frac{d\omega}{2\pi}|\widehat{F}(\omega)|^2 e^{i\omega t}.$$

The focusing of (A.16) is determined by the support of $\mathcal{F}$ and of the sinc function. We conclude that $\mathcal{I}_j(\boldsymbol{X},\boldsymbol{V})$ is large for

$$\big|\mathcal{T}(\boldsymbol{X},\boldsymbol{V},\boldsymbol{X}_T(S_j),\boldsymbol{V}_T,S_j)\big| \le \frac{\varepsilon^4}{B} \tag{A.17}$$

and

$$\Big|\frac{\psi(\boldsymbol{X},\boldsymbol{V},\boldsymbol{X}_T(S_j),\boldsymbol{V}_T,S_j)}{\varepsilon}+\varphi(\boldsymbol{X},\boldsymbol{V},\boldsymbol{X}_T(S_j),\boldsymbol{V}_T,S_j)\Big|\le\frac{2\pi}{\omega_o\Delta S}. \tag{A.18}$$

To interpret the estimate (A.17), let us expand (A.13) in powers of ε. By assumption (A.8) we obtain

$$\Big|(\boldsymbol{X}_T(S_j)-\boldsymbol{X})\cdot\boldsymbol{e}\big(\boldsymbol{X}_T(S_j),S_j\big)\Big|\le\frac{c_o}{B}\varepsilon^4, \tag{A.19}$$

where we see from definition (A.10) that

$$\boldsymbol{e}\big(\boldsymbol{X}_T(S_j),S_j\big)=2\frac{\boldsymbol{X}_T(S_j)}{|\boldsymbol{X}_T(S_j)|}+O(\varepsilon). \tag{A.20}$$

Therefore, the location of the target is localized along the vector $\boldsymbol{e}\big(\boldsymbol{X}_T(S_j),S_j\big)$, which points nearly in the direction of $\boldsymbol{X}_T(S_j)$ in our case, with an $O(\varepsilon^4)$ precision. Recalling the scaling of the bandwidth, the bound in (A.19) is proportional to c_o/B^ε, the classic range resolution, as stated in Proposition 3.1.

To interpret the estimate (A.18), we expand in powers of ε the expressions of ψ and φ. We obtain that

$$\Big|\frac{(\boldsymbol{V}_T-\boldsymbol{V})}{\varepsilon c_o}\cdot\boldsymbol{e}(\boldsymbol{X}_T(S_j),S_j)+\Big(\mathbf{P}_{TR}(S_j)\frac{\boldsymbol{V}_T-\varepsilon\boldsymbol{V}_R}{\varepsilon c_o}+\mathbf{P}_{TE}(S_j)\frac{\boldsymbol{V}_T}{\varepsilon c_o}\Big)\cdot(\boldsymbol{X}_T(S_j)-\boldsymbol{X})\Big|\le\frac{2\pi\varepsilon^2}{\omega_o\Delta S}, \tag{A.21}$$

where we introduced the matrices

$$\mathbf{P}_{TE}(S_j)=\frac{\mathbf{I}-\boldsymbol{m}_{TE}(S_j)\boldsymbol{m}_{TE}(S_j)^T}{|\boldsymbol{X}_T(S_j)-\varepsilon\boldsymbol{X}_E|},\quad \mathbf{P}_{TR}(S_j)=\frac{\mathbf{I}-\boldsymbol{m}_{TR}(S_j)\boldsymbol{m}_{TR}(S_j)^T}{|\boldsymbol{X}_T(S_j)-\varepsilon\boldsymbol{X}_R(S_j)|}, \tag{A.22}$$

defined in terms of the unit vectors

$$\boldsymbol{m}_{TE}(S_j)=\frac{\boldsymbol{X}_T(S_j)-\varepsilon\boldsymbol{X}_E}{|\boldsymbol{X}_T(S_j)-\varepsilon\boldsymbol{X}_E|},\quad \boldsymbol{m}_{TR}(S_j)=\frac{\boldsymbol{X}_T(S_j)-\varepsilon\boldsymbol{X}_R(S_j)}{|\boldsymbol{X}_T(S_j)-\varepsilon\boldsymbol{X}_R(S_j)|}. \tag{A.23}$$

If $\boldsymbol{V}=\boldsymbol{V}_T$, then (A.21) shows that $\boldsymbol{X}_T^\varepsilon=\boldsymbol{X}_T(S_j)$ can be localized with a precision of the order of

$$\frac{\varepsilon^3\lambda_o|\boldsymbol{X}_T(S_j)|}{a_T}=\frac{\lambda_o^\varepsilon|\boldsymbol{X}_T^\varepsilon(S_j)|}{a_T^\varepsilon}$$

in the direction of $\boldsymbol{V}_T$ and

$$\frac{\varepsilon^2\lambda_o|\boldsymbol{X}_T(S_j)|}{a_R}=\frac{\lambda_o^\varepsilon|\boldsymbol{X}_T(S_j)|}{a_R^\varepsilon}$$

in the direction of $\boldsymbol{V}_R$. These are the classical Rayleigh resolution formulas. If $\boldsymbol{X}=\boldsymbol{X}_T$, then the estimate (A.21) shows that $\boldsymbol{V}_T^\varepsilon=\varepsilon^3\boldsymbol{V}_T$ can be estimated in the direction $\boldsymbol{e}\big(\boldsymbol{X}_T(S_j),S_j\big)$ with a precision

$$\frac{\varepsilon^6\lambda_o}{\Delta S}=\frac{\lambda_o^\varepsilon}{\Delta S^\varepsilon}.$$

These are the results stated in Proposition 3.1, which are rewritten there in simpler form using the approximations

$$\boldsymbol{m}_{TE}\approx\boldsymbol{m}_{TR}\approx\frac{\boldsymbol{X}_T(S_j)}{|\boldsymbol{X}_T(S_j)|}=\boldsymbol{m}(0),$$

and

$$\mathbf{P}_{TE}\approx\mathbf{P}_{TR}\approx\frac{\mathbf{I}-\boldsymbol{m}(0)\boldsymbol{m}(0)^T}{|\boldsymbol{X}_T(S_j)|}.$$

A.3.2. Target vector location not orthogonal to target velocity. The sub-aperture imaging function (A.15) is large if (A.17) holds and if the argument in the sinc function is less than π. However, when $\boldsymbol{X}_T(S_j)$ is not orthogonal to $\boldsymbol{V}_T$, the ω dependent term in the argument of the sinc function cannot be neglected, because $\psi = O(1)$. The support of the sinc function is essentially an interval of order one, so the sub-aperture imaging function (A.15) is large when the argument in the sinc function is less than π for all ω in this interval, which in fact imposes

$$\left|\frac{\psi(\boldsymbol{X},\boldsymbol{V},\boldsymbol{X}_T(S_j),\boldsymbol{V}_T,S_j)}{\varepsilon} + \varphi(\boldsymbol{X},\boldsymbol{V},\boldsymbol{X}_T(S_j),\boldsymbol{V}_T,S_j)\right| \leq O\left(\frac{1}{\omega_o \Delta S}\right). \tag{A.24}$$

This is the same condition as in the previous subsection, although here ψ can be of order $O(1)$. Therefore, the discussion of the previous subsection still holds true.

A.4. Large-aperture imaging function. Here we estimate the focusing of

$$\mathcal{I}^\varepsilon(\boldsymbol{Y}^\varepsilon,\boldsymbol{V}^\varepsilon) = \sum_{j=-N^\varepsilon/2}^{N^\varepsilon/2} \mathcal{I}_j^\varepsilon(\boldsymbol{Y}^\varepsilon + S_j^\varepsilon \boldsymbol{V}^\varepsilon,\boldsymbol{V}^\varepsilon), \tag{A.25}$$

which sums coherently (A.15) over j. We expect an improvement over the sub-aperture images, due to the sum of the highly oscillatory exponentials $\exp\left\{i(-1)^q\omega_o\tau/\varepsilon^5\right\}$ in (A.15).

It is not possible to calculate the sum analytically, unless we use the further assumption that $A_T \ll H_T$. If that is the case, we see from (A.15) and (A.17), (A.19) that all the terms in the sum are large when

$$\left|(\boldsymbol{Y}_T - \boldsymbol{Y})\cdot\frac{\boldsymbol{Y}_T}{|\boldsymbol{Y}_T|}\right| \leq \frac{\varepsilon^4 c_o}{B}. \tag{A.26}$$

This is because

$$\boldsymbol{X}_T(S_j) \approx \boldsymbol{Y}_T \quad \text{and} \quad \boldsymbol{e}(\boldsymbol{X}_T(S_k),S_j) \approx \frac{2\boldsymbol{Y}_T}{|\boldsymbol{Y}_T|}.$$

We also have

$$\begin{aligned}\tau(0,\boldsymbol{X},\boldsymbol{V},\boldsymbol{X}_T(S_j),\boldsymbol{V}_T,S_j) &\approx \frac{2}{c_o}\left(|\boldsymbol{Y}_T + S_j\boldsymbol{V}_T| - |\boldsymbol{Y} + S_j\boldsymbol{V}|\right)\\ &\approx \frac{2}{c_o}\left\{(\boldsymbol{Y}_T-\boldsymbol{Y})\cdot\frac{\boldsymbol{Y}_T}{|\boldsymbol{Y}_T|} + S_j\left[(\boldsymbol{V}_T-\boldsymbol{V})\cdot\frac{\boldsymbol{Y}_T}{|\boldsymbol{Y}_T|} + \boldsymbol{V}\cdot\left(\mathbf{I}-\frac{\boldsymbol{Y}_T}{|\boldsymbol{Y}_T|}\frac{\boldsymbol{Y}_T^T}{|\boldsymbol{Y}_T|}\right)\frac{(\boldsymbol{Y}_T-\boldsymbol{Y})}{|\boldsymbol{Y}_T|}\right]\right\},\end{aligned}$$

so when we sum (A.15) over j we get the sinc factor

$$\operatorname{sinc}\left\{\frac{\omega_o T_{\rm tot}}{\varepsilon^5 c_o}\left[(\boldsymbol{V}_T-\boldsymbol{V})\cdot\frac{\boldsymbol{Y}_T}{|\boldsymbol{Y}_T|} + \boldsymbol{V}\cdot\left(\mathbf{I}-\frac{\boldsymbol{Y}_T}{|\boldsymbol{Y}_T|}\frac{\boldsymbol{Y}_T^T}{|\boldsymbol{Y}_T|}\right)\frac{(\boldsymbol{Y}_T-\boldsymbol{Y})}{|\boldsymbol{Y}_T|}\right]\right\}.$$

Since $\varepsilon^5 c_o/\omega_o = \lambda_o^\varepsilon/(2\pi)$, $\boldsymbol{V}_T = \varepsilon^{-3}\boldsymbol{V}_T^\varepsilon$, $\boldsymbol{V} = \varepsilon^{-3}\boldsymbol{V}$, $\boldsymbol{Y}_T^\varepsilon = \boldsymbol{Y}_T$ and $T_{\rm tot} = \varepsilon^3 T_{\rm tot}^\varepsilon$, this is the result stated in section 3.2, equation (3.14).

If $\boldsymbol{Y} = \boldsymbol{Y}_T$ and $(\boldsymbol{V}_T - \boldsymbol{V})\cdot\frac{\boldsymbol{Y}_T}{|\boldsymbol{Y}_T|} = 0$, then we need to expand the term τ to higher order and we find

$$\tau(0,\boldsymbol{X},\boldsymbol{V},\boldsymbol{X}_T(S_j),\boldsymbol{V}_T,S_j) \approx \frac{1}{c_o}\frac{S_j^2}{|\boldsymbol{Y}_T|}\left(|\boldsymbol{V}|^2 - |\boldsymbol{V}_T|^2\right),$$

so when we sum (A.15) over j we get the factor

$$\Psi\left\{\frac{\omega_o T_{\rm tot}^2}{\varepsilon^5 c_o|\boldsymbol{Y}_T|}\left||\boldsymbol{V}|^2 - |\boldsymbol{V}_T|^2\right|\right\},$$

where $\Psi(s) = (C+iS)(\sqrt{s})/\sqrt{s}$ in terms of the Fresnel integral functions $C(s) = \int_0^s \cos(t^2)dt$ and $S(s) = \int_0^s \sin(t^2)dt$. If $\boldsymbol{V} = \boldsymbol{V}_T + \delta\frac{\boldsymbol{V}_T}{|\boldsymbol{V}_T|}v + \delta\boldsymbol{V}^\perp$, with $\boldsymbol{V}^\perp\cdot\boldsymbol{V}_T = 0$, then $|\boldsymbol{V}|^2 - |\boldsymbol{V}_T|^2 = |\boldsymbol{V}_T|^2(2\delta v + O(\delta^2))$, so that we get the result stated in section 3.2, equation (3.15).

Appendix B. Resolution analysis with two receivers. In this appendix we derive the resolution results stated in section 4, in our regime of separation of scales defined in appendix A. The analysis of the sub-aperture imaging function is in section B.1 and the large aperture case is discussed in section B.2.

B.1. Small-aperture imaging function. The imaging function for the $j-$th sub-aperture is

$$\mathcal{I}_j^\varepsilon(\boldsymbol{X}^\varepsilon,\boldsymbol{V}^\varepsilon)=\frac{1}{n^\varepsilon}\sum_{l=-n^\varepsilon/2}^{n^\varepsilon/2}\int_{-\Delta T^\varepsilon}^{\Delta T^\varepsilon}dt\,u_{\rm r}^\varepsilon\Big(s_{jl}^\varepsilon+\frac{t+t_{\rm r}^\varepsilon(s_{jl}^\varepsilon-S_j^\varepsilon,\boldsymbol{X}^\varepsilon,\boldsymbol{V}^\varepsilon)}{\gamma_{\rm r}^\varepsilon(s_{jl}^\varepsilon-S_j^\varepsilon,\boldsymbol{X}^\varepsilon,\boldsymbol{V}^\varepsilon)}\Big)$$
$$\times u_{\rm r}^{\varepsilon,Z}\Big(s_{jl}^\varepsilon+\frac{t+t_{\rm r}^{\varepsilon,Z}(s_{jl}^\varepsilon-S_j^\varepsilon,\boldsymbol{X}^\varepsilon,\boldsymbol{V}^\varepsilon)}{\gamma_{\rm r}^{\varepsilon,Z}(s_{jl}^\varepsilon-S_j^\varepsilon,\boldsymbol{X}^\varepsilon,\boldsymbol{V}^\varepsilon)}\Big),\tag{B.1}$$

where the Z indexes correspond to the second receiver at location $\boldsymbol{X}_R^{\varepsilon,Z}=\boldsymbol{X}_R^\varepsilon+\boldsymbol{Z}^\varepsilon=\varepsilon(\boldsymbol{X}_R+\boldsymbol{Z})$. In scaled variables we can write

$$\begin{aligned}\mathcal{I}_j(\boldsymbol{X},\boldsymbol{V})\approx\frac{\varepsilon^{-20}(\rho^\varepsilon)^2k_o^4}{(4\pi|\boldsymbol{X}_T(S_j)|)^4}\frac{1}{n^\varepsilon}\sum_{l=-n^\varepsilon/2}^{n^\varepsilon/2}\Big\{\int_{-\Delta T^\varepsilon}^{\Delta T^\varepsilon}dt\\
\times f^\varepsilon\Big(\frac{\big[t+t_{\rm r}(\varepsilon^2\sigma,\boldsymbol{X},\boldsymbol{V})\big]}{\gamma_{\rm r}(\varepsilon^2\sigma,\boldsymbol{X},\boldsymbol{V})}\gamma_{\rm r}(\varepsilon^2\sigma,\boldsymbol{X}_T(S_j),\boldsymbol{V}_T)-t_{\rm r}(\varepsilon^2\sigma,\boldsymbol{X}_T(S_j),\boldsymbol{V}_T)\Big)\\
\times f^\varepsilon\Big(\frac{\big[t+t_{\rm r}^Z(\varepsilon^2\sigma,\boldsymbol{X},\boldsymbol{V})\big]}{\gamma_{\rm r}^Z(\varepsilon^2\sigma,\boldsymbol{X},\boldsymbol{V})}\gamma_{\rm r}^Z(\varepsilon^2\sigma,\boldsymbol{X}_T(S_j),\boldsymbol{V}_T)-t_{\rm r}^Z(\varepsilon^2\sigma,\boldsymbol{X}_T(S_j),\boldsymbol{V}_T)\Big)\Big\}_{\sigma=\varepsilon\Delta sl}.\end{aligned}\tag{B.2}$$

This can be analyzed as in the previous section, by writing the argument of the first pulse f^ε as $t-\tau(\sigma,\boldsymbol{X},\boldsymbol{V},\boldsymbol{X}_T(S_j),\boldsymbol{V}_T,S_j)$, with τ as in (A.11). The argument of the second pulse is similar, given by $t-\tau^Z(\sigma,\boldsymbol{X},\boldsymbol{V},\boldsymbol{X}_T(S_j),\boldsymbol{V}_T,S_j)$, with $\boldsymbol{X}_R$ replaced by $\boldsymbol{X}_R^Z$. We have more explicitly,

$$\begin{aligned}\tau^Z(\sigma,\boldsymbol{X},\boldsymbol{V},\widetilde{\boldsymbol{X}},\widetilde{\boldsymbol{V}},S_j)=&\frac{1}{c_o}\Big[|\widetilde{\boldsymbol{X}}-\varepsilon\boldsymbol{X}_E|-|\boldsymbol{X}-\varepsilon\boldsymbol{X}_E|\\
&+|\widetilde{\boldsymbol{X}}-\varepsilon\boldsymbol{X}_R^Z(S_j)|-|\boldsymbol{X}-\varepsilon\boldsymbol{X}_R^Z(S_j)|\Big]\\
&-2\varepsilon^3\frac{|\widetilde{\boldsymbol{X}}-\varepsilon\boldsymbol{X}_E|}{c_o}\Big[\frac{\boldsymbol{V}}{c_o}\cdot\frac{\boldsymbol{X}}{|\boldsymbol{X}|}-\frac{\widetilde{\boldsymbol{V}}}{c_o}\cdot\frac{\widetilde{\boldsymbol{X}}}{|\widetilde{\boldsymbol{X}}|}\Big]\\
&-2\varepsilon^3\Big[\frac{|\widetilde{\boldsymbol{X}}-\varepsilon\boldsymbol{X}_R^Z(S_j)|-|\boldsymbol{X}-\varepsilon\boldsymbol{X}_R^Z(S_j)|}{c_o}\Big]\frac{\boldsymbol{V}}{c_o}\cdot\frac{\boldsymbol{X}}{|\boldsymbol{X}|}\\
&-\varepsilon^2\sigma\Big[\frac{\boldsymbol{V}}{c_o}\cdot\boldsymbol{e}^Z(\boldsymbol{X},S_j)-\frac{\widetilde{\boldsymbol{V}}}{c_o}\cdot\boldsymbol{e}^Z(\widetilde{\boldsymbol{X}},S_j)\Big]\\
&-\varepsilon^3\sigma\frac{\boldsymbol{V}_R}{c_o}\cdot\Big[\frac{\widetilde{\boldsymbol{X}}-\varepsilon\boldsymbol{X}_R^Z(S_j)}{|\widetilde{\boldsymbol{X}}-\varepsilon\boldsymbol{X}_R^Z(S_j)|}-\frac{\boldsymbol{X}-\varepsilon\boldsymbol{X}_R^Z(S_j)}{|\boldsymbol{X}-\varepsilon\boldsymbol{X}_R^Z(S_j)|}\Big]+o(\varepsilon^5),\end{aligned}\tag{B.3}$$

and

$$\boldsymbol{e}^Z(\boldsymbol{X},S_j)=\frac{\boldsymbol{X}-\varepsilon\boldsymbol{X}_E}{|\boldsymbol{X}-\varepsilon\boldsymbol{X}_E|}+\frac{\boldsymbol{X}-\varepsilon\boldsymbol{X}_R^Z(S_j)}{|\boldsymbol{X}-\varepsilon\boldsymbol{X}_R^Z(S_j)|}.\tag{B.4}$$

We also define $\mathcal{T}^Z$ and ψ^Z and φ^Z as before, with $\boldsymbol{X}_R$ replaced by $\boldsymbol{X}_R^Z$.

Substituting in (B.2) and using the definition of the pulse we get

$$\begin{aligned}
\mathcal{I}_j(\boldsymbol{X},\boldsymbol{V}) \approx{}& \frac{4\varepsilon^{-20}(\rho^\varepsilon)^2k_o^4}{(4\pi|\boldsymbol{X}_T(S_j)|^2)^4\Delta S}\int_{-\Delta S/2}^{\Delta S/2}d\sigma\int_{-\Delta T^\varepsilon}^{\Delta T^\varepsilon}dt\\
&\times F\Big[\varepsilon^{-4}B\big(t-\mathcal{T}(\boldsymbol{X},\boldsymbol{V},\boldsymbol{X}_T(S_j),\boldsymbol{V}_T,S_j)\big)+\sigma B\psi(\boldsymbol{X},\boldsymbol{V},\boldsymbol{X}_T(S_j),\boldsymbol{V}_T,S_j)\Big]\\
&\times F\Big[\varepsilon^{-4}B\big(t-\mathcal{T}^Z(\boldsymbol{X},\boldsymbol{V},\boldsymbol{X}_T(S_j),\boldsymbol{V}_T,S_j)\big)+\sigma B\psi^Z(\boldsymbol{X},\boldsymbol{V},\boldsymbol{X}_T(S_j),\boldsymbol{V}_T,S_j)\Big]\\
&\times\cos\Big\{\varepsilon^{-5}\omega_o\Big[t-\tau(0,\boldsymbol{X},\boldsymbol{V},\boldsymbol{X}_T(S_j),\boldsymbol{V}_T,S_j)+\varepsilon^4\sigma\psi(\boldsymbol{X},\boldsymbol{V},\boldsymbol{X}_T(S_j),\boldsymbol{V}_T,S_j)\\
&\qquad+\varepsilon^5\sigma\varphi(\boldsymbol{X},\boldsymbol{V},\boldsymbol{X}_T(S_j),\boldsymbol{V}_T,S_j)\Big]\Big\}\\
&\times\cos\Big\{\varepsilon^{-5}\omega_o\Big[t-\tau^Z(0,\boldsymbol{X},\boldsymbol{V},\boldsymbol{X}_T(S_j),\boldsymbol{V}_T,S_j)+\varepsilon^4\sigma\psi^Z(\boldsymbol{X},\boldsymbol{V},\boldsymbol{X}_T(S_j),\boldsymbol{V}_T,S_j)\\
&\qquad+\varepsilon^5\sigma\varphi^Z(\boldsymbol{X},\boldsymbol{V},\boldsymbol{X}_T(S_j),\boldsymbol{V}_T,S_j)\Big]\Big\}.
\end{aligned}\tag{B.5}$$

Let us write the product of the cosines as half the sum of the cosines of the difference and sum of their arguments. The rapid oscillations of the cosines due to $\varepsilon^{-5}\omega_o t$ terms make the t integral significant only for the first part, so we can approximate (B.5) by

$$\begin{aligned}
\mathcal{I}_j(\boldsymbol{X},\boldsymbol{V}) \approx{}&\frac{2\varepsilon^{-16}(\rho^\varepsilon)^2k_o^4}{B\Delta S(4\pi|\boldsymbol{X}_T(S_j)|)^4}\int_{-\Delta S/2}^{\Delta S/2}d\sigma\int\frac{d\omega}{2\pi}\,|\hat F(\omega)|^2\\
&\times\exp\Big[i\frac{\omega B\big(\mathcal{T}(\boldsymbol{X},\boldsymbol{V},\boldsymbol{X}_T(S_j),\boldsymbol{V}_T,S_j)-\mathcal{T}^Z(\boldsymbol{X},\boldsymbol{V},\boldsymbol{X}_T(S_j),\boldsymbol{V}_T,S_j)\big)}{\varepsilon^4}\Big]\\
&\times\exp\Big[-i\omega\sigma B\big[\psi(\boldsymbol{X},\boldsymbol{V},\boldsymbol{X}_T(S_j),\boldsymbol{V}_T,S_j)-\psi^Z(\boldsymbol{X},\boldsymbol{V},\boldsymbol{X}_T(S_j),\boldsymbol{V}_T,S_j)\big]\Big]\\
&\times\cos\Big\{\varepsilon^{-5}\omega_o\Big[\tau(0,\boldsymbol{X},\boldsymbol{V},\boldsymbol{X}_T(S_j),\boldsymbol{V}_T,S_j)-\tau^Z(0,\boldsymbol{X},\boldsymbol{V},\boldsymbol{X}_T(S_j),\boldsymbol{V}_T,S_j)\\
&\qquad+\varepsilon^4\sigma\big[\psi(\boldsymbol{X},\boldsymbol{V},\boldsymbol{X}_T(S_j),\boldsymbol{V}_T,S_j)-\psi^Z(\boldsymbol{X},\boldsymbol{V},\boldsymbol{X}_T,(S_j)\boldsymbol{V}_T,S_j)\big]\\
&\qquad+\varepsilon^5\sigma\big[\varphi(\boldsymbol{X},\boldsymbol{V},\boldsymbol{X}_T(S_j),\boldsymbol{V}_T,S_j)-\varphi^Z(\boldsymbol{X},\boldsymbol{V},\boldsymbol{X}_T(S_j),\boldsymbol{V}_T,S_j)\big]\Big]\Big\}.
\end{aligned}\tag{B.6}$$

Now we can integrate over σ and obtain

$$\begin{aligned}
\mathcal{I}_j(\boldsymbol{X},\boldsymbol{V}) \approx{}&\frac{\varepsilon^{-16}(\rho^\varepsilon)^2k_o^4}{B(4\pi|\boldsymbol{X}_T(S_j)|)^4}\int\frac{d\omega}{2\pi}|\hat F(\omega)|^2\\
&\times\exp\Big[i\frac{\omega B}{\varepsilon^4}\big(\mathcal{T}(\boldsymbol{X},\boldsymbol{V},\boldsymbol{X}_T(S_j),\boldsymbol{V}_T,S_j)-\mathcal{T}^Z(\boldsymbol{X},\boldsymbol{V},\boldsymbol{X}_T(S_j),\boldsymbol{V}_T,S_j)\big)\Big]\\
&\times\sum_{q=1}^{2}\exp\Big[i(-1)^q\frac{\omega_o\big(\tau(0,\boldsymbol{X},\boldsymbol{V},\boldsymbol{X}_T(S_j),\boldsymbol{V}_T,S_j)-\tau^Z(0,\boldsymbol{X},\boldsymbol{V},\boldsymbol{X}_T(S_j),\boldsymbol{V}_T,S_j)\big)}{\varepsilon^5}\Big]\\
&\times\operatorname{sinc}\Big\{\frac{\omega_o\Delta S}{2\varepsilon}\Big[\Big(1+\varepsilon(-1)^q\frac{\omega B}{\omega_o}\Big)\Big(\psi(\boldsymbol{X},\boldsymbol{V},\boldsymbol{X}_T(S_j),\boldsymbol{V}_T,S_j)-\psi^Z(\boldsymbol{X},\boldsymbol{V},\boldsymbol{X}_T(S_j),\boldsymbol{V}_T,S_j)\Big)\\
&\qquad+\varepsilon\Big(\varphi(\boldsymbol{X},\boldsymbol{V},\boldsymbol{X}_T(S_j),\boldsymbol{V}_T,S_j)-\varphi^Z(\boldsymbol{X},\boldsymbol{V},\boldsymbol{X}_T(S_j),\boldsymbol{V}_T,S_j)\Big)\Big]\Big\}.
\end{aligned}\tag{B.7}$$

We estimate next the argument of the sinc functions and of the complex exponential. From the definitions of $\mathcal{T}$ and $\mathcal{T}^Z$,

$$\begin{aligned}
\mathcal{T}(\boldsymbol{X},\boldsymbol{V},\widetilde{\boldsymbol{X}},\widetilde{\boldsymbol{V}},S_j)-\mathcal{T}^Z(\boldsymbol{X},\boldsymbol{V},\widetilde{\boldsymbol{X}},\widetilde{\boldsymbol{V}},S_j) = \frac{1}{c_o}\Big[&|\widetilde{\boldsymbol{X}}-\varepsilon\boldsymbol{X}_R(S_j)|\\
&-|\boldsymbol{X}-\varepsilon\boldsymbol{X}_R(S_j)|-|\widetilde{\boldsymbol{X}}-\varepsilon\boldsymbol{X}_R^Z(S_j)|+|\boldsymbol{X}-\varepsilon\boldsymbol{X}_R^Z(S_j)|\Big].
\end{aligned}\tag{B.8}$$

The definition of τ and τ^Z gives

$$\tau(0,\boldsymbol{X},\boldsymbol{V},\widetilde{\boldsymbol{X}},\widetilde{\boldsymbol{V}},S_j)-\tau^Z(0,\boldsymbol{X},\boldsymbol{V},\widetilde{\boldsymbol{X}},\widetilde{\boldsymbol{V}},S_j)=\big(\mathcal{T}(\boldsymbol{X},\boldsymbol{V},\widetilde{\boldsymbol{X}},\widetilde{\boldsymbol{V}},S_j) \\ -\mathcal{T}^Z(\boldsymbol{X},\boldsymbol{V},\widetilde{\boldsymbol{X}},\widetilde{\boldsymbol{V}},S_j)\big)\Big(1-2\varepsilon^3\frac{\boldsymbol{V}}{c_o}\cdot\frac{\boldsymbol{X}}{|\boldsymbol{X}|}\Big), \tag{B.9}$$

and from the definitions of ψ,ψ^Z,φ and φ^Z we get

$$\psi(\boldsymbol{X},\boldsymbol{V},\widetilde{\boldsymbol{X}},\widetilde{\boldsymbol{V}},S_j)-\psi^Z(\boldsymbol{X},\boldsymbol{V},\widetilde{\boldsymbol{X}},\widetilde{\boldsymbol{V}},S_j)=\varepsilon^{-2}\Big[\frac{\boldsymbol{V}}{c_o}\cdot\Big(\frac{\boldsymbol{X}-\varepsilon\boldsymbol{X}_R(S_j)}{|\boldsymbol{X}-\varepsilon\boldsymbol{X}_R(S_j)|}-\frac{\boldsymbol{X}-\varepsilon\boldsymbol{X}_R^Z(S_j)}{|\boldsymbol{X}-\varepsilon\boldsymbol{X}_R^Z(S_j)|}\Big) \\ -\frac{\widetilde{\boldsymbol{V}}}{c_o}\cdot\Big(\frac{\widetilde{\boldsymbol{X}}-\varepsilon\boldsymbol{X}_R(S_j)}{|\widetilde{\boldsymbol{X}}-\varepsilon\boldsymbol{X}_R(S_j)|}-\frac{\widetilde{\boldsymbol{X}}-\varepsilon\boldsymbol{X}_R^Z(S_j)}{|\widetilde{\boldsymbol{X}}-\varepsilon\boldsymbol{X}_R^Z(S_j)|}\Big)\Big], \tag{B.10}$$

and

$$\varphi(\boldsymbol{X},\boldsymbol{V},\widetilde{\boldsymbol{X}},\widetilde{\boldsymbol{V}},S_j)-\varphi^Z(\boldsymbol{X},\boldsymbol{V},\widetilde{\boldsymbol{X}},\widetilde{\boldsymbol{V}},S_j)=\varepsilon^{-2}\frac{\boldsymbol{V}_R}{c_o}\cdot\Big[\frac{\widetilde{\boldsymbol{X}}-\varepsilon\boldsymbol{X}_R(S_j)}{|\widetilde{\boldsymbol{X}}-\varepsilon\boldsymbol{X}_R(S_j)|} \\ -\frac{\boldsymbol{X}-\varepsilon\boldsymbol{X}_R(S_j)}{|\boldsymbol{X}-\varepsilon\boldsymbol{X}_R(S_j)|}-\frac{\widetilde{\boldsymbol{X}}-\varepsilon\boldsymbol{X}_R^Z(S_j)}{|\widetilde{\boldsymbol{X}}-\varepsilon\boldsymbol{X}_R^Z(S_j)|}+\frac{\boldsymbol{X}-\varepsilon\boldsymbol{X}_R^Z(S_j)}{|\boldsymbol{X}-\varepsilon\boldsymbol{X}_R^Z(S_j)|}\Big]. \tag{B.11}$$

The source information is canceled out in these expressions, so the results appear independent of the knowledge of the source. However, we used $\boldsymbol{X}_E$ in the Doppler factors in (B.1), so the image has some sensitivity to knowing $\boldsymbol{X}_E$.

It remains to expand the right hand sides in (B.8)-(B.11) in order to estimate the resolution of (B.7). We obtain that

$$c_o\big(\mathcal{T}(\boldsymbol{X},\boldsymbol{V},\widetilde{\boldsymbol{X}},\widetilde{\boldsymbol{V}},S_j)-\mathcal{T}^Z(\boldsymbol{X},\boldsymbol{V},\widetilde{\boldsymbol{X}},\widetilde{\boldsymbol{V}},S_j)\big)=\varepsilon\big(\widetilde{\boldsymbol{X}}-\boldsymbol{X}\big)\cdot\mathbf{P}_{TR}\boldsymbol{Z}+O(\varepsilon^4), \tag{B.12}$$

where the matrix $\mathbf{P}_{TR}$ is defined in (A.22). Since this argument must be in the support of the pulse, we obtain that

$$\Big|\big(\boldsymbol{X}_T(S_j)-\boldsymbol{X}\big)\cdot\mathbf{P}_{TR}\boldsymbol{Z}\Big|\le\varepsilon^3\frac{c_o}{B}, \tag{B.13}$$

or in real units

$$\Big|\big(\boldsymbol{X}_T^\varepsilon(S_j^\varepsilon)-\boldsymbol{X}^\varepsilon\big)\cdot\mathbf{P}_{TR}\boldsymbol{Z}^\varepsilon\Big|\le\frac{c_o}{B^\varepsilon}.$$

Thus, we estimate with the precision c_o/B^ε the inner product between the target location error $\boldsymbol{X}_T^\varepsilon(S_j^\varepsilon)-\boldsymbol{X}^\varepsilon$ and $\mathbf{P}_{TR}\boldsymbol{Z}^\varepsilon$, which is $O(\varepsilon|\boldsymbol{Z}|/|\boldsymbol{X}_T(S_j)|)$ in our scaling. Since $\boldsymbol{X}_T^\varepsilon(S_j^\varepsilon)$ is approximately in the null space of $\mathbf{P}_{TR}$, we see that we estimate $\boldsymbol{X}_T^\varepsilon(S_j^\varepsilon)-\boldsymbol{X}^\varepsilon$ in the cross-range plane, orthogonal to $\boldsymbol{X}_T^\varepsilon(S_j^\varepsilon)$. Moreover, the receiver separation $\boldsymbol{Z}^\varepsilon$ should be in this plane, to get the best possible estimate.

The expansion of (B.10) gives

$$\varepsilon^{-1}\big(\psi(\boldsymbol{X},\boldsymbol{V},\boldsymbol{X}_T(S_j)\boldsymbol{V}_T,S_j)-\psi^Z(\boldsymbol{X},\boldsymbol{V},\boldsymbol{X}_T(S_j),\boldsymbol{V}_T,S_j)\big)=\frac{(\boldsymbol{V}-\boldsymbol{V}_T)}{\varepsilon^2c_o}\cdot\mathbf{P}_{TR}\boldsymbol{Z} \\ +\frac{(\boldsymbol{X}-\boldsymbol{X}_T(S_j))}{\varepsilon^2}\cdot\frac{\big(\mathbf{P}_{TR}-\mathbf{P}_{TR}^Z\big)\boldsymbol{V}_T}{\varepsilon c_o}+O(\varepsilon), \tag{B.14}$$

where $\mathbf{P}_{TR}^Z$ is similar to $\mathbf{P}_{TR}$ defined in (A.22), with $\boldsymbol{X}_R$ replaced by $\boldsymbol{X}_R^Z=\boldsymbol{X}_R+\boldsymbol{Z}$. We have in particular that $(\mathbf{P}_{TR}-\mathbf{P}_{TR}^Z)/\varepsilon$ is an order one matrix. The expansion of (B.11) is

$$\varphi(\boldsymbol{X},\boldsymbol{V},\boldsymbol{X}_T(S_j),\boldsymbol{V}_T,S_j)-\varphi^Z(\boldsymbol{X},\boldsymbol{V},\boldsymbol{X}_T(S_j),\boldsymbol{V}_T,S_j)=\varepsilon\frac{(\boldsymbol{X}-\boldsymbol{X}_T(S_j))}{\varepsilon^2}\cdot\frac{\big(\mathbf{P}_{TR}-\mathbf{P}_{TR}^Z\big)\boldsymbol{V}_R}{\varepsilon c_o}+O(\varepsilon^2). \tag{B.15}$$

Substituting in the argument of the sinc function in (B.7), we get that

$$\Big|\frac{(\boldsymbol{V}-\boldsymbol{V}_T)}{c_o}\cdot\mathbf{P}_{TR}\boldsymbol{Z}+(\boldsymbol{X}-\boldsymbol{X}_T(S_j))\cdot\frac{(\mathbf{P}_{TR}-\mathbf{P}^Z_{TR})\boldsymbol{V}_T}{\varepsilon c_o}\Big|\le\frac{\varepsilon^2}{\omega_o\Delta S}. \tag{B.16}$$

As in the one-receiver case, equation (3.4), we can only localize a linear combination of the velocity and target location error. However, since the receiver separation is $\boldsymbol{Z}^\varepsilon=\varepsilon\boldsymbol{Z}$, this localization is with a precision $O(\varepsilon^2)$. This is not an improvement of the assumption (A.8) that we began with, but it is consistent with it.

The results in Proposition 4.1 follow from (B.13), (B.16), and the approximations

$$\mathbf{P}_{TR}\approx\frac{\mathbf{I}-\boldsymbol{m}(0)\boldsymbol{m}(0)^T}{|\boldsymbol{X}_T(S_j)|},\qquad(\mathbf{P}_{TR}-\mathbf{P}^Z_{TR})\boldsymbol{V}_T\approx-\frac{\varepsilon(\boldsymbol{Z}\cdot\boldsymbol{V}_T)}{|\boldsymbol{X}_T|^2}\boldsymbol{m}(S_j).$$

B.2. Large-aperture imaging function. The large aperture imaging function

$$\mathcal{I}^\varepsilon(\boldsymbol{Y}^\varepsilon,\boldsymbol{V}^\varepsilon)=\sum_{j=-N^\varepsilon/2}^{N^\varepsilon/2}\mathcal{I}^\varepsilon_j(\boldsymbol{Y}^\varepsilon+S^\varepsilon_j\boldsymbol{V}^\varepsilon,\boldsymbol{V}^\varepsilon), \tag{B.17}$$

improves the estimate (B.16), due to the coherent sum over j of the $\omega_o(\tau-\tau^Z)\varepsilon^{-5}$ rapidly oscillating terms in (B.7). As was the case in the previous appendix, it is difficult to calculate this sum analytically, unless $A_T\ll H_T$. If this is the case, we get from (B.7) and (B.13) that all the terms in the sum are large when

$$\left|(\boldsymbol{Y}_T-\boldsymbol{Y})\cdot\left(\mathbf{I}-\boldsymbol{m}(0)\boldsymbol{m}(0)^T\right)\boldsymbol{Z}\right|\le O\left(\frac{\varepsilon^3c_oH_T}{B}\right), \tag{B.18}$$

or, equivalently,

$$\left|\frac{(\boldsymbol{Y}^\varepsilon_T-\boldsymbol{Y}^\varepsilon)}{|\boldsymbol{Y}^\varepsilon_T|}\cdot\left(\mathbf{I}-\boldsymbol{m}(0)\boldsymbol{m}(0)^T\right)\boldsymbol{Z}^\varepsilon\right|\le O\left(\frac{c_o}{B^\varepsilon}\right). \tag{B.19}$$

Here we used the approximation

$$\mathbf{P}_{TR}\approx\frac{\mathbf{I}-\boldsymbol{m}(0)\boldsymbol{m}(0)^T}{|\boldsymbol{Y}_T|},\qquad\boldsymbol{m}(0)=\frac{\boldsymbol{Y}_T}{|\boldsymbol{Y}_T|},$$

and $|\boldsymbol{Y}_T|\approx H_T$. The sum over j is obtained from (B.12), and $\boldsymbol{X}_T(S_j)-\boldsymbol{X}=\boldsymbol{Y}_T-\boldsymbol{Y}+S_j(\boldsymbol{V}_T-\boldsymbol{V})$. We obtain approximately the sinc factor

$$\operatorname{sinc}\left[\frac{\omega_oT_{\rm tot}}{\varepsilon^4c_o}(\boldsymbol{V}_T-\boldsymbol{V})\cdot\frac{\left(\mathbf{I}-\boldsymbol{m}(0)\boldsymbol{m}(0)^T\right)\boldsymbol{Z}}{|\boldsymbol{Y}_T|}\right],$$

from which we deduce that

$$\left|(\boldsymbol{V}_T-\boldsymbol{V})\cdot\left(\mathbf{I}-\boldsymbol{m}(0)\boldsymbol{m}(0)^T\right)\boldsymbol{Z}\right|\le O\left(\frac{\varepsilon^4\lambda_oH_T}{T_{\rm tot}}\right), \tag{B.20}$$

or, equivalently, in the scaled variables,

$$\left|\frac{(\boldsymbol{V}^\varepsilon_T-\boldsymbol{V}^\varepsilon)}{|\boldsymbol{V}^\varepsilon_T|}\cdot\left(\mathbf{I}-\boldsymbol{m}(0)\boldsymbol{m}(0)^T\right)\boldsymbol{Z}^\varepsilon\right|\le O\left(\frac{\lambda^\varepsilon_oH^\varepsilon_T}{A^\varepsilon_T}\right). \tag{B.21}$$

Note that for horizontal $\boldsymbol{Z}$ we have

$$\left(\mathbf{I}-\boldsymbol{m}(0)\boldsymbol{m}(0)^T\right)\boldsymbol{Z}\approx\boldsymbol{Z},$$

so the estimates above determine the target location and velocity along $\boldsymbol{Z}$. To see the target location in range, we need to set $\boldsymbol{V}_T = \boldsymbol{V}$ in the imaging function. Then, we get from (B.9) and the further expansion in (B.12) that

$$\left|(\boldsymbol{Y} - \boldsymbol{Y}_T) \cdot \frac{(\mathbf{P}_{TR} - \mathbf{P}^Z_{TR})\boldsymbol{V}_T}{\varepsilon c_o}\right| \leq O\left(\frac{\varepsilon^4}{\omega_o T_{\rm tot}}\right). \tag{B.22}$$

We have to leading order

$$(\mathbf{P}_{TR} - \mathbf{P}^Z_{TR})\boldsymbol{V}_T = -\frac{\boldsymbol{Y}_T + \boldsymbol{V}_T S_j}{|\boldsymbol{Y}_T + \boldsymbol{V}_T S_j|^3}\varepsilon \boldsymbol{Z} \cdot \boldsymbol{V}_T \approx -\frac{\varepsilon(\boldsymbol{Z} \cdot \boldsymbol{V}_T)}{|\boldsymbol{Y}_T|^2}\boldsymbol{m}(0), \tag{B.23}$$

so (B.22) gives

$$\left|\frac{(\boldsymbol{Y}_T - \boldsymbol{Y})}{|\boldsymbol{Y}_T|} \cdot \boldsymbol{m}(0)\right| \leq O\left(\frac{\varepsilon^4 \lambda_o H_T}{T_{\rm tot} \boldsymbol{Z} \cdot \boldsymbol{V}_T}\right). \tag{B.24}$$

With $Z_\parallel = \boldsymbol{Z} \cdot \boldsymbol{V}_T/|\boldsymbol{V}_T|$, and in real units, this gives the range resolution of order $\lambda_o^\varepsilon (H_T^\varepsilon)^2/(Z_\parallel^\varepsilon A_T^\varepsilon)$ stated in section 4.

REFERENCES

[1] M. Antoniou, Z. Zeng, L. Feifeng, and M. Cherniakov, Experimental demonstration of passive BSAR imaging using navigation satellites and a fixed receiver, IEEE Geoscience and Remote Sensing Letters **9** (2012), pp. 477-481.

[2] J. L. Auterman, Phase stability requirements for bistatic SAR, in Proc. IEEE Nat. Radar Conf., Atlanta, GA, 1984, pp. 48-52.

[3] L. Borcea, T. Callaghan, and G. Papanicolaou, Synthetic aperture radar imaging with motion estimation and autofocus, in Inverse Problems 28.4 (2012): 045006.

[4] C. H. Casteel, Jr., L. R. A. Gorham, M. J. Minardi, S. M. Scarborough, K. D. Naidu, and U. K. Majumder, A challenge problem for 2D/3D imaging of targets from a volumetric data set in an urban environment, in Proceedings of SPIE, Vol. 6568, 2007, 65680D.

[5] M. Cheney, A mathematical tutorial on synthetic aperture radar, SIAM Review **43** (2001), pp. 301-312.

[6] M. Cheney and B. Borden, *Fundamentals of radar imaging*, SIAM, Philadelphia, 2009.

[7] J. C. Curlander and R. N. McDonough, *Synthetic aperture radar*, Wiley, New York, 1991.

[8] J. R. G. del Arroyo and J. A. Jackson, SAR Imaging Using WiMAX OFDM PHY, Proc. IEEE Radar Conf. (RADAR), 2011, pp. 129-134.

[9] D. Mehrholz, L. Leushacke, W. Flury, R. Jehn, H. Klinkrad, and M. Landgraf, Detecting, tracking and imaging space debris, ESA Bulletin **109** (2002), pp. 128-134.

[10] J. Garnier, Passive synthetic aperture imaging with limited noise sources, Inverse Problems **32** (2016), 095008.

[11] J. Garnier and G. Papanicolaou, Correlation based virtual source imaging in strongly scattering media, Inverse Problems **28** (2012), 075002.

[12] J. Garnier and G. Papanicolaou, Passive synthetic aperture imaging, SIAM J. Imaging Sciences **8** (2015), pp. 2683-2705.

[13] J. Garnier and G. Papanicolaou, *Passive imaging with ambient noise*, Cambridge University Press, Cambridge, 2016.

[14] J. Garnier, G. Papanicolaou, A. Semin, and C. Tsogka, Signal-to-noise ratio analysis in virtual source array imaging, SIAM J. Imaging Sciences **8** (2015), pp. 248-279.

[15] J. A. Haimerl and G. P. Fonder, *Space Fence system overview*, in Proceedings of the Advanced Maui Optical and Space Surveillance Technology Conference, September 2015.

[16] C. Ho and A. Wheelon, Amplitude scintillation due to atmospheric turbulence for the deep space network Ka-band downlink, Interplanetary Network Progress Report, Volume 42-158 (2004), pp. 1-21.

[17] E. J. Holder, J. C. Kerce, R. A. Smith, M. Shipman, R. W. McMillan, and J. K. Williams, Measurements of atmospheric turbulence with an x-band radar: correlation with angle-of-arrival results, in Proc. SPIE 4744, Radar Sensor Technology and Data Visualization, Volume 30 (2002).

[18] IEEE Aerospace and Electronic Systems Magazine, Volume 27, Issues 10-11, 2012.

[19] S. Knospe and S. Jonsson, Covariance estimation for dInSAR surface-deformation measurements in presence of anisotropic atmospheric noise, IEEE Trans. Geosci. Remote Sens. **48** (2009), pp. 2057-2065.

[20] M. E. Lawrence, C. T. Hansen, S. P. Deshmukh, B. C. Flickinger, Characterization of the effects of atmospheric lensing in SAR images, in SPIE Proceedings, Vol. 7308, 2009, 73080C.

[21] K. Mehta, A. Bakulin, J. Sheiman, R. Calvert, and R. Snieder, Improving the virtual source method by wavefield separation, Geophysics **72** (2007), pp. V79-V86.

[22] R. W. McMillan, Atmospheric turbulence effects on radar systems, Proceedings of the IEEE 2010 National Aerospace & Electronics Conference, 2010, pp. 181-196.

[23] A. Miranda and M. Cheney, Imaging moving objects from multiply scattered waves and multiple sensors, Inverse Problems **29** (2013) 054012.

[24] S. Quegan and J. Lamont, Ionospheric and tropospheric effects on synthetic aperture radar performance, International Journal of Remote Sensing **7** (1986), pp. 525-539.
[25] M. Rodriguez-Cassola, S. V. Baumgartner, G. Krieger, and A. Moreira, Bistatic TerraSAR-X/F-SAR Spaceborne-Airborne SAR experiment: Description, data processing, and results, IEEE Transactions on Geoscience and Remote Sensing **48** (2010), pp. 781-794.
[26] M. Siderius, C. H. Harrison, and M. B. Porter, A passive fathometer technique for imaging seabed layering using ambient noise, J. Acoust. Soc. Am. **120** (2006), pp. 1315-1323.
[27] S. V. Tsynkov, On the use of Start-Stop approximation for spaceborne SAR imaging, SIAM J. Imaging Sciences **2** (2009), pp. 646-669.
[28] M. T. Valley, S. P. Kearney, and M. Ackermann, Small Space Object Imaging: LDRD Final Report, Sandia National Laboratories, 2009.
[29] S. Wacks and B. Yazici, Passive Synthetic Aperture Hitchhiker Imaging of Ground Moving Targets – Part 1: image formation and velocity estimation, IEEE Transactions on Image Processing **23**(6) (2014), pp. 2487–2500.
[30] S. Wacks and B. Yazici, Passive Synthetic Aperture Hitchhiker Imaging of Ground Moving Targets – Part 2: Performance Analysis, IEEE Transactions on Image Processing **23**(9) (2014), pp. 4126–4138.
[31] L. Wang, C. E. Yarman, and B. Yazici, Doppler-Hitchhiker: A novel passive synthetic aperture radar using ultranarrowband sources of opportunity, IEEE Transactions on Geoscience and Remote Sensing **49** (2011), pp. 3521-3537.
[32] L. Wang, C. E. Yarman, and B. Yazici, Theory of passive synthetic aperture imaging, in Excursions in Harmonic Analysis, Volume 1, Applied and Numerical Harmonic Analysis, 2013, pp. 211-236.
[33] K. Wapenaar, E. Slob, R. Snieder, and A. Curtis, Tutorial on seismic interferometry: Part 2 - Underlying theory and new advances, Geophysics **75** (2010), pp. A211-A227.
[34] C. Yarman, L. Wang, and B. Yazici, Doppler synthetic aperture hitchhiker imaging, Inverse Problems **26** (2010), 065006.
[35] C. Yarman and B. Yazici, Synthetic aperture hitchhiker imaging, IEEE Trans. Image Process. **17** (2008), pp. 2156-2173.